INHIBITORY DYNAMICS IN THE SUPERFICIAL MEDIAL ENTORHINAL CORTEX

by

Joan José Martínez Castillo

A dissertation submitted to the faculty of
The University of Utah
in partial fulfillment of the requirements for the degree of

Doctor of Philosophy

Department of Bioengineering

The University of Utah

May 2016

The University of Utah Graduate School

STATEMENT OF DISSERTATION APPROVAL

The dissertation of **Joan José Martínez Castillo**

has been approved by the following supervisory committee members:

John A. White , Chair **8/25/15**
Date Approved

Alan Dale Dorval II , Member **8/25/15**
Date Approved

Richard D. Rabitt , Member **8/25/15**
Date Approved

Dale Matthew Wachowiak , Member **8/25/15**
Date Approved

Karen S. Wilcox , Member **8/25/15**
Date Approved

and by **Patrick A. Tresco** , Chair/Dean of

the Department of **Bioengineering**

and by David B. Kieda, Dean of The Graduate School.

ABSTRACT

The brain’s medial entorhinal cortex (MEC) plays a key role in spatial navigation, serving as the node between the hippocampus and the rest of the mammalian cortex. In the last 10 years, spatially-modulated “grid” cells in the superficial MEC have been shown to preferentially fire as the animal moves into the apices of a hexagonal grid. Our incomplete understanding of the inhibitory dynamics within the MEC, however, limits our knowledge of how this brain structure executes such spatial navigation functions. Here, we explore various roles that inhibition plays in the superficial MEC and characterize the neuronal population that elicits this inhibition. We find that excitatory stellate cells in the layer 2 MEC exhibit membrane-dependent, nonlinear synaptic integration of inhibitory inputs, amplifying inputs that arrive near their firing threshold and dampening those that arrive closer to rest. Our next study is the first systematic anatomical/electrophysiological characterization of the superficial MEC’s inhibitory interneuron population. We find that they are best classified into four clusters with distinct anatomical/electrophysiological profiles. In our last study, we investigated the viability of a novel, inhibition-mediated gamma rhythm model, finding that superficial MEC interneurons can exhibit resonant behaviors that could be key to generating neuronal network oscillations. The work presented here provides valuable groundwork for understanding MEC cortical computation.

A mi familia, que han hecho posible esta tesis que jamás leerán

TABLE OF CONTENTS

Chapters

LIST OF FIGURES

Figure Page

ACKNOWLEDGEMENTS

None of the text or figures in this work can properly convey the contribution others have made to this dissertation. Their support came not only in the teaching of techniques or discussion of the literature, but also in my development as a scientist and as a human being. The last six years were a success because of those around me. My accomplishments are their accomplishments.

First and foremost, I thank my advisor John White. Our hour-long talks are among the highlights of my PhD. You helped me navigate the studies contained in this dissertation, yes, but also you taught me how science was conducted, the customs and practices that surround the collection and analysis of data. And of course, I learned a lot more about politics, baseball, and leadership than I ever thought I would. As an undergraduate, one of my professors praised your character and your kindness and encouraged me to join your lab. I consider myself very lucky to have chosen a PI who is as kind, patient, and insightful as you are.

I thank Fernando Fernandez, the senior postdoc who was as close to a second PI as I could have hoped for. Your guidance in all things electrophysiology were the foundation in the experiments detailed here. Every figure carries your influence. I thank you for being my advisor and friend.

I am grateful to my committee: Chuck Dorval, Rick Rabitt, Karen Wilcox,

and Matt Wachowiak. You have helped focus my efforts and tested my abilities as a scientist. I also thank my collaborators: former labmate Mike Economo, Carmen Canavier, and Ruben Tikidzhi-Khamburyan. Our discussions were an integral part of my education, and I am grateful to have had the chance to work with you.

I want to thank Tilman Broicher and Nathan Smith in particular for teaching me new techniques and for having the patience it no doubt must have required on your part. You were both exemplary mentors, and I am proud to call you friends. I would like to thank as well all the White lab members whom I worked with and without whom these last few years would have no doubt been duller: Tilman K., Eric, Mike, Paola, Tristan, Katherine, Marsa, and Feliks. I thank the over two hundred rodents that helped provide the data contained here.

While my time in Utah was certainly dominated by my time in lab, I will cherish the time I spent with friends outside of lab. Jayme, Christian, and Sylvana, as well as all my friends in Utah BioE, helped make the last few years as wonderful as they have been. And though we have spent the last few years so far apart, I thank my friends Osama, Mohammed, Liz and Bobby, who left us too soon, for being a constant source of motivation. You are my role models.

Finally, I thank my parents, Américo and Rosanna, and my brother Antonio. They most of all have made me the person I am today. My parents, like their parents, emphasized hard work and learning as ways to better ourselves. This dissertation is in no small way a result of our family’s values and I dedicate it to you.

CHAPTER 1

INTRODUCTION

Medial entorhinal cortex

The medial entorhinal cortex (MEC) is the main cortical interface of the hippocampal formation (Burwell, 2006; Squire et al., 2004) and plays an important role in spatial navigation (Moser et al., 2008). Recently, *in vivo* extracellular single unit recordings have identified multiple functional cell types linked to spatial navigation in the MEC. Among these are grid cells, which fire preferentially when the animal is on the apices of a hexagonal lattice (Hafting et al., 2005); boundary cells that fire preferentially along the borders of an environment (Solstad et al., 2008); head direction cells that fire preferentially according to the orientation of the animal's head (Sargolini, 2006); and conjunctive cells which show some combination of the previous behavioral correlates (Sargolini, 2006). The presence of these behaviorally-linked cell types has made the MEC cortical circuitry an attractive target for anatomical and physiological study.

Like any cortical structure, the MEC is composed of two basic neuronal populations: a relatively homogeneous excitatory, glutamatergic principal cell population that projects to other brain regions; and a heterogeneous inhibitory, GABAergic interneuron population that modulates local activity (McBain and

Fisahn, 2001). The two main types of principal cells are star-shaped stellate cells predominant in the superficial layers and conically-shaped pyramidal cells present throughout the MEC (Canto and Witter, 2012). GABAergic interneurons, in turn, are an anatomically and physiologically diverse population that represent a minority (<20%) of the neurons in the MEC (Canto et al., 2008; Gatome et al., 2010).

MEC connectivity varies by layer. Principal neurons in the superficial layers of the MEC project to the dentate gyrus via the perforant path, providing the main excitatory cortical input to the hippocampal formation; neurons in the deeper layers receive direct input from hippocampus and serve as one of the hippocampus major outputs (Canto et al., 2008). As with its connective differences, the MEC has functional differentiation between the cell layers. Grid cells are primarily located in layer 2 of the MEC (Hafting et al., 2005), where stellate cells are the major principal cells, whereas the other functional cell types are present either throughout the entire MEC (boundary cells) or particularly located in layers 3 and 5 (head direction and conjunctive cells) (Sargolini, 2006; Solstad et al., 2008; Taube and Muller, 1998), where the majority of principal cells are the more ubiquitous pyramidal cells.

Neural oscillations in the medial entorhinal cortex: theta and gamma

Local field potential recordings have long revealed the presence of narrow-band, behavior-dependent oscillations in the mammalian cortex (Buzsáki, 2006). The exact mechanism of generation and the physiological function of these oscillations remains an area of active research. The oscillations are known to represent periodic activity in neurons close to the recording site, and have generally been classified into distinct frequency bands (Buzsáki, 2006). The work in this dissertation encompasses work on two such bands: the slow theta (4-12 Hz) oscillation and fast gamma (30-100 Hz) oscillation.

Like much of the hippocampal formation, the MEC exhibits a prominent extracellular electrical signal in the 4-12 Hz theta band (McNaughton et al., 2006; Witter and Moser, 2006). Brain functions such as memory formation, synaptic plasticity, and spatial navigation have been posited to be dependent on the theta oscillation for temporal coordination (Bland and Bland, 1986; Buzsáki, 2002; Huerta and Lisman, 1995). In the superficial MEC, the theta rhythm has been posited to play a role in grid cell firing (Brandon et al., 2011; Giocomo et al., 2007; Hafting et al., 2005; Koenig et al., 2011), although there is evidence that questions the importance of the theta rhythm to grid field generation (Couey et al., 2013; Domnisoru et al., 2013; Pastoll et al., 2013; Schmidt-Hieber and Häusser, 2013; Stensola et al., 2012; Yartsev and Ulanovsky, 2013). Intracellularly, stellate cells exhibit synaptically-driven membrane potential theta oscillations *in vivo* near threshold, and show pronounced ramp depolarizations when in their respective grid fields (Domnisoru et al., 2013; Schmidt-Hieber and Häusser, 2013). These phenomena suggest the functional relevance of stellate cell membrane potential fluctuations.

Another prominent cortical rhythm is the faster 30-100 Hz gamma band oscillation observed in the MEC (Chrobak and Buzsáki, 1998). Gamma oscillations have been often posited to play a crucial role in multisensory integration, wherein different sensory inputs are “bound” together to form a unified percept (Singer, 2006). More generally, they are believed to help mediate communication between separate cortical regions: gamma-entrained neuronal ensembles in one cortical region may preferentially communicate with phase-specific gamma-entrained neural ensembles in another cortical region (Wang, 2010). Cortical gamma rhythms may also play a crucial role in memory formation and attention (Jensen and Colgin, 2007). In the MEC, gamma has been theorized to both coordinate activity with the hippocampus in a task-specific manner via its reciprocal input/output connections and combine the inputs it receives from various cortical areas (Chrobak and Buzsáki, 1998; Quilichini et al., 2010; Schomburg et al., 2014). The mechanism by which these gamma oscillations are generated in the MEC are not well understood, and the physiological validation of a proposed gamma rhythmogenesis model is the focus of Chapter 4 of this dissertation.

Membrane dynamics and synaptic integration in stellate cells

In vitro intracellular experiments in stellate have described a prominent (approximately 5 mV peak-to-peak) intrinsic membrane potential oscillation (MPO) as cell is depolarized toward threshold (Alonso and Llinás, 1989; Burton et al., 2008; Dickson et al., 1997; Dorval, 2005; White et al., 1998). This MPO is due to the interplay between the persistent sodium current, I_{NaP}, and the hyperpolarization-activated cation current, I_h (Alonso and García-Austt, 1987; Alonso and Klink, 1993; Dickson et al., 2000; White et al., 1998). Basically, as the membrane potential is depolarized, the inward current I_h is slowly deactivated and the membrane potential is hyperpolarized. As the deactivation of I_h is slow (on the order of 200-300 ms near threshold), it creates a delayed feedback mechanism that enables sustained oscillations (Dickson et al., 2000). Although I_h alone can produce oscillatory behavior, the effect is amplified by the depolarization-activated opening of persistent sodium channels.

Along with producing subthreshold MPOs, I_{NaP} and I_h have a nonlinear effect on the impedance spectra of stellate cells. This can affect how these cells integrate inhibitory and excitatory synaptic inputs, a phenomenon which is investigated in the second chapter of this dissertation. First, the combination of these currents produces a resonant peak in the impedance spectrum of stellate cells at near-threshold potentials (Burton et al., 2008; Erchova et al., 2004; Fernandez and White, 2008; Garden et al., 2008; Haas and White, 2002; Nolan et al., 2007). Second, I_{NaP} endows stellate cells with a depolarization-induced increase in membrane impedance, an effect referred to as a negative slope conductance (Stafstrom et al., 1982). Blocking I_{NaP} with TTX eliminates this effect. Given the behavioral context of the large (>10 mV) membrane potential fluctuations stellate cells undergo *in vivo*, any significant change in synaptic integration due to this impedance increase could have functional consequences in physiological stellate cell dynamics. Furthermore, since interneurons specifically make up a large number of the synaptic inputs onto hippocampal neuronal somata (Freund and Buzsáki, 1996) and are known to fire synchronously (Quilichini et al., 2010) in the MEC, it is likely that effects on synaptic integration of inhibitory inputs in stellate cells is particularly relevant to *in* *vivo* dynamics.

Interneuron form and function in the superficial MEC

Although much effort has been focused on understanding the properties of the MEC's principal cells, there remains a paucity of electrophysiological data on the GABAergic interneurons that modulate principal cell activity in the superficial MEC. Recent evidence, however, suggests that GABAergic interneurons play an important role in the spatial navigation functions of the MEC (Couey et al., 2013; Domnisoru et al., 2013; Garden et al., 2008; Pastoll et al., 2013; Varga et al., 2010). Layer 2 stellate cells, which along with superficial layer pyramidal cells are the putative grid cells measured *in vivo*, show very sparse to no interconnectivity; instead stellate-to-stellate is mediated via inhibitory interneurons in the superficial MEC (Couey et al., 2013). Inhibitory synaptic activity onto principal cells is also known to be much higher in superficial layers of the MEC than in the deeper layers: Woodhall et al. (2005) found that spontaneous inhibitory postsynaptic currents were approximately four times higher in frequency in layers 2 and 3 compared to layers 5 and 6. Computational modeling of grid field formation in the MEC has recently transitioned toward more inhibition-dominated network models to accommodate these findings (Burak and Fiete, 2009; Thurley et al., 2013). Finally, (Pastoll et al., 2013) showed that feedback inhibition without recurrent excitation was sufficient to produce theta-nested gamma (30-100 Hz) oscillations in stellate cells within optically stimulated MEC acute brain slices. These theta-nested gamma oscillations are believed to be important in coordinating interactions between MEC and hippocampus.

Despite the important role that interneurons play in the superficial MEC, studying this neuronal cell population remains difficult for two reasons. First, interneurons amount to less than 10% of neuronal cell bodies in the superficial MEC (Gatome et al., 2010), making targeted studies difficult. Second, as in other cortical regions, the population of interneurons in the superficial MEC interneuron population is quite diverse (Ascoli et al., 2008; Buzsáki et al., 2004; Maccaferri and Lacaille, 2003; McBain and Fisahn, 2001; Whittington and Traub, 2003). Whereas MEC principal cells are usually categorized as either stellate or pyramidal (with some efforts to further subdivide pyramidal cells), cortical interneurons can be subdivided into as little as 3 types to as many as 100 (DeFelipe et al., 2013). This “interneuron diversity problem” is compounded as interneurons can be categorized by their anatomical, molecular or physiological characteristics. Using only a single categorization scheme fails to completely capture the functional diversity of interneurons, so two or three categories must be examined concurrently to adequately characterize interneurons. Although there has not been a systematic study of the electrophysiological properties of superficial MEC interneurons (nor one linking these properties to anatomical classifications), there have been anatomical studies describing some basic morphologies for superficial MEC interneurons (Canto et al., 2008). These studies have classified interneurons into layer 1 horizontal neurons, layer 1/2/3 multipolar neurons, layer 2 horizontal bipolar cells, layer 2 fan cells, layer 2 basket cells (forming an axonal “basket” at targeted somas), layer 2 chandelier cells (forming candle-shaped axonal projections onto principal axons), layer 3 pyramidal-like interneurons, and layer 3 bipolar cells. It is likely that these different anatomical types have different functions within the cortical circuit (Kepecs and Fishell, 2014).

Despite the anatomical categorization of MEC interneurons, the combination of low cell counts and functional diversity has made systematic electrophysiological studies difficult. Limited data are available on the firing pattern of basket cells and chandelier cells, both of which have been generally lumped together using their common molecular identifier parvalbumin (Wouterlood et al., 1995), but these data do not include passive membrane features, basic input/output measures or action potential characterization. Furthermore, the electrophysiological properties of remaining cell types in the superficial MEC are largely unknown (Gloveli et al., 1997; Wolansky et al., 2007). Finally, what limited data are available does not take into account the localization of these neurons within the MEC dorsoventral axis, which as previously described has been shown to exhibit a gradient in inhibitory activity as well as principal cell physiology and grid field spacing.

Inhibition-mediated gamma oscillations in the MEC

Like other cortical regions, the medial entorhinal cortex exhibits robust rhythmic activity in the 30-100 Hz gamma band (Chrobak and Buzsáki, 1998). Cortical oscillations are believed to coordinate spike timing of different neuronal populations and may synchronize activity across different brain regions (Wang, 2010). In the cortex, gamma rhythms have been implicated in memory formation, attention (Jensen and Colgin, 2007), and, most commonly, sensory binding (Singer, 2006); in the MEC in particular, gamma is theorized to coordinate activity with the hippocampus in a task-specific manner and associate inputs from various cortical areas (Chrobak and Buzsáki, 1998; Quilichini et al., 2010; Schomburg et al., 2014).

Multiple mechanisms for gamma rhythmogenesis have been described, invariably relying on fast GABA-mediated inhibition to pace synchrony (Buzsáki and Wang, 2012). Two basic connectivity models have been proposed: the first describes a minimal, mutually inhibitory network (comprised of interneurons) that is sufficient to produce gamma synchronization (I-I models), while the second describes an excitatory-inhibitory feedback loop that requires both excitatory principal cells and interneurons to create gamma synchrony (E-I models). Experimental evidence has been presented for both I-I models and E-I models (Csicsvari et al., 2003; Whittington et al., 1995), and it is likely that several gamma generation mechanisms operate in the MEC *in vivo* (Cunningham, 2004, 2006; Cunningham et al., 2003; Middleton et al., 2008).

Work specific to the MEC has shown that MEC gamma oscillations arise independently in layers 2, 3, and 5, with the strongest gamma rhythm being present in layer 2 (Quilichini et al., 2010). Superficial MEC low-mid gamma oscillations in particular are thought to coordinate activity between the MEC and hippocampus (Schomburg et al., 2014), possibly allowing MEC input to preferentially arrive during the most excitable phases of the hippocampal gamma cycle. These mechanisms, however, require operational uniformity in gamma frequencies within each region, a feature that has been difficult to achieve in models with heterogeneous input.

Recent gamma rhythmogenesis models have attempted to address this issue by constructing stochastic synchrony models wherein neurons are in a fluctuation-driven regime and firing probability is dictated by delayed feedback (Brunel, 2003). These models are more amenable to heterogeneous inputs and more closely replicate the physiological sparseness of firing in individual neurons. Although these models have generally treated interneurons as simple integrators, recent studies have shown that modeling interneurons as resonators can further facilitate frequency uniformity in brain regions in these network types (Baroni et al., 2014; Moca et al., 2014).

Along this paradigm, a sparsely connected I-I model of gamma rhythmogenesis has been proposed (Tikidji-Hamburyan and Canavier, unpublished results) that relies on postinhibitory rebound (PIR) spiking to elicit gamma oscillations in the network. This model constructs a sparsely connected network comprised of type 2 spiking resonator model neurons (Izhikevich, 2003). The bias current depolarizes interneurons toward threshold to reach a resonant firing regime, where they fire intermittently. Once a neuron fires, it inhibits other neurons that are similarly in the resonant firing regime. These inputs could then elicit a postinhibitory rebound spike in the target cell. As interneurons cause other interneurons to fire, the network becomes synchronized to a network period approximately equal to the input-to-spike delay. The model is robust to noise, being able to maintain a stable network frequency despite the interneurons receiving noisy inputs from both outside sources and other interneurons.

In this regime, the frequency of the network oscillation is directly linked to the postsynaptic potential-to-spike latency in inhibitory neurons; as such a delay of 10-33 ms would be necessary to account for a 30-100 Hz gamma oscillation in the network. Although there is some limited evidence showing that interneuronal PIR spiking may occur *in vivo* in the MEC (Kumar and Buckmaster, 2006), there are no data on intrinsic properties of MEC interneurons whereby they exhibit PIR spiking in response to synaptic inputs. Also, although there is significant evidence supporting the role of fast-spiking basket cells in gamma rhythmogenesis (Cardin et al., 2009), our understanding of the role other interneuron populations may play in gamma is limited (Buzsáki and Wang, 2012).

Inhibitory dynamics in the medial entorhinal cortex

The common focus of the work presented in this dissertation is to better understand various aspects of the inhibitory dynamics in the superficial medial entorhinal cortex. In Chapter 2, we describe a synaptic integration effect in the superficial MEC's stellate cells, whereby membrane potential is observed to amplify/attenuate the amplitude of synaptic inputs. The findings in this chapter describe an integrative phenomenon that preferentially affects the integration of inhibitory synaptic inputs, which synapse directly onto the stellate cell somas (Freund and Buzsáki, 1996; Hu et al., 2010; Jarsky et al., 2005). Chapter 3 covers the electrophysiological/anatomical characterization and clustering of interneuronal populations in the superficial MEC, the first systematic study on the inhibitory components of this cortical circuit. Chapter 4 covers the physiological validation of an inhibition-mediated gamma rhythmogenesis model, an important role of inhibitory neurons in the superficial MEC. In the final chapter, the findings of this dissertation are summarized and future directions that arise from the work presented here are explored.

CHAPTER 2

MEMBRANE POTENTIAL-DEPENDENT INTEGRATION OF SYNAPTIC INPUTS IN ENTORHINAL STELLATE NEURONS

Introduction

The 4-12 Hz theta rhythm is the dominant electrical signal recorded extracellularly in the rodent hippocampal formation during a variety of behavioral states (Buzsáki, 2002; Kramis et al., 1975; Mitchell and Ranck, 1980; Vanderwolf, 1969) and has been observed concurrently in the medial septum, nucleus accumbens, amygdala, prefrontal cortex, and many parts of the olfactory system (Bland and Oddie, 2001; Seidenbecher et al., 2003; Siapas et al., 2005). Brain functions as diverse as memory formation, synaptic plasticity, spatial navigation, and sensorimotor integration have been suggested to be reliant upon the theta rhythm for temporal coordination (Bland and Oddie, 2001; Buzsáki, 2002; Huerta and Lisman, 1993; Lisman, 2010). Additionally, the theta rhythm has been hypothesized to play a critical role in the formation of the grid-like spatial firing patterns of neurons in the superficial entorhinal cortex (Brandon et al., 2011; Giocomo et al., 2007; Hafting et al., 2005; Koenig et al., 2011),

Adapted from Economo, M. N.*, Martínez, J. J.* and White, J. A. (2014), Membrane potential-dependent integration of synaptic inputs in entorhinal stellate neurons. Hippocampus, 24: 1493–1505. doi: 10.1002/hipo.22329. Reprinted with permission from John Wiley and Sons, Inc.

although recent evidence points to other models (Couey et al., 2013; Domnisoru et al., 2013; Harvey et al., 2009; Pastoll et al., 2013; Remme et al., 2010; Schmidt-Hieber and Häusser, 2013; Stensola et al., 2012; Yartsev et al., 2011). Several factors have been suggested to contribute to the hippocampal theta rhythm, including cellular and synaptic properties within the hippocampus and medial entorhinal cortex (Alonso and Llinás, 1989; Gillies et al., 2002; Gloveli et al., 2005a, 2005b; Goldin et al., 2007; Goutagny et al., 2008; Haas et al., 2007; Heys et al., 2013; Pastoll et al., 2012; Tort et al., 2007; White et al., 2000) and unidirectional or bidirectional interactions of these structures with the medial septum (Bland and Bland, 1986; Freund and Antal, 1988; Hangya et al., 2009; Manseau et al., 2008; Stewart and Fox, 1990; Wang, 2002).

Stellate neurons of the medial entorhinal cortex (MEC) layer II exhibit pronounced narrow-band, though non-periodic, membrane potential oscillations (MPOs) in the theta band. *In vitro*, MPOs occur spontaneously through an interplay of intrinsic ionic currents near spike threshold (Alonso and Llinás, 1989; Burton et al., 2008; Dickson et al., 2000; Dorval and White, 2005; Pastoll et al., 2012; White et al., 1998) and typically have a peak-to-peak amplitude of 1-5 mV. Furthermore, stellate neurons exhibit a resonant peak in the subthreshold membrane impedance spectrum at theta frequencies (Burton et al., 2008; Erchova et al., 2004; Fernandez and White, 2008; Garden et al., 2008; Haas and White, 2002; Nolan et al., 2007), indicating that synaptic inputs modulated at theta frequencies may be preferentially amplified. While this effect is present in stellate cells *in vitro*, these intrinsic MPOs are not observed *in vivo* either at rest, where synaptic input may be dampening such oscillations, or during movement, where theta oscillations are synaptically driven (Schmidt-Hieber and Häusser, 2013). During movement *in vivo*, ~10 mV MPOs have been observed concomitantly with population-level local field potential oscillations at theta frequencies (Domnisoru et al., 2013; Harvey et al., 2009; Quilichini et al., 2010; Schmidt-Hieber and Häusser, 2013), presumably reflecting resonant responses to coherent synaptic input. It is currently unknown if and how the intrinsic rhythmicity of stellate neurons contributes to population-level oscillations. However, the ability of these cells to spontaneously produce theta-frequency MPOs and the observation of a theta generator in the superficial MEC (Alonso and García-Austt, 1987; Kocsis et al., 1999; Mitchell and Ranck, 1980) have prompted the suggestion that the intrinsic electrophysiological rhythmicity of stellate cells could be responsible for the production or strengthening of this rhythm (Hasselmo et al., 2000).

Here, we demonstrate that a slowly inactivating, TTX-sensitive conductance, primarily represented by the persistent sodium conductance (G_{NaP}) (Magistretti and Alonso, 1999), is responsible for a highly nonlinear subthreshold membrane mechanism. Our results are consistent with those from other brain areas (Stuart and Sakmann, 1994). The inward current generated by G_{NaP} gives rise to an apparent depolarization-induced increase in input resistance, an effect known in the literature as negative slope conductance (Stafstrom et al., 1982). Using the dynamic clamp technique, we show that a noninactivating, TTX-sensitive conductance leads to highly nonlinear, membrane potential- and phase-dependent integration of synaptic inputs in the membrane potential range of ongoing oscillations—both intrinsic and synaptically-driven—near spike threshold. This nonlinearity has a profound impact on the integrative properties of stellate cells and may contribute to the selective amplification of synaptic input arriving coherently as a result of population-level, input-driven theta oscillations *in vivo*.

Materials and methods

Electrophysiology

All experiments were conducted as approved by the University of Utah Institutional Animal Care and Use Committee. Measurements from stellate cells of the medial entorhinal cortex were made from Long-Evans rats, 18-32 days old. These animals were anesthetized with isoflurane and decapitated. The brain was removed and chilled in ACSF (in mM, 125 NaCl, 2.5 KCl, 1.25 NaH_2PO_4, 10 $MgCl_2$, 25 $NaHCO_3$, 25 Glucose, 2 $CaCl_2$) and slices were cut in the horizontal plane using a vibrating microtome (Vibratome 1000+; Vibratome, St. Louis, MO) to 400 μm thickness. After letting slices recover for at least one hour in a holding chamber at room temperature, they were transferred to a heated (32-34°C) chamber (Warner Instruments), mounted on an upright microscope stage (AxioSkop FS2; Carl Zeiss, Thornwood, NY). Slices were perfused with heated ACSF and bubbled continuously with 95/5 percent O_2/CO_2. Neurons were visualized using infrared differential interference contrast video microscopy (CCD 100; Dage/MTI, Michigan City, IN). Whole-cell patch clamp recordings were obtained using patch pipettes (2-5 MΩ) fabricated from borosilicate glass (1.0

O.D. 0.5 I.D.; Sutter Instruments, Novato, CA) and filled with (in mM), 120 K-Gluconate, 5 $MgCl_2$, 0.2 EGTA, 10 HEPES, 20 KCl, 7 di(tris) phosphocreatine, 4 Na_2ATP, 0.3 Tris-GTP. Presented data were not corrected for the junction potential, presumed to be 10-12 mV. Entorhinal stellate cells were identified electrophysiologically by their prominent sag potentials following hyperpolarization and the presence of MPOs near threshold (Alonso and Klink, 1993). Stellate cells were anatomically identified by their location in layer II of the MEC, their large cell body and the absence of an apical dendrite. In a small number of experiments, the recording pipette contained 0.6% biocytin (Invitrogen, Carlsbad, CA) and recorded cells were processed for posthoc visualization using established techniques (Kispersky et al., 2012). This aided post-hoc anatomical identification of stellate and pyramidal cells. Control trials using tetrodotoxin (TTX) used ACSF that with 0.5 μM of TTX; those using ZD7288 used concentrations of 20 μM in ACSF. All reagents were obtained from Sigma-Aldrich (St. Louis, MO), unless otherwise noted.

Stimulation protocols

Stimuli for calculating subthreshold impedance were frozen noise current waveforms with white frequency spectra up to 250 Hz. Current waveforms were either 10 sec in duration and repeated 8 times, or 50 sec long and applied in a single trial. Trials in which action potentials were generated were omitted from further analysis.

In comparisons with pyramidal neurons and stellate neurons in TTX, artificial MPOs were elicited by injecting a small-amplitude current waveform constructed in the frequency domain. These stimuli had Gaussian power spectra with a standard deviation of 4 Hz, centered at 3.5 Hz, and truncated at 0Hz. The phases of individual frequency components were uniformly distributed between 0 and 2π. This stimulus was constructed in the frequency domain to resemble spontaneous MPOs and adjusted to generate 3-5 mV peak-to-peak fluctuations in the membrane potential of each neuron.

Synaptic conductances were simulated using dynamic clamp software (Bettencourt et al., 2008; www.rtxi.org; Dorval et al., 2001; Lin et al., 2010) on a Pentium 4 computer running Linux with a patched version of the real-time application interface (RTAI) kernel and equipped with an analog-to-digital converter card (National Instruments, Atlanta GA). Voltage was measured and a control signal applied using a MultiClamp 700B amplifier (Axon Instruments, Union City, CA).

Conductances were implemented according to $I_{syn}(t)=g_{max}\cdot s(t)(V-E_{syn})$, where g_{max} is maximal conductance, V is membrane voltage, E_{syn} is the reversal potential of the synapse (-75 mV for inhibitory, 0 mV for excitatory), and $s(t)$ is the difference of two exponentials with time constants of τ_{rise} = 1 ms and τ_{fall} = 3 ms. Artificial postsynaptic conductances (PSGs) were elicited as above using a modified homogeneous Poisson process at an average rate of 0.5 Hz with the additional constraint that events were separated by at least 500 ms. PSGs occurring within 250 ms of an action potential were disregarded during further analysis.

Data analysis

Data analyses were performed using custom scripts written in MATLAB (The Mathworks, Natick, MA). Impedance-frequency plots were calculated by dividing the amplitude of the Fourier transform of the membrane voltage by the transform of input current waveforms. Postsynaptic potential amplitudes were calculated as the difference between the maximum (minimum) voltage within 15 ms of stimulation in response to excitatory (inhibitory) inputs and the voltage immediately prior to stimulation. Given that the implemented synaptic inputs include a driving-force term, the amplitude of applied synaptic currents varied with membrane potential. To correct this driving force effect, in the analysis PSP amplitudes were divided by the integral of the input current (total electric charge) driving that PSP. In order to compare across trials, PSP amplitudes were also normalized by dividing PSP amplitudes by the mean PSP amplitude of that trial. PSP modulation values are thus presented as percent differences per mV of depolarizations, rather than mV (in amplitude) differences per mV of depolarization. When determining significant difference to zero, reported p values were calculated using a one-sample t-test. When comparing among groups, reported p values were calculated using a one-way ANOVA with a Tukey test for means when comparing groups assuming equal variance, except when otherwise noted. P values reported for correlation coefficients were calculated with the 'corrcoef' function in MATLAB and represent the probability that a correlation coefficient as large as or larger than the reported value would be obtained by chance.

To evaluate the effect of peak vs. trough and rising vs. falling phase on the amplitude of PSPs, traces were detrended using a 4^{th} order highpass Butterworth filter with a cutoff frequency of 1 Hz. Using this detrended trace, the PSPs within the band of 20% most depolarized potentials were labeled “peak phase” PSPs; the PSPs within the band of 20% most hyperpolarized potentials were labeled “trough phase” PSPs. The middle 40% membrane potential band was used to calculate the rising and falling phase PSPs. Within this band, PSPs that were preceded by 25 ms of an overall increase in membrane potential were labeled “rising phase” PSPs, whereas those preceded by 25 ms of an overall decrease in membrane potential were labeled “falling phase” PSPs. When comparing PSP amplitudes between a) peak and trough phase PSPs and b) rising and falling phase PSPs, the reported p values were calculated using a two sample paired t-test assuming equal variance.

Results

Voltage dependence of subthreshold impedance

Below spike threshold, stellate neurons of the medial entorhinal cortex (see Figure 2.1A) express substantial quantities of a noninactivating, “persistent” sodium conductance, G_{NaP} (Alonso and Klink, 1993; Burton et al., 2008; Magistretti and Alonso, 1999; White et al., 1998). Somewhat paradoxically, activation of G_{NaP} leads to an increase in the apparent input resistance of stellate neurons, as the slope of the current-voltage relationship of the channel is negative (Stafstrom et al., 1982). The presence of G_{NaP} necessarily contributes a nonlinearity to the subthreshold response properties of these neurons: membrane impedance is thus a function of membrane voltage, increasing as a

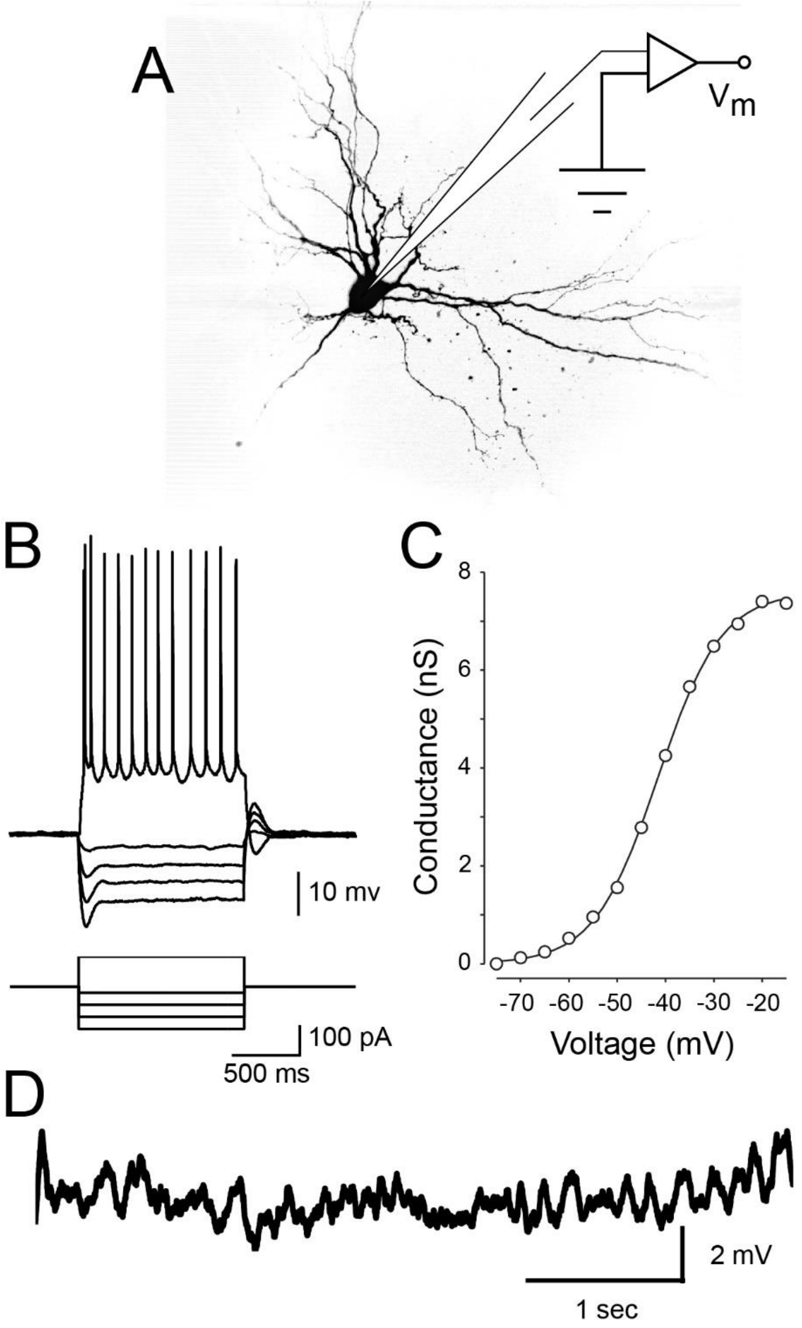

Figure 2.1 Stellate neuron morphology and electrophysiology
A Schematic of the recording setup and morphology of a representative stellate neuron. **B** Stellate neurons display a pronounced inward rectification (sag) in response to hyperpolarizing current steps. In response to a step of depolarizing current, stellate neurons respond with a short burst of action potentials followed by tonic spiking. **C** Average activation curve of persistent sodium conductance (G_{NaP}) across a population of stellate cells (modified from Burton et al., 2008). **D** Spontaneous subthreshold oscillations appear as the neuron is depolarized to just below spike threshold.

neuron is depolarized towards spike threshold. Here, our results are consistent with prior findings showing the characteristic membrane impedance spectrum of entorhinal stellate cells (Erchova et al., 2004; Nolan et al., 2007) and the role of TTX-sensitive currents in the impedance spectrum (Boehlen et al., 2013).

To quantify the voltage dependence of the subthreshold impedance in entorhinal stellate cells, we recorded from these cells in the current-clamp configuration (Figure 2.1). Stellate neurons were easily identifiable by established criteria (Alonso and Klink, 1993), including their location in superficial layer II of the medial entorhinal cortex, the presence of a prominent sag in response to hyperpolarizing current steps (Figure 2.1B), and the presence of spontaneous MPOs near spike threshold (Figure 2.1D). In a subset of experiments, the recording pipette contained 0.6% biocytin and stellate morphology was confirmed following post-hoc staining with a fluorescent molecule (Figure 2.1A).

In addition to displaying the characteristic resonance peak at theta frequencies resulting from the presence of the hyperpolarization-activated cation current, I_h, (Burton et al., 2008; Nolan et al., 2007), the membrane impedance of entorhinal stellate cells was found to be exquisitely sensitive to membrane potential (Figure 2.2A). Specifically, the impedance increased at all frequencies below the membrane's intrinsic cutoff frequency (~10 Hz) as the membrane potential was depolarized towards spike threshold (Figure 2.2A). We observed a particularly large increase at the resonant frequency, where the impedance reaches a maximum, although the Q-value (ratio of peak impedance to

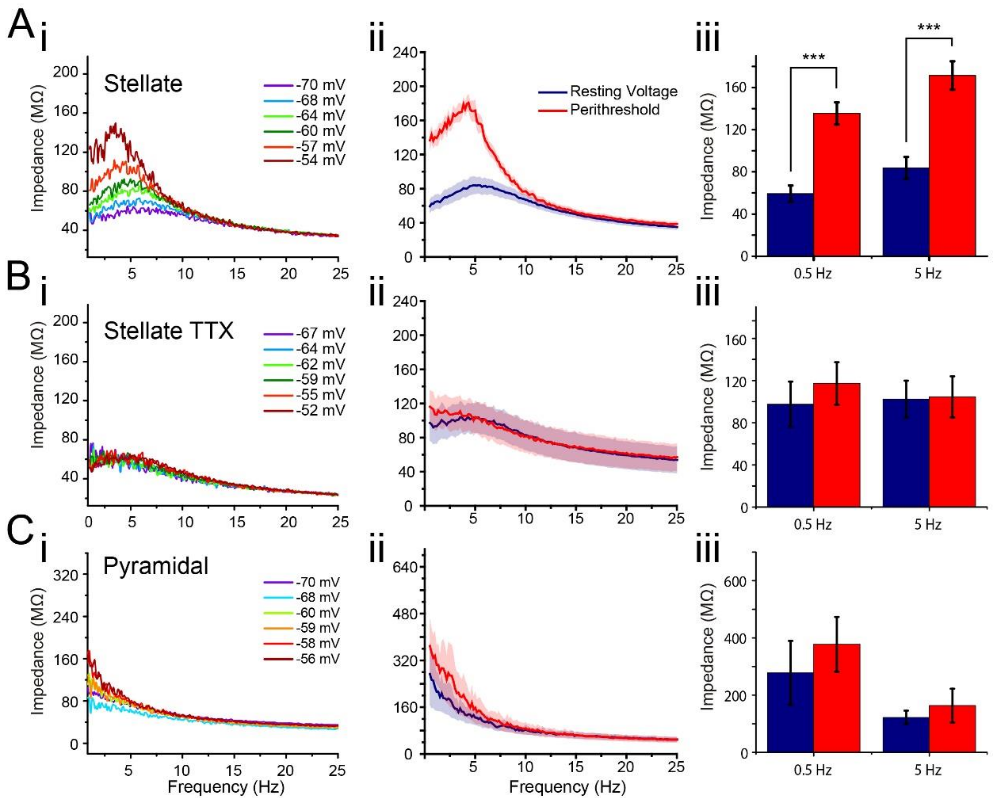

Figure 2.2 Membrane potential-dependent impedance spectra in MEC principal cells

Ai Membrane impedance as a function of frequency for a stellate cell at different mean voltages (as indicated). **ii,iii** Average impedance of stellate neurons (n=10) at their resting potentials and near threshold. **Bi** Impedance measurements in the same cell as in (Ai) in 0.5 µM tetrodotoxin (TTX). **ii,iii** Average impedance across all stellate neurons recorded in TTX (n=8) at resting and threshold potentials. **Ci** Impedance of a putative entorhinal layer II/III pyramidal neuron at a range of mean voltages. **ii,iii** Average impedance of putative pyramidal neurons (n = 5) at resting and threshold potentials. Impedance is sensitive to voltage in stellate neurons under control conditions (**A**) but not in TTX (**B**) or in nearby pyramidal neurons (**C**).

impedance at 0.1 Hz) was statistically unchanged (Figure 2.2Aiii; $Q_{rest} = 1.30 \pm 0.09$; $Q_{thresh} = 1.42 \pm 0.11$; $p = 0.45$). Additionally, the sensitivity of impedance to voltage became greater as threshold was approached. Across all stellate cells studied, the impedance at 5 Hz increased from 83.6 ± 10.5 MΩ at resting potential to 171.5 ± 13.4 MΩ near threshold ($p < 10^{-3}$). Similarly, at 0.5 Hz, impedance increased from 59.3 ± 7.7 MΩ at rest to 135.4 ± 10.5 MΩ near threshold ($p < 10^{-3}$; $n = 9$). For the preceding comparisons, the mean voltage in the resting condition was -68.0 mV ± 0.6 mV compared to -54.8 ± 1.1 near threshold, reflecting the presumed biologically relevant range of subthreshold voltages for these neurons. It is worth noting that slices were held at a temperature of 32-34°C, lower than the physiological 37°C, in order to preserve the health of the brain slices. At this lower temperature, the resonance frequency in hippocampal pyramidal cells has been shown to decrease from approximately 8 Hz to 4 Hz (Hu et al., 2002). As such, it is possible that using lower-than-physiological holding temperatures may have lowered the resonance frequency of the stellate cells in this study.

To confirm that the observed voltage dependency of impedance was indeed a product of persistent sodium channels, we repeated these measurements in the presence of 0.5 μM tetrodotoxin to block voltage-gated sodium channels (TTX; Figure 2.2B). In TTX, the voltage dependence of the membrane impedance was abolished and the impedance spectrum closely matched the spectrum measured at the resting membrane potential in control ACSF (Figure 2.2B; threshold impedance in TTX at 5 Hz: 104.6 ± 19.5 MΩ, hyperpolarized impedance in control: 102.4 ± 17.5 MΩ; p = 0.94; n = 9). Averaged data (Figure 2.2Bii) show a hint of resonance near resting potential, probably due to the effects of I_h. This effect is small, and thus hard to see in many individual examples (e.g., Figure 2.2Bi). The observation that impedance in TTX was similar to that measured at the resting potential of the cell in the control condition ($p = 0.36$) is consistent with the interpretation that voltage-sensitive input resistance is mediated by G_{NaP}, as the persistent sodium conductance is nearly completely deactivated at rest (Figure 2.1C). Furthermore, nearby pyramidal neurons did not display a voltage-dependent impedance profile (5 Hz: 122.2 ± 23.6 MΩ at rest vs. 163.6 ± 58.8 MΩ near threshold; $p = 0.54$; $n = 4$), which suggests that G_{NaP}-mediated increase in impedance near threshold in pyramidal cells is either small or non-existing. Although TTX also blocks the transient sodium current, I_{NaT}, responsible for the upstroke of the action potential, this channel population comprises only a small (approximately 10%) of the total sodium current at this membrane potential range (Magistretti and Alonso, 1999). Since G_{NaP} represents the overwhelming majority of the sodium current in this voltage range, G_{NaP} is used here to refer to the slowly inactivating, TTX-sensitive conductance responsible for this effect.

Membrane potential variations within the physiological range affect synaptic integration due to impedance changes

The observations of voltage-dependent membrane impedance and theta-rhythmic membrane potential oscillations led us to hypothesize that synaptic inputs might be integrated with variable efficacy within the range of membrane potentials where subthreshold oscillations occur. As shown in Figure 2.3, we

Figure 2.3 Effects of driving force and impedance on PSP amplitude
A Post-synaptic potentials (PSPs) induced via dynamic clamp in a stellate cell depolarized to the peri-threshold region. At this level of depolarization, membrane potential oscillations are pronounced. PSPs of amplitude 0.5-3 mV were induced randomly in time to quantify modulation of PSP amplitudes by fluctuations in membrane potential. **B** Single IPSP samples were measured from moment of initiation to their peak, as illustrated by the arrows. The IPSP occurring at the more depolarized membrane potential (peak phase of the oscillation) is greater in amplitude than the IPSP in the more hyperpolarized membrane potential (trough phase of the oscillation). **C** Examples of the relationship between PSP amplitude and membrane potential for excitatory (**i,ii**) and inhibitory (**iii, iv**) PSPs amplitudes excluding a driving force normalization (**i,iii**) and including the driving force normalization (**ii, iv**). As expected, excitatory PSPs are somewhat attenuated with depolarization by the decreasing driving force (compare **i** and **ii**), while inhibitory PSPs are further amplified by the increasing driving force (compare **iii** and **iv**). **D** Population averages (stellates near threshold, n = 29 in 24 cells for excitatory, n = 41 in 26 cells for inhibitory; stellates in TTX, n = 15 in 11 cells for excitatory, n = 15 in 10 cells for inhibitory) for the modulation of PSP amplitude by membrane potential for the four cases illustrated in A (solid bars) and when the same measurements were repeated in TTX (shaded bars). The modulation effect is maintained in both uncorrected and driving force normalized conditions.

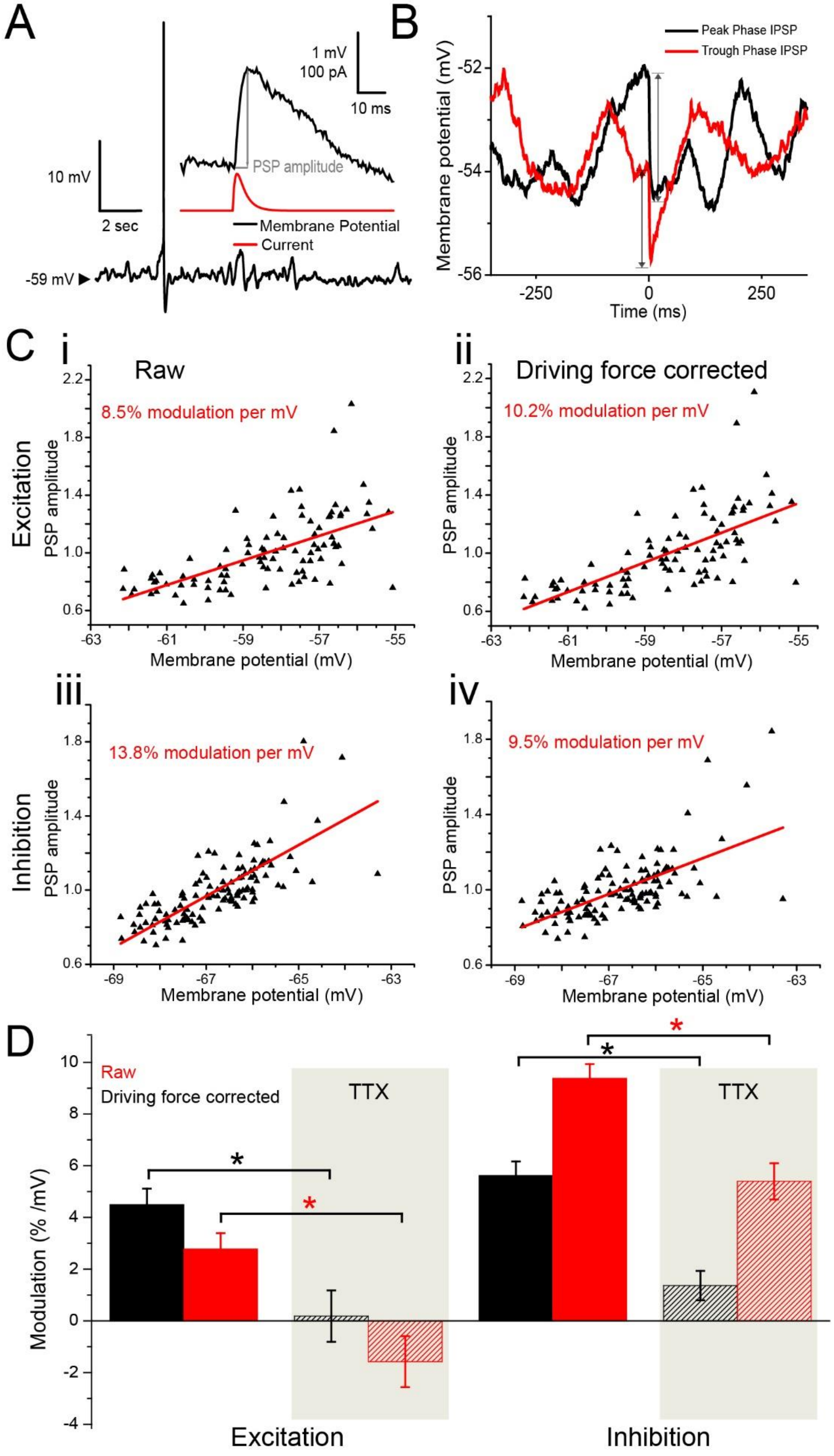
A
1 mV
100 pA
10 ms
10 mV
2 sec
PSP amplitude
Membrane Potential
Current
-59 mV
B
Peak Phase IPSP
Trough Phase IPSP
Membrane potential (mV)
-52
-54
-56
-250
0
250
Time (ms)
C
i
Raw
8.5% modulation per mV
ii
Driving force corrected
10.2% modulation per mV
Excitation
PSP amplitude
2.2
1.8
1.4
1.0
0.6
-63
-61
-59
-57
-55
Membrane potential (mV)
iii
13.8% modulation per mV
iv
9.5% modulation per mV
Inhibition
-69
-67
-65
-63
D
Raw
Driving force corrected
TTX
*
Modulation (% /mV)
10
8
6
4
2
0
-2
-4
Excitation
Inhibition

tested this hypothesis by current clamping cells and injecting a bias current to depolarize the membrane to perithreshold potentials, the membrane potential at which entorhinal stellate cell membrane potential oscillations were spontaneously and robustly generated, and applying artificial synaptic conductances via dynamic clamp (Figure 2.3A). Test artificial excitatory and inhibitory postsynaptic conductances (PSGs) with constant amplitude were applied randomly in time at low rates (see *Materials and Methods*). PSG amplitudes were set to elicit 0.5-3.0 mV voltage deflections (Figure 2.3B), which are small enough as to not alter either the steady state conductance of the cell or the amplitude/frequency of the theta-frequency subthreshold oscillations (as was done in Fernandez and White (2008) and Schmidt-Hieber and Häusser (2013)). Interestingly, even these small artificial PSPs appear to reset the phase of MPOs (Figure 2.3B).

The resulting relationship between postsynaptic potential (PSP) amplitude and the membrane potential at the time of PSG onset is illustrated for a single, representative stellate neuron in Figure 2.3C. Here, driving force corrected data are also shown along with raw, noncorrected data. Since the magnitude of postsynaptic current waveforms in the intact brain—introduced here via dynamic clamp—also depend on membrane potential, the synaptic driving force changes with changing membrane potential. For this reason, a simple calculation would predict that excitatory PSP amplitudes would decrease by approximately 2% per mV depolarization near threshold if the reversal potential of an 2-amino-3-(5-methyl-3-oxo-1,2- oxazol-4-yl)propanoic acid (AMPA) channel is taken to be 0 mV and the perithreshold region is assumed to be -55 to -50 mV. In contrast, inhibitory PSPs would be expected to increase in magnitude by 4-5% per mV depolarization for ionotropic γ–aminobutyric acid (GABA) synapses in the absence of any membrane nonlinearity if the reversal potential of these channels was taken to be -75 mV. When referring to driving force corrected data, PSP amplitudes have been divided by the integral of the input current (total electric charge) injected during that PSP.

In Figure 2.3C, both excitatory and inhibitory PSP representative samples are plotted versus membrane potential, in both non-corrected and driving force corrected form. The corresponding PSP amplitude modulatory effect is shown using the calculated correlation coefficient. As expected, with the driving force correction the modulation of PSP amplitude becomes larger for excitatory synapses and smaller for inhibitory synapses (Figure 2.3D; compare solid red and black bars). The net effect of these two factors is that raw (non-corrected) inhibitory PSPs are dramatically increased in magnitude with depolarization (9.38% ± 0.55% per mV, n = 41 in 26 cells, $p < 10^{-3}$), whereas raw excitatory inputs are only modestly amplified (2.79% ± 0.61% per mV, n = 29 in 24 cells, $p < 10^{-3}$). In TTX, the only modulation of PSP amplitude occurs through changes in the driving force. In this case, with the membrane non-linearity largely abolished, raw excitatory synaptic inputs do not change magnitude appreciably with depolarization while raw inhibitory inputs are amplified (-1.58% ± 0.98% per mV for excitation, n = 15 stellate threshold trials in 11 cells, p = 0.13; 5.39% ± 0.55% per mV for inhibition, n = 15 stellate threshold trials in 10 cells, $p < 10^{-3}$). In raw control data, stellate cells in perithreshold membrane voltages showed significantly more modulation relative to TTX trials in both excitatory ($p < 10^{-3}$, n = 29 stellate threshold trials in 24 cells, n = 15 TTX trials in 11 cells) and ($p < 10^{-3}$, n = 41 stellate threshold trials in 26 cells, n = 15 TTX trials in 10 cells) inhibitory trials, reflecting the impedance-driven modulatory effect. Furthermore, PSP modulation was not significantly different from zero in TTX when the changing driving force was taken into account (0.77% ± 0.57% per mV; n = 15 excitatory trials in 11 cells; 15 inhibitory trials in 10 cells; p = 0.18), validating our correction procedure. In all, these results indicate that the ability for GABAergic synaptic inputs to hyperpolarize the membrane is likely to be substantially greater near the peak of an intrinsic MPO when compared to the trough, while the excitatory ability of AMPAergic synapses is only modestly enhanced by the same cyclic depolarization.

In Figure 2.4A, driving force corrected data are shown for both representative stellate and pyramidal neurons (top row), as well as in control conditions. A clear trend is apparent in the PSP amplitude-vs.-membrane-potential relationship, with PSP amplitudes increasing significantly as the neuron is depolarized. In the representative example of a stellate cell near threshold in Figure 2.4Ai, the corrected PSP amplitude increases linearly with depolarization with a 5.90% increase in amplitude per mV of depolarization ($r=0.315$, $p < 10^{-3}$). No such relationship was observed when these measurements were repeated in the presence of 0.5 µM TTX in the same cell in Figure 2.4Aii, which then exhibited a -0.76% decrease in amplitude per mV of depolarization ($r = 0.105$, $p > 0.05$). In a pyramidal neuron of the same cortical region (Figure 2.4Aiii), a

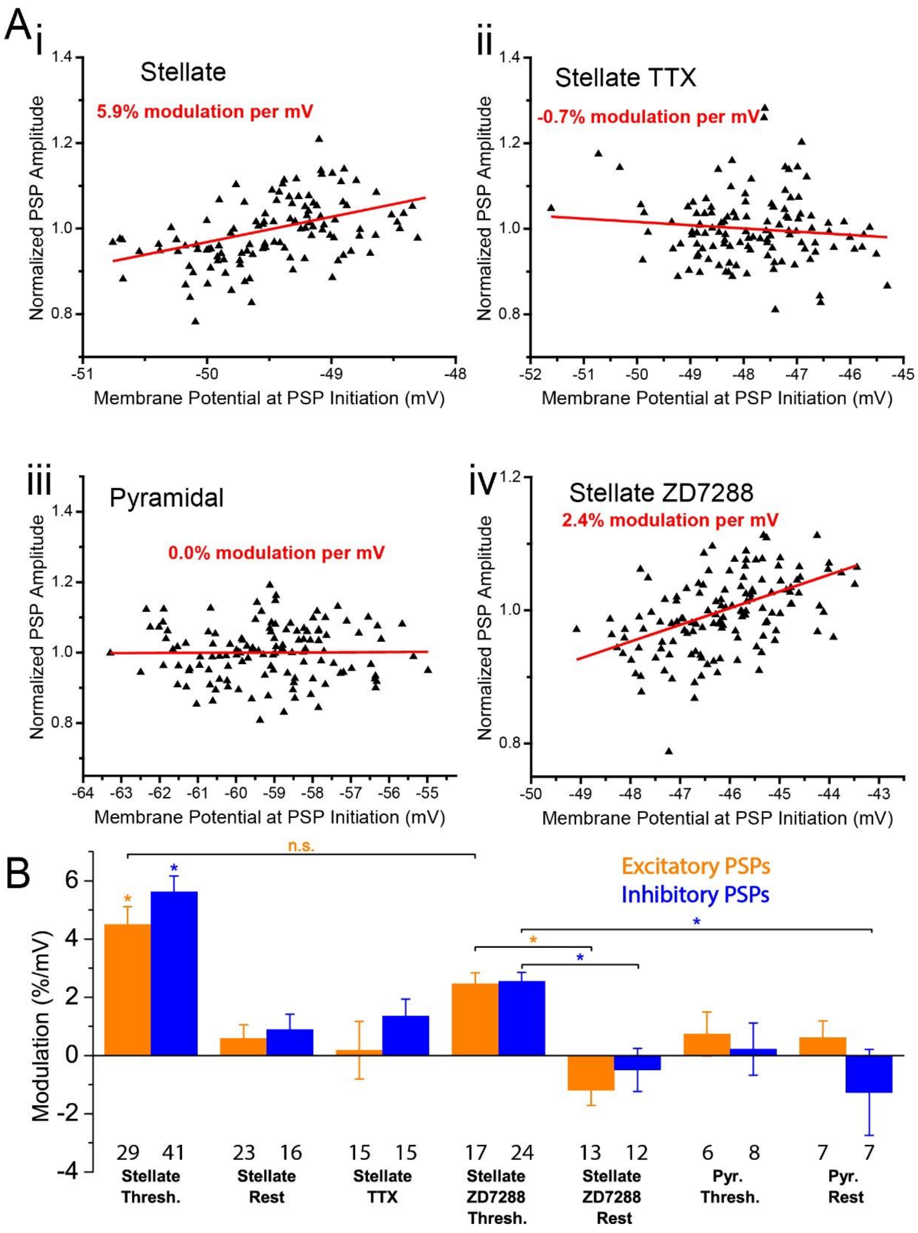

Figure 2.4 Nonlinear integration of artificial synaptic inputs

A Relationship between PSP amplitudes and membrane potential. There is a clear linear trend in stellate neurons near threshold under control conditions (**i**) but not in TTX (**ii**) or in pyramidal neurons (**iii**). For stellate neurons in ZD7288 (**iv**), the effect is reduced, but largely maintained. **B** Summary plots for the percent modulation of excitatory and inhibitory PSP amplitude per mV depolarization under the various conditions described. Stellates cells near threshold are significantly different (in both excitatory and inhibitory) from all other conditions (ANOVA with Tukey test for means, $p < 10^{-2}$) except where otherwise noted. In ZD7288 trials, stellate cells near threshold were significantly different (ANOVA with Tukey test for means, $p < 10^{-2}$) from stellates at rest, for both excitatory and inhibitory trials.

0.04% increase in amplitude per mV of depolarization, $r = 0.009$, $p > 0.05$ was observed. These examples suggest that the modulation of PSP amplitude was indeed likely the result of the voltage-dependence of the stellate neuron impedance. To eliminate the effect of the hyperpolarization activated cation current, I_h (Harris and Constanti, 1995), the effect was also measured in the presence of 20 μM of ZD7288. In Figure 2.4Aiv, a representative sample is shown, exhibiting a 2.37% increase in amplitude per mV of depolarization ($r=0.4682$, $p < 10^{-3}$), suggesting the effect is diminished but maintained.

Across all recorded stellate cells (Figure 2.4B), a significant increase in PSP amplitude was observed at perithreshold membrane potentials (5.15% ± 0.41% per mV; $n = 29$ excitatory trials in 24 cells, 41 inhibitory trials in 26 cells; $p < 10^{-3}$). As expected, such nonlinear integration of synaptic inputs was substantially reduced in these neurons at their resting potential (0.72% ± 0.34% per mV; $n = 23$ excitatory trials in 19 cells, 16 inhibitory trials in 16 cells; $p < 10^{-2}$) and completely absent in the presence of TTX (0.77% ± 0.57% per mV; $n = 15$ excitatory trials in 11 cells, 15 inhibitory trials in 10 cells; $p = 0.18$). In nearby MEC layer II pyramidal neurons, artificial synaptic conductances were integrated linearly; the relationship between PSP amplitude and voltage was nearly flat—after compensating for changes in driving force—near threshold (0.44% ± 0.59% per mV; $n = 6$ excitatory trials in 6 cells, 8 inhibitory trials cells in 7 cells, $p = 0.46$) and at rest (-0.33% ± 0.80% per mV; 7 excitatory trials in 7 cells, 7 inhibitory trials in 8 cells; $p = 0.69$). The I_h current was blocked using ZD7288, and while the effect of membrane potential on PSP amplitude was reduced at threshold (2.51%

± 0.24% per mV; 17 excitatory trials in 11 cells, 24 inhibitory trials in 10 cells; $p < 10^{-3}$), it was only fully eliminated at rest (-0.85% ± 0.44% per mV; 13 excitatory trials in 11 cells, 12 inhibitory trials in 10 cells; $p = 0.07$).

These relationships remain unchanged if excitatory and inhibitory trials are separated and similarly compared across all conditions. Near threshold, excitatory (inhibitory) PSPs increased in magnitude by 4.49% ± 0.62% per mV, $n = 29$ trials in 24 cells, $p < 10^{-3}$ (5.62% ± 0.54%, $n = 41$ trials in 26 cells, $p < 10^{-3}$). On average in stellate neurons, these values were significantly different from all other conditions ($p < 10^{-2}$ for excitatory trials, except compared to stellates in ZD7288 near threshold where $p = 0.17$; $p < 10^{-3}$ for inhibitory trials). In turn, modulation values were near zero under the other conditions: stellates near rest 0.59% ± 0.46% per mV, $n = 23$ trials in 19 cells, $p = 0.21$ (inhibitory PSPs: 0.90% ± 0.53% per mV, 16 trials in 16 cells, $p = 0.11$), stellates in the presence of TTX 0.49% ± 0.99% per mV, $n = 15$ trials in 11 cells, $p = 0.85$ (inhibitory: 1.36% ± 0.57% per mV, 15 trials in 10 cells, $p = 0.03$), pyramidal cells near threshold 0.73% ± 0.76% per mV, $n = 6$ trials in 6 cells, $p = 0.38$ (inhibitory: 0.22% ± 0.90% per mV, 8 trials in 7 cells, $p = 0.81$), and pyramidal cells near rest 0.61% ± 0.58, 7 trials in 7 cells, $p = 0.33$ (inhibitory: -1.27 % ± 1.48% per mV, 7 trials in 8 cells, $p = 0.42$).

These findings bolster the argument that the observed PSP amplification is caused by the voltage dependence of the membrane impedance illustrated in Figure 2.2 which is, in turn, mediated largely by the presence of a substantial persistent sodium conductance. Nevertheless, the impedance spectrum of stellate cells near threshold is in part attributable to I_h (Nolan et al., 2007), so to discriminate the effect of I_h on this modulation, similar trials were performed in the presence of 20 µM ZD7288. Stellate cells in ZD7288 showed subthreshold modulation of 2.47% ± 0.37% per mV, 17 trials in 11 cells, $p < 10^{-3}$ (inhibitory: 2.54% ± 0.31% per mV, 24 trials in 10 cells, $p < 10^{-3}$), whereas at rest the effect was eliminated with modulation of -1.19% ± 0.51, 13 trials in 11 cells, $p < 10^{-2}$ (inhibitory: -.49% ± 0.74% per mV, 12 trials in 10 cells, $p = 0.52$). ZD7288 subthreshold trials were significantly different from their corresponding rest trials ($p < 10^{-3}$ in excitatory trials, $p < 10^{-2}$ in inhibitory trials).

Effects of membrane potential oscillation phase on synaptic integration

Thus far, the effect discussed has been between the corrected PSP amplitude and the membrane potential at which this PSP is elicited. To study the relationship of PSP amplitude to the oscillation phase of stellate cell intrinsic subthreshold oscillations, trials were detrended to account for slow drift in the voltage signal and PSPs were grouped according to their location within the oscillation bands, as in Figure 2.5. The PSPs elicited during the 20% most depolarized membrane potentials were labeled peak phase PSPs, those elicited during the 20% most hyperpolarized were labeled trough phase PSPs, and the PSPs in the central 40% were classified as either rising or falling phase, depending on the voltage change prior to the PSP. The amplitude of PSPs in each group were averaged for each trial and compared using paired-samples t-tests. In excitatory (inhibitory) trials, peak phase PSPs were significantly larger in amplitude than their corresponding trough phase PSPs with a calculated $p < 10^{-2}$,

Figure 2.5 Effect of oscillation phase on synaptic integration
A PSPs were grouped into four different categories: peak, trough, rising and falling phase. Detrended data were divided into bands representing each category: the 20% most depolarized membrane potential were labeled “peak phase” trials, while the 20% most hyperpolarized band were labeled “trough phase” trials. From the middle band representing 40% of the membrane potential range, PSPs following an increase in membrane potential were labelled “rising phase” PSPs; those following a decrease in membrane potential were labelled “falling phase” PSPs. **B** A sample waveform average from one trial showing the PSP-triggered average of all peak phase PSPs and trough phase PSPs. An arrow denotes the beginning of the artificial PSP injection. Shaded region indicates standard error associated with the waveform average. Note the larger magnitude associated with peak phase PSPs relative to trough phase PSPs, as well as the intrinsic MPO preceding the PSP. **C** For each trial, the average PSP amplitude for peak (rising) phase PSPs are compared to the average PSP amplitude for trough (falling) phase PSPs (stellates near threshold, $n = 29$ in 24 cells for excitatory, $n = 41$ in 26 cells for inhibitory; stellates in TTX, $n = 15$ in 11 cells for excitatory, $n = 15$ in 10 cells for inhibitory). Peak phase PSP amplitudes were significantly larger ($p < 10^{-3}$ for both inhibitory and excitatory, paired sample t-test) than their corresponding trough phase PSP amplitudes (i, ii). This effect was eliminated for PSPs in TTX, which showed no significant difference between matched peak vs. trough PSP amplitudes. Rising and falling phase PSPs showed now significant difference in any condition, for neither excitatory nor inhibitory trials.

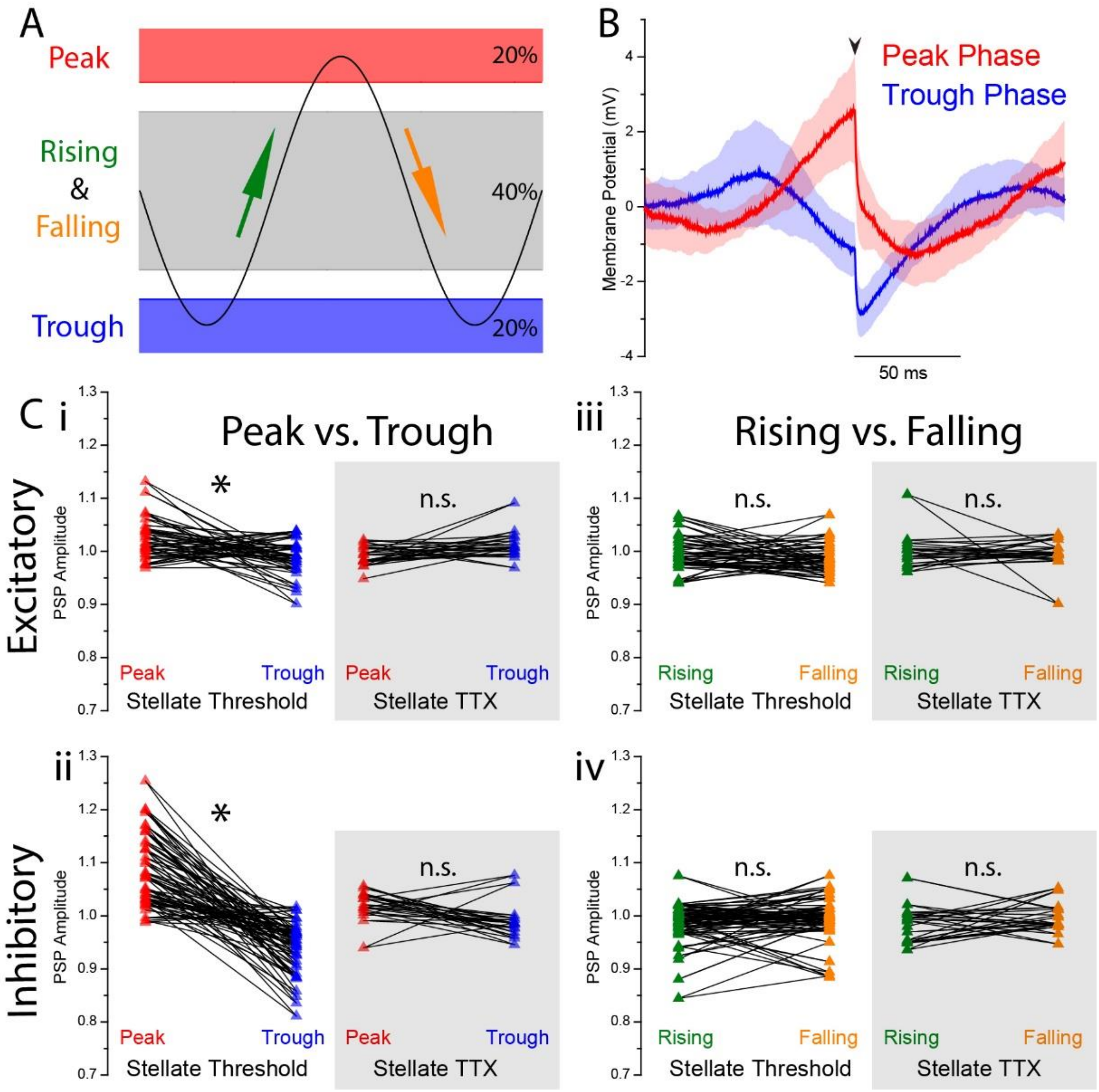
A
Peak
20%
Rising
&
Falling
40%
Trough
20%
B
Peak Phase
Trough Phase
Membrane Potential (mV)
4
2
0
-2
-4
50 ms
C i
Peak vs. Trough
Excitatory
PSP Amplitude
*
n.s.
Peak
Trough
Stellate Threshold
Stellate TTX
ii
Inhibitory
iii
Rising vs. Falling
Rising
Falling
iv
1.3
1.2
1.1
1.0
0.9
0.8
0.7

n = 29 trials in 24 cells (inhibitory: $p < 10^{-3}$, n = 41 trials in 26 cells). In TTX, this peak phase vs. trough phase difference was not significant with a calculated p = 0.07, n = 15 trials in 11 cells (inhibitory: p = 0.08, 15 trials in 10 cells). Rising phase vs. falling phase paired comparisons in stellate excitatory (inhibitory) trials showed no significant difference with a calculated p = 0.23, n = 29 trials in 24 cells (inhibitory: p = 0.28, n = 41 trials in 26 cells); nor did the same comparisons for stellates in TTX with a calculated p = 0.72, 15 trials in 11 cells (inhibitory: p = 0.33, 15 trials in 10 cells). These findings suggest that PSP amplification is more directly a function of membrane voltage and is thus evident at the peak phase of the oscillation (versus the trough), and furthermore that the rising and falling phase do not have different effects on the amplification of synaptic inputs.

Discussion

In agreement with previous studies (Boehlen et al., 2013; Erchova et al., 2004; Nolan et al., 2007), we have demonstrated that the subthreshold impedance of stellate neurons in the MEC layer II is sensitive to voltage and that this dependence is brought about by the successive activation of increasing numbers of non-inactivating, “persistent” sodium channels in response to membrane depolarization. The effect of this nonlinearity is an increase in membrane impedance, particularly near the theta frequency band, as spike threshold is approached (Figure 2.2). Using artificial postsynaptic conductance waveforms introduced during ongoing MPOs with dynamic clamp, we have shown that SCs exhibit voltage-dependent integration of synaptic inputs. Quantitatively, these results indicate that PSP amplitude may be modulated by up to 30-60% by the changing membrane impedance alone during an ongoing synaptically-driven MPO *in vivo*. Voltage-dependent synaptic integration is abolished by blocking Na^+ channels and reduced by blocking HCN channels that underlie the hyperpolarization-activated cation current I_h. Our results complement those showing that SCs at different locations along the dorsal-ventral (DV) axis, and thus associated with different grid periods, process inputs differentially (Garden et al., 2008). Thus while we expect the mechanism described in this paper to not change along the DV axis, the effect is complementary to the increase in resistance along the DV axis described in Garden et al., 2008.

The nonlinear resonance of stellate cells is intriguing in the context of theta-frequency oscillations, which are commonly recorded in the MEC (Kramis et al., 1975; Mitchell and Ranck, 1980; Vanderwolf, 1969) and are accompanied by membrane-potential oscillations (MPOs) at theta frequencies near spike threshold (Domnisoru et al., 2013; Harvey et al., 2009; Quilichini et al., 2010; Schmidt-Hieber and Häusser, 2013). Both stellate cells and pyramidal cells phase lock to the theta rhythm and phase precess (Alonso and García-Austt, 1987; Frank et al., 2001; Hafting et al., 2008; Quilichini et al., 2010), consistent with their high impedances within the theta band. Our data suggest that, due to their impedance spectra having theta-centered resonance, stellate cells may show stronger frequency dependence in their phase locking. Furthermore, given that phase precession seems to be driven by periodic inputs that are faster than the average network activity (Schmidt-Hieber and Häusser, 2013), the cellular mechanisms of phase precession are likely to be identical to those underlying phase locking. This suggests that stellates will also show strong frequency preference in their phase precession.

While much of this study focused on the increase in impedance mediated by slowly inactivating Na^+ channels, we also studied the effect of I_h in the membrane potential-dependent synaptic integration. I_h plays a prominent role in stellate cells electrophysiological dynamics (Dickson et al., 2000; Fernandez et al., 2013; Haas et al., 2007; Nolan et al., 2007; Richter et al., 2000), and its deactivation as the membrane potential is depolarized could contribute to the effect described in this paper. Experiments using ZD7288, an I_h blocker, maintained the effect relative to rest, but reduced the mean percent modulation per mV from approximately 5% to 2.5%. This suggests that the I_h deactivation approaching threshold could play a role in voltage-dependent synaptic integration, and that the increased low frequency impedance associated with eliminating I_h (Nolan et al., 2007) would reduce the impedance differential in the membrane voltage range studied here. It is also possible that ZD7288 introduces off target effects on sodium channels, and that the effect observed here is due to these off-target effect rather than through the block of I_h (Wu et al., 2012).

In addition to amplification by increasing subthreshold impedance, PSP amplitudes are also affected by changes in driving force as the membrane potential varies. For glutamatergic excitation, with a reversal potential of about 0 mV, a 1 mV depolarization of membrane potential will produce a roughly 2%

decrease in synaptic current due to the change in driving force alone. Although estimates of the reversal potential of $GABA_A$ channels vary considerably (Khirug et al., 2008; Vida et al., 2006; Woodruff et al., 2010), the effects of either shunting or hyperpolarizing $GABA_A$ channels will be enhanced near threshold (e.g., by 4-5% if E_{GABA} = -75 mV). Effects of driving force combine approximately linearly with the effects of nonlinear impedance (Figure 2.3D).

In this study, we have limited measurements and analysis to the dynamics of only the neuronal cell body. It is possible that the characteristics we describe here are substantially different at distal dendritic locations. However, a large number of inhibitory synapses are located on the cell body or at proximal dendritic sites of principal cells in the hippocampal formation (Freund and Buzsáki, 1996), indicating that the effects of nonlinear impedance are likely relevant for physiological inhibitory synaptic inputs in the intact brain. As excitatory inputs may arrive at more distal locations and because the density of sodium channels has been found to decrease with distance along dendritic processes in other cell types (Hu et al., 2010; Jarsky et al., 2005), it is possible that excitatory synaptic inputs are affected by the membrane nonlinearity to a lesser degree (Stuart and Sakmann, 1995).

The nonlinearity we describe here is likely present in any neuronal population possessing a substantial persistent sodium conductance below spike threshold, due to the simplicity of this mechanism. Neurons in the thalamus, neocortex, hippocampus, and cerebellum express such a conductance prominently (Crill, 1996), and for this reason one may presume that synaptic inputs are integrated in all of these cells in a manner that is nonlinear and depends significantly (5-10% / mV) on membrane voltage when engaged in oscillatory or other activity in which membrane potential traverses a large range of values.

The results we describe here should have substantial effects in vivo, on three time scales. On the time scale of crossings through one of the cells' periodically spaced place fields, SCs exhibit sustained depolarizations lasting seconds (Domnisoru et al., 2013; Schmidt-Hieber and Häusser, 2013). Our results suggest that the effects of both excitation and (especially) inhibition are enhanced during these in-field periods, making the SCs easier to drive but also making it easier for inhibition to modulate this drive. On the time scale of the theta cycle (hundreds of ms), we would expect both the excitation arriving during the depolarizing phase, and any inhibitory inputs that help terminate the depolarizing phase, to be enhanced by nonlinear membrane impedance. Thus, the nonlinearity in the membrane may enhance the quality of phase locking to the network theta rhythm. Finally, on the time scale of short trains of action potentials (10 ms), membrane nonlinearity may serve as an additional form of negative feedback, amplifying the effects of inhibition. As the temporal lobe in general and the superficial entorhinal cortex in particular represent common foci for epileptic seizures (Bartolomei et al., 2005; Engel and Pedley, 2008; Spencer and Spencer, 1994), it is not unreasonable to expect that neurons in this area have developed numerous negative feedback mechanisms to regulate excitability.

Collaborator contributions

The work in this chapter was completed in collaboration with Michael N. Economo at the University of Utah. MNE conceived of the study, collected a portion of the data, and wrote the scripts used in the initial analysis. Joan José Martínez Castillo collected a majority of the data, expanded the analysis to include separate excitatory and inhibitory components, added the input phase analysis, wrote scripts to analyze the data, and performed the statistical tests contained in the chapter. This chapter has been published in the journal *Hippocampus* (Economo et al., 2014) as a shared first author publication between MNE and JJMC. The initial submitted text was written by MNE; changes to the text in response to reviewers were done by JJMC. Figure 2.1 was prepared by MNE; Figures 2.2, 2.3, 2.4, and 2.5 were prepared by JJMC.

CHAPTER 3

INTERNEURON FORM AND FUNCTION IN THE SUPERFICIAL MEC

Introduction

By modulating the activity of principal neurons, interneurons play a crucial role in the spatial navigation function of the superficial medial entorhinal cortex (Buetfering et al., 2014; Couey et al., 2013; Domnisoru et al., 2013; Garden et al., 2008; Pastoll et al., 2013; Varga et al., 2010). Among other findings, recent studies have demonstrated that MEC GABAergic interneurons mediate stellate-to-stellate cell communication (Couey et al., 2013) and the superficial layers of the MEC exhibit higher inhibitory synaptic input onto principal cells than the deeper layers (Woodhall et al., 2005). Grid cell computation work has implemented inhibition-dominated network models to simulate spatial navigation mechanisms (Burak and Fiete, 2009; Thurley et al., 2013), although a recent study has argued against the notion that interneurons provide location dependent input onto grid cells (Buetfering et al., 2014).

Despite their importance, electrophysiological data for GABAergic interneurons remain scarce (Gloveli et al., 1997; Wolansky et al., 2007). The characterization of superficial MEC interneurons has been difficult for two reasons: the low proportion of interneurons (approximately 10%) compared to principal cells (Gatome et al., 2010) and the relative physiological and anatomical diversity of cortical interneuron populations (Buzsáki et al., 2004; DeFelipe et al., 2013; Maccaferri and Lacaille, 2003; Whittington and Traub, 2003). Previous research suggests that the superficial MEC is anatomically diverse, containing at least seven anatomical categories as defined by soma depth and dendritic morphology (Canto et al., 2008). The anatomical differences in the interneuron population are likely to coincide with different roles within the local cortical circuit (Kepecs and Fishell, 2014). Nevertheless, only limited data exist on the electrophysiological profiles of the superficial MEC interneuron population (Gloveli et al., 1997; Wolansky et al., 2007; Wouterlood et al., 1995).

This study takes advantage of recent developments in transgenic techniques that specifically label GABAergic interneurons in order to systematically characterize the superficial MEC interneuron population both electrophysiologically and anatomically. Acute brain slices were harvested from GAD2+ and PV+ labeled transgenic mice and whole cell patch clamp techniques were used to measure a variety of electrophysiological features. Posthoc anatomical reconstruction was then conducted using fluorescence staining and 2-photon imaging to couple each interneuron’s electrophysiological profile with its MEC localization and axonal tree distribution. We find that superficial MEC interneurons can be grouped into four separate groups that have distinct anatomical and electrophysiological profiles. These categories include deep-projecting layer 2/3 slow-firing interneurons, layer 2/3 projecting fast-spiking interneurons, layer 1/2-projecting interneurons and layer 1-projecting superficial interneurons. To our knowledge, these findings are the first to systematically characterize superficial MEC interneurons into these four distinct categories.

Materials and methods

Electrophysiology

All electrophysiology experiments were conducted according to protocols approved by the University of Utah Animal Care and Use Committee. Brain slices were harvested from 18-35 day old transgenic mice. Two transgenic strains were used: cre-dependent GAD2-IRES-tdTomato transgenic mice (Taniguchi et al., 2011, strain 010802, The Jackson Laboratories; Bar Harbor, ME), which labeled glutamic acid decarboxylase 2 gene (GAD2) expressing cells and thus facilitated targeting of GABAergic cortical interneurons; and PV-tdTomato transgenic mice (Hippenmeyer et al., 2005, strain 008069, The Jackson Laboratories; Bar Harbor, ME), which labeled all parvalbumin (PV) expressing cells and thus facilitated targeting of the specific PV+ genotype in inhibitory interneurons. These mice were anesthetized with isoflurane and decapitated. The brain was then harvested, chilled in sucrose-substituted artificial cerebrospinal fluid (ACSF, units in mM, 185 sucrose, 2.5 KCl, 1.25 NaH_2PO_4, 10 $MgCl_2$, 25 $NaHCO_3$, 12.5 Glucose, 0.5 $CaCl_2$), and cut parasagittally into 300 µm thick slices using a vibrating microtome (Vibratome VT1200, Leica; Buffalo Grove, IL). Slices were incubated for 15 min in ACSF (units in mM, 125 NaCl, 2.5 KCl, 1.25 NaH_2PO_4, 10 $MgCl_2$, 25 $NaHCO_3$, 25 Glucose, 2 $CaCl_2$) at 37°C, and then allowed to recover for at least 30 min at room temperature. For recordings, slices were transferred to a heated (32-34°C) slice chamber (Warner Instruments; Hamden, CT) that is mounted on an upright microscope stage (Olympus BX53; Olympus, Tokyo, Japan) and perfused with 95/5 percent O2/C02 ACSF. GAD2+/PV+ neurons were visualized using fluorescence and whole-cell patch clamp clamped using patch pipettes (5-6 MΩ) fabricated from borosilicate glass (1.5 O.D. 1.1 I.D.; Sutter Instruments; Novato, CA) and filled with artificial intracellular fluid (ICF, units in mM, 120 K-Gluconate, 5 $MgCl_2$, 0.2 EGTA, 10 HEPES, 20 KCl, 7 di(tris) phosphocreatine, 4 Na_2ATP, 0.3 Tris-GTP) loaded with biocytin (1% by weight) for posthoc reconstruction. Presented data were not corrected for the junction potential, assumed to be 10-12 mV. Cells were patched for at least 30 min to ensure complete biocytin fill. Following electrophysiological trials, brain slices were perfused in 4% paraformaldehyde for 16-24 hours, then washed in phosphate-buffered saline (units in mM, 137 NaCl, 2.7 KCl, 10 Na_2HPO_4, 1.8 KH_2PO_4) three times for 15 min each and stored in 4° C for later staining.

Posthoc anatomical reconstruction

To reconstruct the anatomy of patched cells, brain slices were incubated for 3 hr in a PBS solution containing 3 µg/mL streptavidin Alexa 488 (Molecular Probes; Eugene, OR) and 2% Triton X-100 (by volume). Slices were then washed in PBS three times for 15 min each and mounted on slides using a Mowiol mounting medium. At least 24 hr after mounting, slides were imaged using a two-photon microscope (Ultima Intravital, Bruker Corporation; Billerica, MA), with excitation wavelength set to 810 nm and a 520 nm low-pass filter. Alexa 488-filled cells were localized in the brain slice and a z-stack of 585 µm x

585 µm raster-scanned images was acquired, covering the entire range of the soma and neuronal processes (usually 100-200 µm). This z-stack was projected onto a single composite image and endowed with a dark-cell, light-background look-up table to aid axonal visualization. In order to describe the anatomical features of each neuron, soma depth was measured and the extent of the axonal tree was described with a rectangular approximation using the z-projected image, reducing the anatomical decription to these two anatomical features.

Electrophysiological protocols and data analysis

All electrophysiological protocols were conducted in current clamp and were performed within 30 min of breaking the cell membrane to engage the whole cell patch clamp recording.

Input resistance, time constant, and sag ratio

A bias current was applied in current clamp to polarize the cell to -70 mV. Five 2 sec negative current pulses (with a 2 sec rest time) were injected to hyperpolarize the cell to approximately -80 mV (between -20 pA and -50 pA, depending on input resistance). The resulting steady-state voltage was divided by the applied current to calculate the input resistance. To determine the falling time constant, the time from the beginning of the pulse to reaching 63% of the most hyperpolarized membrane potential was measured. The sag ratio was determined by dividing the maximum voltage hyperpolarization (the sag) by the steady state voltage during the pulse.

Action potential (AP) half-width, AP rise time, and spike afterhyperpolarization (AHP)

A depolarizing bias current was inserted to elicit action potentials just above firing threshold. The average of 50-100 total action potentials recorded in a 30-40 sec recording were used to describe the action potential shape. First, the AP half-width was determined by measuring the AP height (from the action potential upstroke to the peak) and calculating the time between passing the half-height on the depolarizing phase and passing the half-height on the hyperpolarizing phase is the AP half-width. The AP rise time was calculated as the time required for the action potential to go from 20% of its total height to 80% of its total height. The afterhyperpolarizing potential (AHP) was measured as the membrane potential difference between the AP upstroke initiation and the most hyperpolarized membrane potential immediately following the AP.

Firing threshold

The cell was hyperpolarized to -80 mV and a 50 pA/s current ramp for 10-20 sec, depending on the input resistance. The membrane potential at which the first action potential was observed was labeled the firing threshold.

Impedance

The cell was hyperpolarized to -80 mV and a 15 sec white noise current trace (approximately 5 mV in amplitude) was injected. The voltage trace was divided by the injected current trace and the resulting trace was plotted in the frequency domain using a fast Fourier transformation. This procedure was repeated several times at increasing membrane potentials until the cell was depolarized to its firing threshold. The impedance change was measured by calculating the average impedance between 1-10 Hz for the most depolarized trace (labeled “perithreshold”) and dividing it by the average impedance for the –80 mV trace in the same frequency band.

Frequency-current gain and peak firing rate

A bias current was applied in current clamp to polarize the cell to -70 mV. A series of one-second current pulses (with a four-second rest between pulses) were injected to determine the frequency-current (F-I) relationship of the cell. These current pulses ranged from -100 pA to up to 1500 pA, depending on what current amplitude was required to reach a firing rate plateau, and were introduced in 20 nA increments. The peak firing rate was the fastest firing frequency recorded during the F-I trial. A linear regression fit to all points between the first non-zero frequency-current point and the peak firing rate point was calculated with the least-squares ‘polyfit’ function in MATLAB for a first order polynomial. The slope of this fit was taken to be the F-I gain.

Grouping methodology

Principal component analysis

Principal components analysis (Jolliffe, 2002) was used to emphasize variation within the electrophysiological/anatomical dataset. The electrophysiological features used for this analysis were: input resistance, peak firing rate, AP half-width, change in impedance, and F-I gain. The anatomical features used were: soma depth, the most superficial extent of the axonal tree, the deepest extent of the axonal tree, and the axonal width. All these features were z-scored (i.e., mean-subtracted and divided by the standard deviation) prior to the analysis. Each cell was treated as an observation with each feature a variable. The ‘princomp’ function in MATLAB was used to calculate the transformation.

K-means clustering analysis

K-means clustering analysis (MacQueen, 1967) was used on the first four principal components of the above data set in order to group cells. The ‘kmeans’ function in MATLAB was used with 100 iterations for each operation to ensure the most optimal solution is achieved. Silhouette scores were calculated using the ‘silhouette’ function in MATLAB. The silhouette score is a measure of similarity of a point to points within its own cluster and of dissimilarity of a point to points outside of its own cluster (Rousseeuw, 1987). For a given cell i, it is calculated as $s(i) = (b(i)-a(i))/\text{maximum}[a(i),b(i)]$, where $a(i)$ is the average distance between cell i and all other cells in its cluster and $b(i)$ is the shortest distance between cell i and any cell not in i's cluster. The range of values ranges from -1 to 1. A higher score (closer to 1) indicates high similarity within cluster and dissimilarity outside of cluster, whereas a lower score (closer to -1) indicates low similarity within cluster and dissimilarity outside of cluster (suggesting the data point was misclassified).

Group comparisons

When comparing electrophysiological and anatomical features among different cell groups, reported p values were calculated using a one-way ANOVA with a Tukey test for means. For each feature in each group, a Kolmogorov–

Smirnov normality test was performed to ascertain that all compared distributions were normal.

Results

Interneuron characterization

Interneurons of the mouse superficial medial entorhinal cortex were systematically patched, electrophysiologically characterized, and then anatomically reconstructed in order to better understand the local inhibitory components of this brain region. Because interneurons make up a small (<10%) portion of all the medial entorhinal cortex, transgenic mice labeling GAD2+ and PV+ cells are used to target the neuron subpopulation. For each interneuron, passive properties (like input resistance at rest, time constant, and sag ratio) and active properties (like action potential shape and frequency-current relationships) are measured in the current clamp configuration (Figure 3.1A), and then the neuron is stained posthoc with an Alexa 488 fluorescent marker. The neuron is then reconstructed in a three dimensional z-stack using a 2-photon microscope (Figure 3.1B). In all, each neuron had ten electrophysiological features and four anatomical features recorded.

The study yielded a total of 122 interneurons with complete electrophysiological and anatomical profiles. Of these, 96 cells were acquired using GAD2+ mice and 26 were acquired in PV+ mice. Cells that had incomplete or inadequate electrophysiological trials were discarded. Common causes of incomplete electrophysiological characterization included cell death during experiment, incomplete pipette to cell seal, and noise artifacts that corrupted the

Figure 3.1 MEC interneuron electrophysiological and anatomical characterization

Ai Depolarizing current is injected to elicit firing and resulting action potentials (AP) are characterized. AP half-widths are measured at half the height of the AP (using the AP initiation upstroke, or “knee,” as the base). The duration between passing the half-height on the depolarizing phase and passing the half-height on the hyperpolarizing phase is the AP half-width. The afterhyperpolarizing potential (AHP) is measured as the membrane potential difference between the AP “knee” and the most hyperpolarized membrane potential immediately following the AP. **ii** One-second long hyperpolarizing pulses are injected to hyperpolarize the cell from -70 mV to approximately -80 mV. The resulting voltage deflection ΔV is divided by the injected current ΔI to calculate the input resistance. The sag ratio was defined as ΔV /(sag+ ΔV). **iii** The frequency-current (F-I) relationship was described injecting progressively increasing current pulses and measuring the resulting firing rate. The slope between the first non-zero F-I trial and the peak firing trial is the F-I gain. The fastest firing rate elicited by the current pulses is the peak firing rate. **iv** The impedance spectra are measured at both -80 mV and near threshold are used to calculate the impedance change. The impedance between 1 Hz and 10 Hz of the perithreshold spectrum is divided by the same impedance band of the rest spectrum. The dashed line indicates the upper band for the impedance change calculation, 10 Hz. **Bi** A z-stack projection of a biocytin filled, Alexa 488 labelled MEC interneuron is used to determine the location of the soma and estimate the extent of the axonal tree. **ii** The neuron in Bi is described using a diamond to indicate the depth of the soma (relative to the pial surface) and a rectangle to describe the laminar and columnar extent of the neuron’s axonal projection, both in red. Dashed line indicate the average depth of layers 1, 2, and 3. This neuron has a soma at the layer 1/2 border (approximately 200 μm deep), and its axonal tree extends from approximately 170 μm to 350 μm in depth and is approximately 500 μm wide.

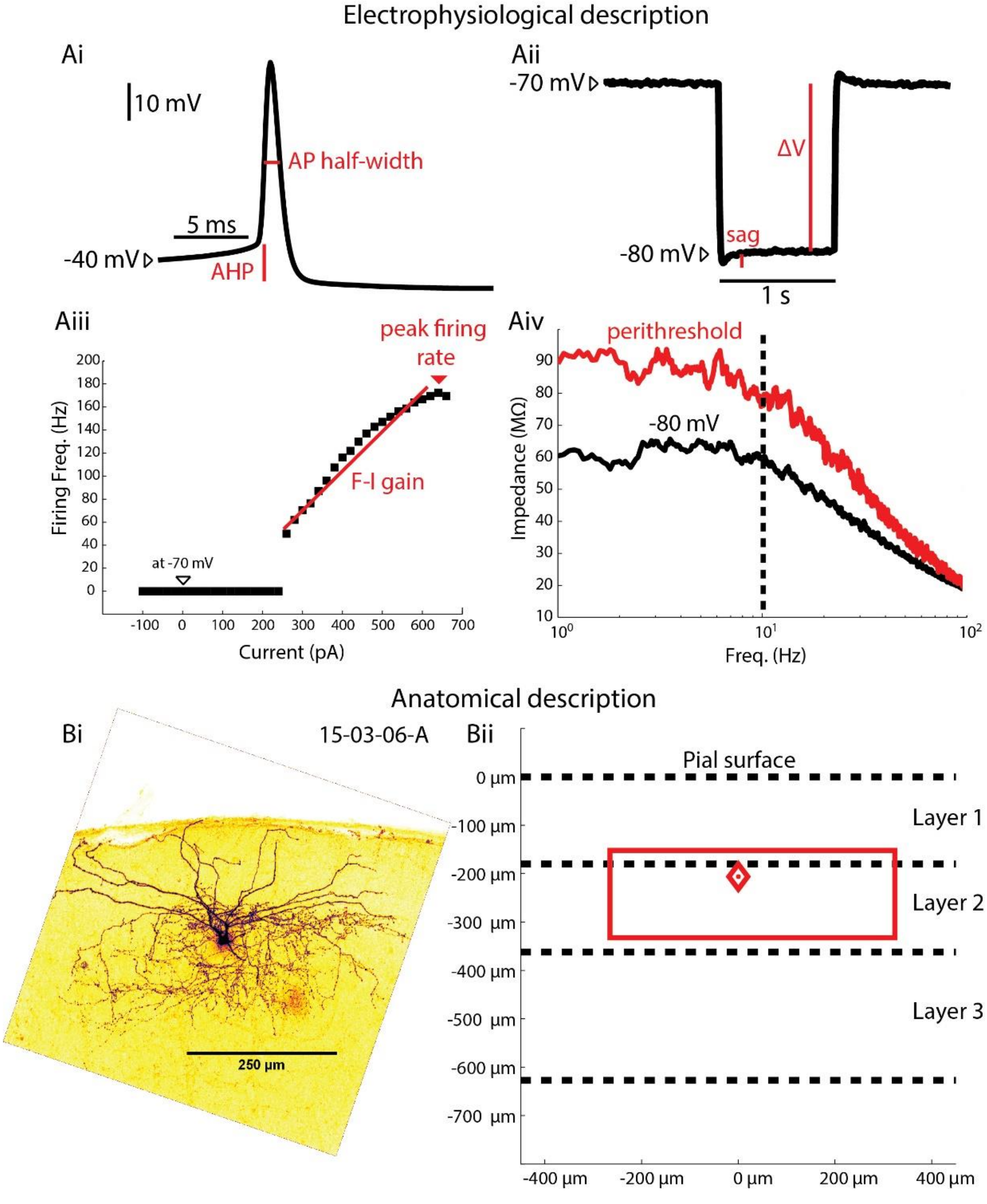
Electrophysiological description
Ai
10 mV
AP half-width
5 ms
-40 mV
AHP
Aii
-70 mV
ΔV
sag
-80 mV
1 s
Aiii
peak firing rate
Firing Freq. (Hz)
F-I gain
at -70 mV
Current (pA)
Aiv
perithreshold
-80 mV
Impedance (MΩ)
Freq. (Hz)
Anatomical description
Bi
15-03-06-A
250 µm
Bii
Pial surface
0 µm
-100 µm
-200 µm
-300 µm
-400 µm
-500 µm
-600 µm
-700 µm
Layer 1
Layer 2
Layer 3
-400 µm
-200 µm
0 µm
200 µm
400 µm

data acquisition. Cells that had incomplete anatomical reconstructions, particularly those where the axonal tree was not visible, were also discarded. Common issues with anatomical reconstruction included incomplete anatomical fills and inadequate staining.

Classifying interneurons into distinct groups

Given that the large data set included 122 interneurons each with 10 electrophysiological features and 4 anatomical features, principal components analysis (PCA) was used to isolate the variation of the data into fewer dimensions. PCA was conducted using 9 selected electrophysiological and anatomical measurements (see Materials and Methods). Since this diverse set of measurements vary greatly in mean and variance, all measurements were z-scored to standardize the PCA variables to a mean of 0 and variance of 1. To reduce the dimensionality of the data set, in further analyses used only the top four ranked principal components, which altogether accounted for 79.6% of the variance in the data. The relationships among the four principal components have been plotted in Figure 3.2A.

The resulting principal components were then used to group cells into distinct clusters. K-means clustering analysis was performed as described previously. Given that k-means clustering requires the number of clusters as an input, it was necessary to determine the optimal number of clusters to divide the data set. K-means clustering was thus conducted on using various cluster number inputs, ranging from only 2 clusters to up to 16 clusters. For each cluster number input, a silhouette score was calculated for all cells. The silhouette score

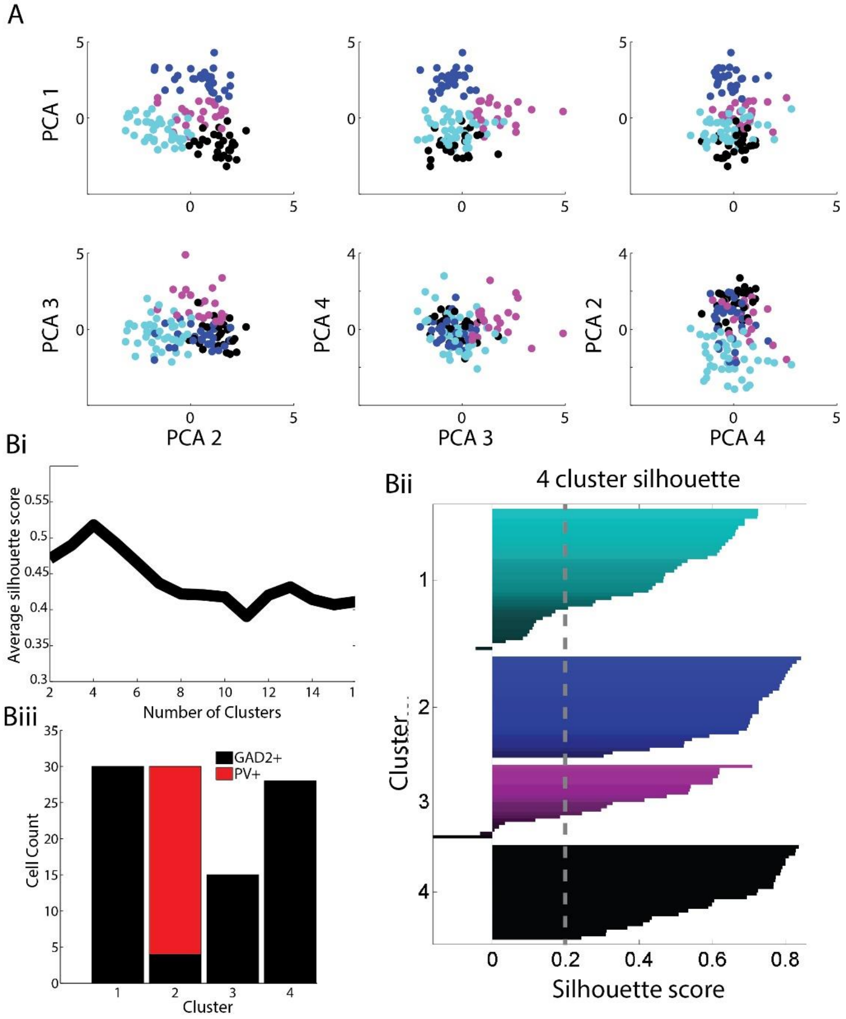

Figure 3.2 Principal component and k-means clustering analysis
A The first four principal components of combined electrophysiological and anatomical data are plotted in all possible combinations. These four principal component dimensions were used to conduct k-means clustering analysis. Cluster 1 is cyan, cluster 2 is blue, cluster 3 is magenta and cluster 4 is in black. **Bi** In order to determine the optimal number of clusters for k-means clustering, the average silhouette score (measure of distance for within-cluster points compared to outside-of-cluster points) was calculated for k-means clustering analyses using between 2 and 16 clusters. The highest silhouette score was achieved using 4 clusters, suggesting that this is the optimal cluster number. **ii** The silhouette value (score) for each point is shown in their corresponding cluster. Low or negative silhouette values indicate points that fit poorly within its cluster. For further analyses, points with silhouette values lower than 0.2 (indicated by the dashed gray line) were discarded. **iii** In a 4 cluster analysis, parvalbumin positive (PV+) cells were located entirely in cluster 2, with 26 out of 30 cells being PV+. This again suggests that using 4 clusters for the k-means clustering analysis is optimal.

is a measure of the cluster “fit”; it is high when a data point (in this case a cell) is more similar to data points within its cluster than those outside of its cluster. The average silhouette score for all 122 interneurons in each of the 2-16 cluster k-means analyses was calculated to validate the cluster “fit,” as shown in in Figure 3.2Bi. The highest mean silhouette score was achieved when four clusters were assigned to the data set, suggesting that the data set is most optimally clustered when the cluster number input is four.

The silhouette scores four the 4 cluster analysis are shown in Figure 3.2Bii. In order to optimize the clustering analysis, cells with silhouette scores less than 0.2 (shown in a gray dashed line in Figure 3.2Bii) were discarded from further analysis. This reduced the data set from 122 interneurons to 105 interneurons. The resulting GAD2-PV cell distribution for these clusters is shown in Figure 3.2Biii. Clusters 1 and 2 have a total of 30 cells each, cluster 3 has 15 cells, and cluster 4 has 28 cells. Notably, the k-means clustering analysis placed all 26 PV+ cells in the data set into cluster 2. The fact that all PV+ cells were placed in a single cluster and that the cluster itself was almost entirely (26 out of 30, 87%) comprised of verified PV+ cells lends further support to the PCA/k-mean clustering method used in this study. This result also suggests that PV+ cells represent a relatively small fraction of the fluorescent cells in the GAD2 mice.

Description of the four interneuron groups

Assigned groups express distinct electrophysiological/ anatomical profiles

As shown on Table 3.1 and Figure 3.3, the clustering method classified the data set into four interneuron groups with distinct anatomical and

Table 3.1 Electrophysiological and anatomical characteristics for all 4 interneuron clusters with statistical comparisons

Cluster	1	2	3	4	Analysis of variance pairwise test	1,2	1,3	1,4	2,3	2,4	3,4
Input resistance (MΩ)	205.9	89.3	294.7	168.6							
	12.8	6.1	22.9	8.3		p<0.01	p<0.01	p<0.05	p<0.01	p<0.01	p<0.01
Time constant, falling (ms)	13.27	5.34	19.38	15.50							
	0.80	0.29	2.76	4.99		p<0.01	p<0.01	n.s.	p<0.01	p<0.05	n.s.
Firing threshold (mV)	-39.3	-36.5	-41.2	-35.9							
	0.7	1.0	1.1	1.0		p<0.05	n.s.	p<0.01	p<0.01	n.s.	p<0.01
A.P. rise time (ms)	0.275	0.196	0.251	0.306							
	0.005	0.005	0.014	0.007		p<0.01	n.s.	p<0.01	p<0.01	p<0.01	p<0.01
A.P. half-width (ms)	1.124	0.536	0.784	1.224							
	0.034	0.014	0.052	0.042		p<0.01	p<0.01	n.s.	p<0.01	p<0.01	p<0.01
Spike AHP (mV)	16.0	19.8	19.5	19.0							
	1.0	0.5	0.9	0.8		p<0.01	p<0.05	p<0.05	n.s.	n.s.	n.s.
Frequency-current gain (Hz/pA)	97.1	282.0	409.4	157.7							
	13.0	15.3	48.2	18.6		p<0.01	p<0.01	p<0.01	p<0.01	p<0.01	p<0.01
Peak firing rate (Hz)	45.1	274.5	120.6	64.9							
	4.8	9.6	7.3	5.7		p<0.01	p<0.01	p<0.01	p<0.01	p<0.01	p<0.01
Change in impedance (%)	56.6	134.7	140.8	48.7							
	9.5	12.4	14.1	10.1		p<0.01	p<0.01	n.s.	n.s.	p<0.01	p<0.01
Sag ratio	0.935	0.946	0.900	0.934							
	0.006	0.004	0.015	0.009		n.s.	p<0.05	n.s.	p<0.01	n.s.	p<0.05
Soma depth (µm)	320.3	308.2	294.7	169.5							
	14.6	15.1	19.5	7.5		n.s.	n.s.	p<0.01	n.s.	p<0.01	p<0.01
Axonal tree, deep (µm)	-298.7	-162.8	-105.2	-79.1							
	22.5	17.4	32.7	22.9		p<0.01	p<0.01	p<0.01	n.s.	p<0.01	n.s.
Axonal tree, superficial (µm)	439.5	285.3	338.4	214.7							
	19.8	13.1	36.6	23.5		p<0.01	p<0.05	p<0.01	n.s.	p<0.01	p<0.01
Axonal tree, width (µm)	366.7	512.2	440.8	495.1							
	22.7	12.5	32.1	19.3		p<0.01	n.s.	p<0.01	p<0.05	n.s.	n.s.

The electrophysiological and anatomical characteristics of all 4 clusters are shown, along with the associated p-values from a one-way analysis of variance test (as described in Materials and Methods). Each row shows the average value for a different electrophysiological or anatomical measurement. The standard error associated with that measurement is located below the average value. Each column for the left half of the table shows the measurements for each of the 4 clusters. On the right half of the table, the p-value for the one-way ANOVA test is shown for matched pairs. For example, column “1,2” shows the p-values for the test between clusters 1 and 2 for each characteristics. P-values less than 0.05 are highlighted in blue. Tests that showed no significance are shown as “n.s.”

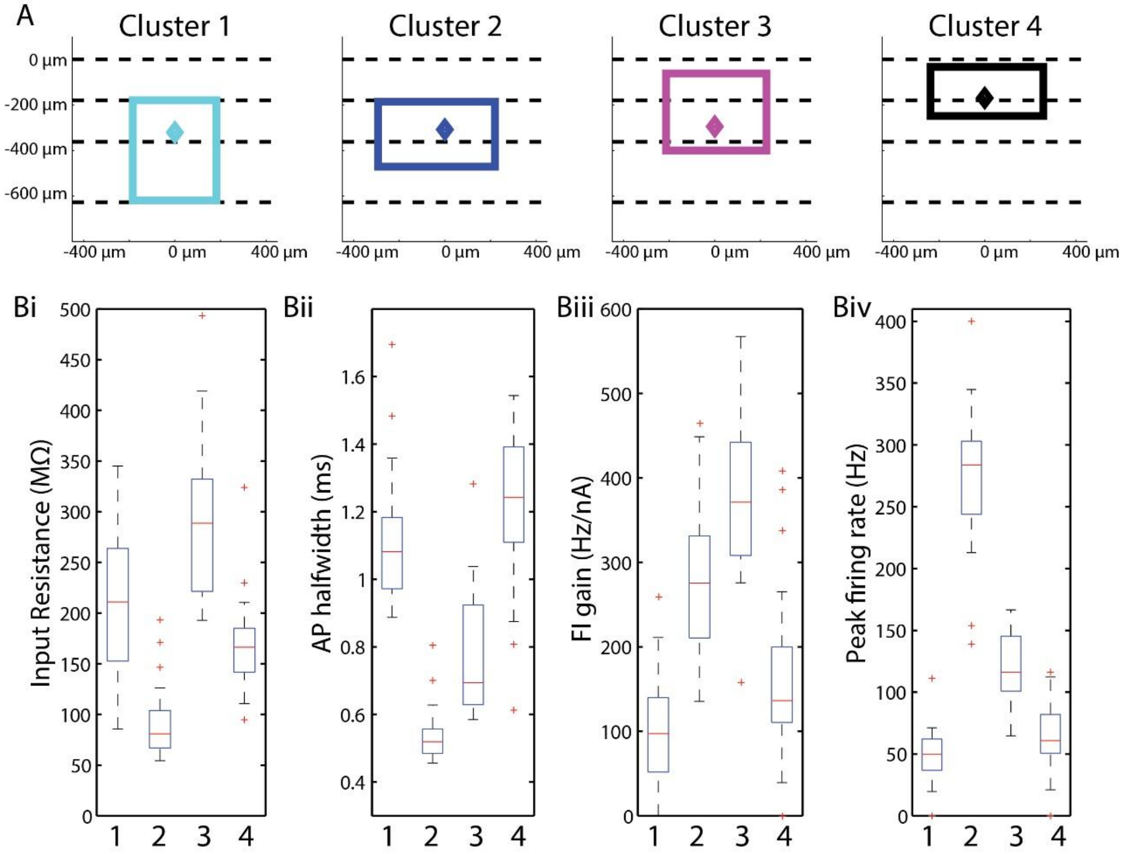

Figure 3.3 Anatomical and electrophysiological summary data for 4 clusters
A The average anatomical characteristics for each cluster are displayed in the same abstract form as in Figure 3.1Bii. The average soma depth is shown as a diamond, and the average axonal tree extent is shown as a rectangle. Cluster 1 shows an average soma depth in the layer 2 with axonal projections to layers 2 and 3. Cluster 2 shows an average soma depth also in layer 2 with axonal projections mostly restricted to layer 2. Cluster 3 shows an average soma depth in layer 2 with axonal projections in layers 2 and 3. Cluster 4 shows an average soma depth in the layer 1/2 border, with axonal projections mostly in layer 1. **B** Several electrophysiological characteristics are described for each cluster. All electrophysiological characteristics and relevant statistical tests are described in Table 3.1. **i** Input resistance is shown in megaohms. Clusters 2 and 4 were lower relative to clusters 1 and 3. **ii** AP halfwidth is show in ms. Cluster 2 interneurons had the fastest AP half-widths of all clusters. **iii** FI gain is shown in hertz per nanoamp. Clusters 2 and 4 had steeper FI gains than clusters 1 and 4. **iv** The peak firing rate is shown in hertz. Cluster 2 had the fastest peak firing rate of all clusters.

electrophysiological profiles. Figure 3.3A shows the average soma depth and the average axonal tree extent for each cluster. The average soma depth varies slightly among clusters, with most of the variance being within cortical layer 2. The average axonal extent, however, is distinct among clusters, with each cluster projecting to a different range of cortical layers. Figure 3.3B shows the distribution (in box plot form) for various electrophysiological characteristics: input resistance (3.3Bi), AP half-width (3.3Bii), F-I gain (3.3Biii), and peak firing rate (3.3Biv). Overall, no 2 clusters show similar electrophysiological profiles; although for certain features two clusters may have distributions with substantial overlap, the combination of electrophysiological features for each cluster is unique. The complete statistical comparisons for both electrophysiological and anatomical features are shown in
Table 3.1.

Cluster 1: layer 2/3-projecting slow-firing interneurons

Cluster 1 interneurons (n = 30) have somas throughout layers 2 and 3, with an average depth of 320.3±14.6 μm. Their axonal projection reach layers 2 and 3, and their average axonal extent is the deepest of all clusters at 298.7±22.5 μm ($p<0.01$) for its most superficial extent and 439.5±19.8 μm ($p<0.01$) for its deepest extent. The average axonal width is the narrower ($p<0.01$) than Cluster 2 and 4 at 366.7±22.7 μm. Several examples of this interneuron cluster are shown in Figure 3.4, with all somas and axonal trees shown in Figure 3.4A and 2-photon reconstructions in Figure 3.4Bi-vi.

The most salient electrophysiological feature of the layer 2/3-projecting

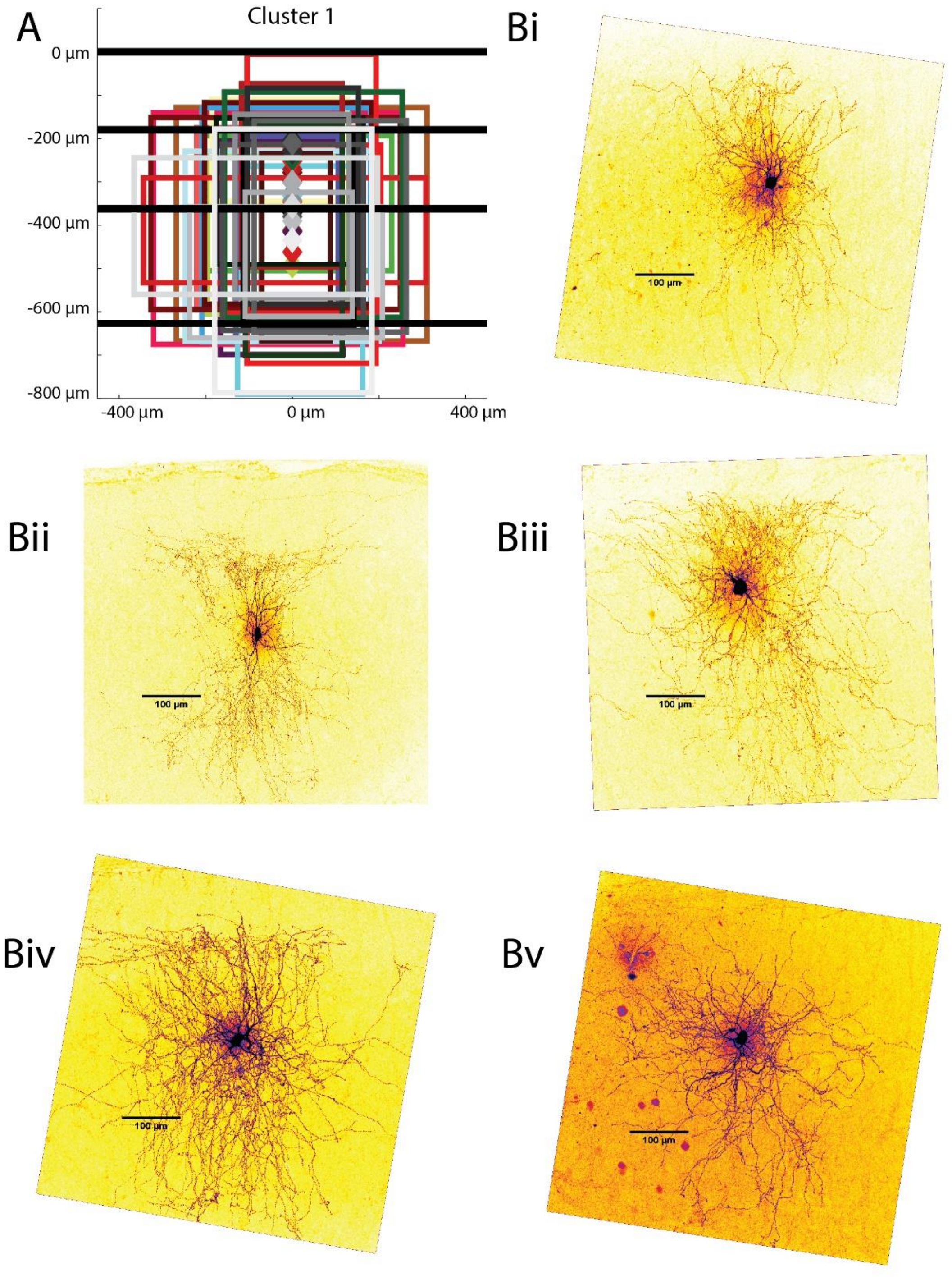

Figure 3.4 Examples of Cluster 1 interneurons
A Anatomical characteristics for all cells in Cluster 1 are shown in the same abstract form as in Figure 3.1Bii. **Bi-v** Z-stack projections of Cluster 1 Alexa 488 labelled MEC interneurons are shown as examples.

Cluster 1 interneurons is their slow firing rate and flat frequency-current relationship. The interneurons in this cluster had both the flattest F-I gain at 97.1±13 Hz/nA ($p<0.01$) and the slowest peak firing potential at 45.1±4.8 Hz ($p<0.01$) of all clusters. The average input resistance of Cluster 1 interneurons is 205.9±12.8 MΩ, the second highest and most significantly different than all other clusters ($p<0.05$). The average time constant is 13.3±0.8 ms significantly longer than Cluster 2 ($p<0.01$) and shorter than Cluster 3 ($p<0.01$) but not significantly different to Cluster 4. The average firing threshold is -39.3±0.7 mV significantly more polarized than Clusters 1 and 4 ($p<0.01$). The AP rise time for Cluster 1 interneurons averaged at 0.275±0.005 ms, and its AP half-width was 1.124±0.034 ms, significantly greater than Clusters 2 and 3 ($p<0.01$). Cluster 1 had the shallowest spike AHP of all clusters at 16.0±1.0 mV ($p<0.01$). It has a smaller change in impedance between -80 mV and the perithreshold region than Clusters 1 and 2 ($p<0.01$), with an average percent change was 56.6±9.5 (%). The average sag ratio for the interneurons of this cluster is 0.935±0.006.

Cluster 2: layer 2/3-projecting fast-firing interneurons

Cluster 2 is the only cluster to contain PV+ interneurons, which comprise 26 out of the 30 cells in this group. Figure 3.5A shows all axonal trees for this cluster. Figure 3.5Bi-vi shows several examples of 2-photon reconstructions. Their somas are located throughout layers 2 and 3, with an average depth of 308.2±15.1 μm. Like Cluster 1, Cluster 2 axonal projections are located mainly throughout layers 2 and 3. The most superficial/deepest axonal projections are on average 162.8±17.4 μm and 282.3±13.1 μm respectively, which places it

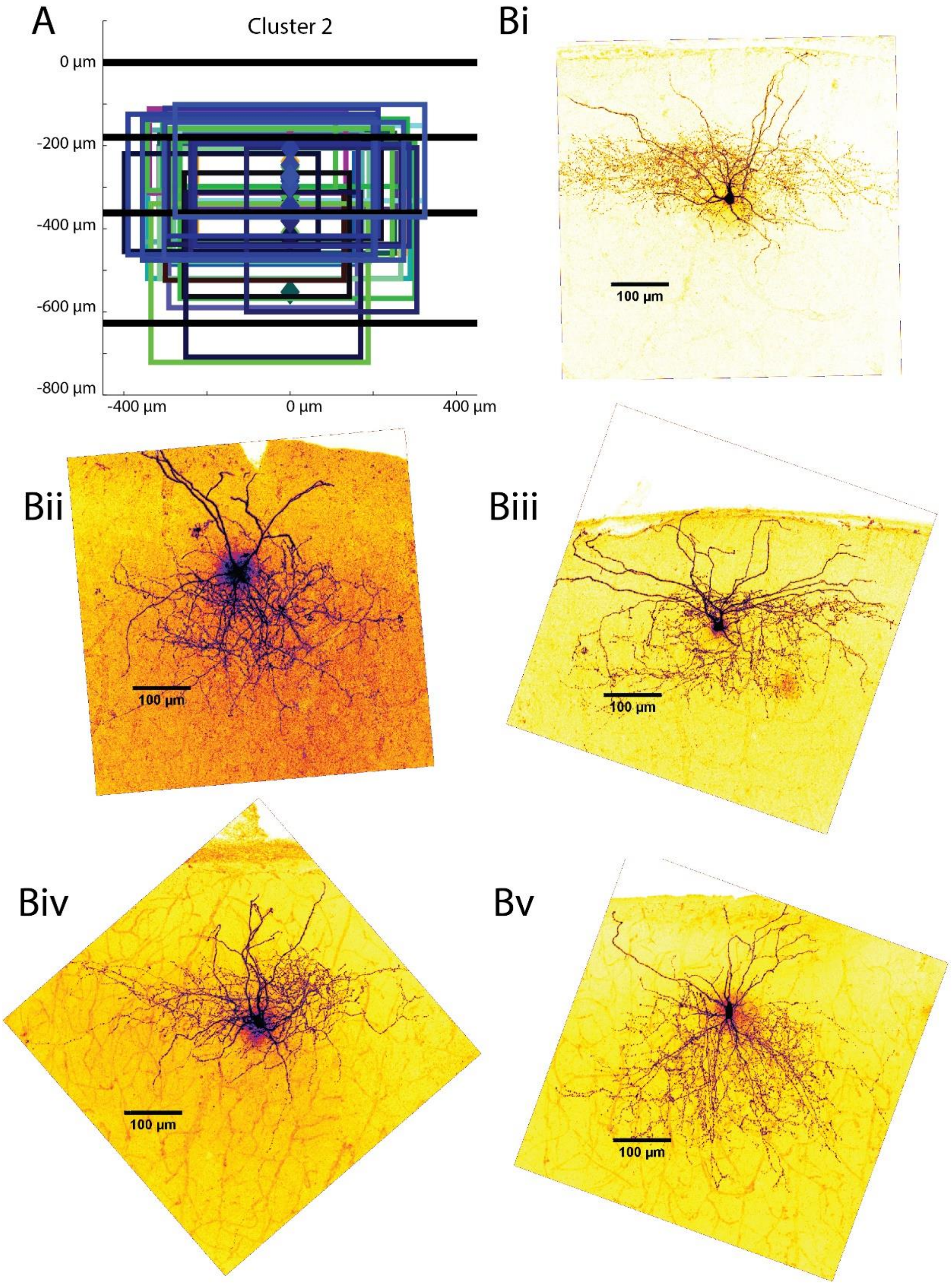

Figure 3.5 Examples of Cluster 2 interneurons
A Anatomical characteristics for all cells in Cluster 2 are shown in the same abstract form as in Figure 3.1Bii. **Bi-v** Z-stack projections of Cluster 2 Alexa 488 labelled MEC interneurons are shown as examples.

significantly deeper than Cluster 4 cells ($p<0.01$) but more superficial than Cluster 1 cells ($p<0.01$). Average axonal width is 512.2±12.5 μm.

Cluster 2 interneurons are predominantly fast-spiking, in agreement with previous findings on PV+ cells (Jones and Bühl, 1993). The interneurons in this cluster have a very fast peak firing rate of 274.5±9.6 Hz, significantly faster than all other clusters ($p<0.01$) and 228% greater than the next fastest spiking cluster (Cluster 3 at 120.6±7.3 Hz). The average input resistance of Cluster 2 interneurons is 89.3±6.1 MΩ, by far the lowest of all clusters ($p<0.01$). The time constant is also faster than all other clusters ($p<0.01$) at 5.34±0.29 ms; as are the AP half-width (0.536±0.014 ms, $p<0.01$) and the AP rise time (0.196±0.005, $p<0.01$). Its 19.8±0.8 mV spike AHP is similar to Clusters 3 and 4, significantly greater only than Cluster 1. Despite its fast firing rate, the frequency-current gain is only the second highest of the four clusters at 282.0±15.3 Hz/nA, less than Cluster 3 but greater than Cluster 1 and 4 ($p<0.01$ for all comparisons). The percent change in impedance exhibited in Cluster 2 neurons is 134.7±12.4 (%), similar to Cluster 3 but greater than Clusters 1 and 4 ($p<0.01$). The average sag ratio is 0.946+0.004.

Cluster 3: layer 1/2-projecting interneurons

Cluster 3 interneurons ($n=15$), like the first two clusters, have somas throughout layers 2 and 3 as shown in Figure 3.6. The average soma depth in Cluster 3 is 294.7±19.5 μm. Cluster 3 axonal projections extend mainly through layers 1 and 2. The average axonal extent of Cluster 3 interneurons is similar to Cluster 2 at 105.2±32.7 μm in its superficial extent and 338.2±36.6 μm in its deep

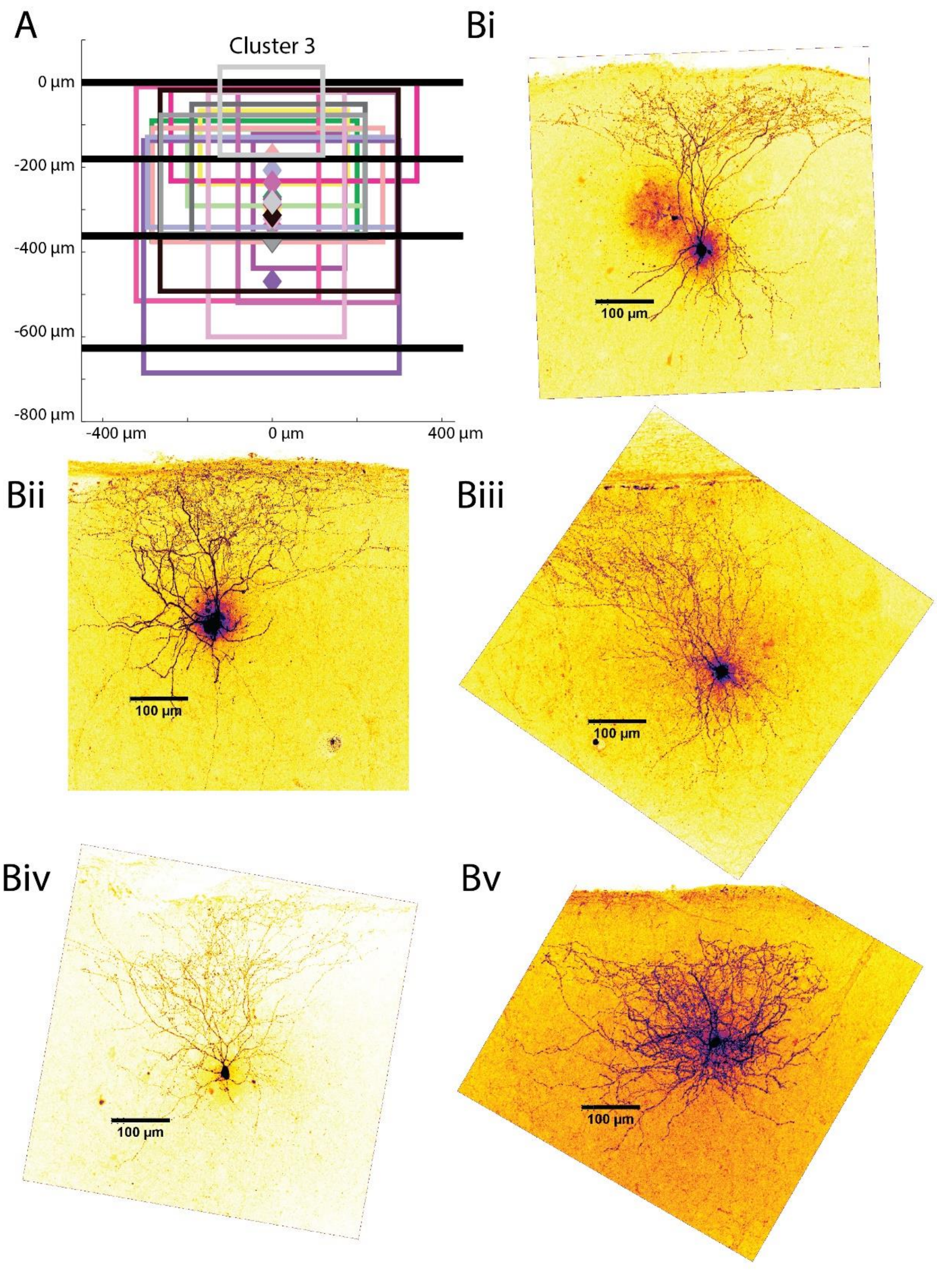

Figure 3.6 Examples of Cluster 3 interneurons
A Anatomical characteristics for all cells in Cluster 3 are shown in the same abstract form as in Figure 3.1Bii. **Bi-v** Z-stack projections of Cluster 3 Alexa 488 labelled MEC interneurons are shown as examples.

extent (deeper than Cluster 4 and more superficial than Cluster 1, $p<0.01$). Its anatomical profile is different from Cluster 2 only in that its axonal tree is narrower ($p<0.01$) at 440.8±32.1 μm, compared to 512.2±12.5 μm. Cluster 3 is the smallest cluster, having only 15 cells. All the axonal trees for this cluster are shown in Figure 3.6A, and several 2-photon reconstruction examples are shown in Figure 3.6Bi-vi.

Cluster 3 interneurons have the highest input resistance (294.7±22.9 MΩ) of any cluster ($p<0.01$). Due in part to this high input resistance, Cluster 3 interneurons also have the steepest F-I gain of all clusters at 409.4±48.2 Hz/nA ($p<0.01$). The average time constant is 19.38±2.76, greater than Clusters 1 and 2 ($p<0.01$). The firing threshold is -41.2±1.1 mV, more polarized than Clusters 2 and 4 ($p<0.01$). The AP half-width (0.784±0.052 ms) is significantly different from all other clusters, greater than Cluster 2 but less than Clusters 1 and 4 ($p<0.01$ for all comparisons). The AP rise time is 0.251±0.014 ms, and the spike AHP 19.5±0.9 mV. The peak firing rate is 120.6±7.3 Hz, faster than Cluster 1 and 4 but slower than Cluster 2. The change in impedance for Cluster 3 is 140.8±14.1 (%). Cluster 3 has the lowest sag ratio at 0.900±0.015 ($p<0.01$), the only sag ratio to be significantly different compared to other clusters.

Cluster 4: layer 1-projecting interneurons

Cluster 4 interneurons (n=28) have the most superficial somas of any cluster ($p<0.01$), as can be seen in Figure 3.7. At an average soma depth of 169.5±7.5 μm, Cluster 4 interneuron somas are located throughout layers 1 and 2. This cluster's axonal projections are mainly limited to layer 1, with its average

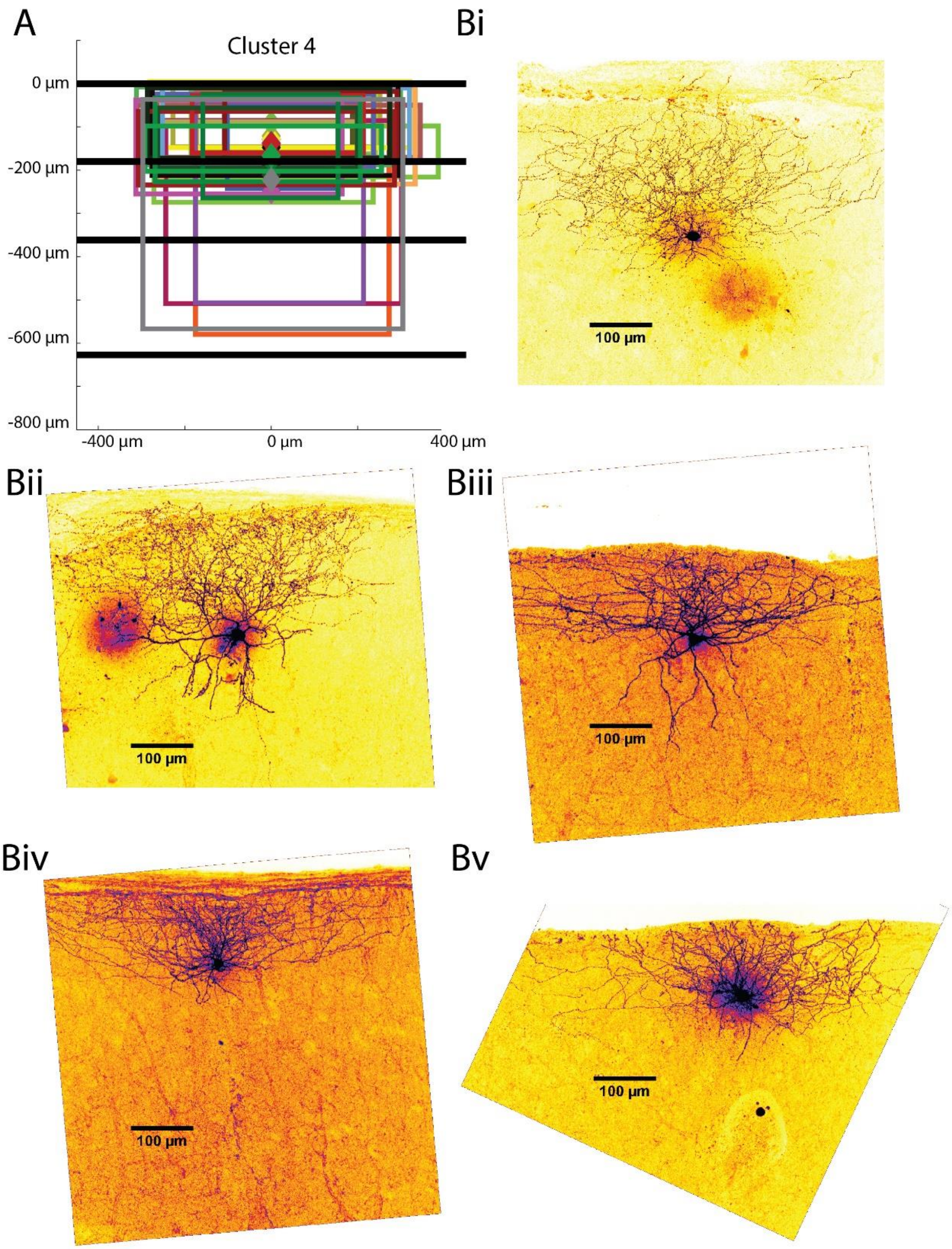

Figure 3.7 Examples of Cluster 4 interneurons
A Anatomical characteristics for all cells in Cluster 4 are shown in the same abstract form as in Figure 3.1Bii. **Bi-v** Z-stack projections of Cluster 4 Alexa 488 labelled MEC interneurons are shown as examples.

deepest axonal extent being the most superficial of all clusters (214.7±23.5 μm, $p<0.01$). The average most superficial axonal extent is 79.1±22.9 μm and the axonal width is 495.1±19.3 μm. The entire population of somas and axonal extents is shown in Figure 3.7A, and several examples of 2-photon reconstructions for Cluster 4 interneurons are shown in Figure 3.7Bi-vi.

Most of the electrophysiological features for these layer 1-projecting interneurons do not lie at either extreme among the clusters. Input resistance is 168.6±8.3 MΩ, greater than Cluster 2 ($p<0.01$) but less than Clusters 1 ($p<0.05$) and 3 ($p<0.001$). The average F-I gain is 157.7±18.6 Hz/nA and peak firing rate is 64.9±5.7 Hz, both greater than Cluster 1 but less than Clusters 2 and 3 ($p<0.01$ for all comparisons). The Cluster 4 average time constant is 15.5±4.99 ms, and firing threshold is -35.9±1.0 mV. The action potential shape is unique in having the slowest AP rise time of all clusters (0.306±0.007 ms, $p<0.01$). The AP half-width is 1.224±0.042 ms, greater than those of Clusters 2 and 3 ($p<0.01$). The spike AHP is 19.0±0.8 mV. The percent change in impedance is 48.7±10.1 (%), lower than Clusters 2 and 3 ($p<0.01$). Finally, the sag ratio for Cluster 4 is 0.934±0.009.

Discussion

Having systematically characterized 122 interneurons in the superficial MEC, we have found that this interneuron population is best classified into four distinct groups, based on their anatomical and electrophysiological characteristics. In anatomical classifiers, the laminar extent of axonal projection and the somatic depth of interneurons were emphasized. For electrophysiological classification, input resistance, AP half-width, peak firing rate, frequency-current gain, and changes in impedance were used. The resulting interneuron groups are layer 2/3-projecting, slow-firing neurons; layer 2/3-projecting fast-firing neurons (mainly PV+); layer 1/2-projecting interneurons; and layer 1-projecting interneurons.

The clustering method for interneuron data used principal component analysis to reduce the 10-dimensional parameter space into four orthogonal dimensions (principal components) with maximized variance (Jolliffe, 2002). Multidimensional clustering was then performed on the first four principal components and silhouette scores were used to determine optimal cluster number. This method is similar to previous approaches to neuronal classification (Cauli et al., 2000; Dumitriu et al., 2006; Helm et al., 2013; Krimer, 2005). This study is the first, to our knowledge, to combine both anatomical and electrophysiological characteristics in the analysis, as opposed to using only electrophysiological data (Helm et al., 2013; Krimer, 2005) or conducting clustering analyses for different types of data separately and evaluating correlations (Cauli et al., 2000; Dumitriu et al., 2006). This method is often used to differentiate between cell types within distinct molecular subgroups, such as parvalbumin-positive or somatostatin-positive interneurons (Halabisky, 2006; Ma, 2006; McGarry, 2010). Because our dataset included cells from the general GAD2+ population and the specific molecular PV+ subgroup, the clustering method was particularly effective at differentiating different anatomical/electrophysiological profiles.

Previous immunostaining work has found that PV+ interneurons make up approximately 50% of the GAD+ population in the superficial MEC (Miettinen et al., 1996). However, analysis of the GAD2+ interneurons characterized in this cluster found a very small percentage of interneurons exhibiting characteristic PV+ electrophysiological/anatomical profiles. The clustering analysis yielded only 4 interneurons out of 96 that were taken to be anatomically and electrophysiologically similar to PV+ interneurons by being placed in Cluster 2. This discrepancy may be explained by issues in the transgenic technique used in this study. PV+ cells may also have been preferentially lost during slicing as compared to GAD2+ cells. GAD2+/tdTomato fluorescence in PV+ neurons may have been lower than in neighboring cells, discouraging patching of PV+ cells. Fortunately, the addition of separate PV+ transgenic animals into the study compensated in part for the relative paucity of PV+ in the GAD2+ patched cell population.

The interneurons of Cluster 1 have somas located throughout layers 2 and 3; their axonal projections reach into layers 2 and 3, with some neurons having axons projecting into the *lamina dessicans* (layer 4). Previous anatomical studies have identified MEC layer 2/3 interneurons with similar anatomical characteristics as pyramidal-looking interneurons (Kumar and Buckmaster, 2006), multipolar cells (Gloveli et al., 1997), and bipolar cells (Wouterlood et al., 2000). Pyramidal-looking interneurons in the MEC layer 3 described by Kumar and Buckmaster (2006) have axonal projections mostly concentrated around the cell body in layer 3 and projecting superficially in layer 2, a feature present in some Cluster 1 cells (see Figure 3.5A). They are described as having high input resistance (382±47 MΩ), whereas the population average for Cluster 1 neurons is also high relative to other clusters (205.9±12.8 MΩ). Gloveli et al. (1997) in turn describes pyramidal-looking interneurons in MEC layer 3 as having much lower input resistances of 50.6±5 MΩ, although they maintained their previously mentioned layer 2/3 axonal projections. The relatively low input resistances measured by Gloveli et al. (1997) are likely due to their use of sharp electrodes (as opposed to the patch electrodes used in this study), which have been shown to reduce the input resistance in a cell by 20-40% (Li, 2004). Overall, these results suggest that a significant portion of Cluster 1 cells are pyramidal-looking interneurons. Multipolar cells are described similarly by Gloveli et al. (1997), with a low input resistance of 36.8±3.3 MΩ. Unlike the pyramidal-looking interneurons, the axonal projections of these interneurons project further into layer 2 and can project onto layer 1, in addition to projecting intralaminarly in layer 3. This cell type contains somatostatin (SOM) and cholecystokinin (CCK) positive cells (Wouterlood and Pothuizen, 2000), and like the pyramidal-looking interneuron is also likely represented within the Cluster 1 population. Finally, MEC layer 3 bipolar cells described by Wouterlood et al. (2000) may be included in the Cluster 1 population as the cells having narrower axonal widths that can project deeper into the *lamina dessicans*. Cluster 1 neurons account for the superficial MEC's deeper-projecting interneurons that generally have lower firing rates and low frequency-current gains. This differentiates them from the fast-firing layer 2/3-projecting interneurons and suggests that they play different roles in local circuit modulation.

The second cluster described in this study is made up almost entirely of PV+ interneurons. The 4 out of 30 cells that are not verified to be PV+ may indeed be PV+, as the GAD2+ marker also covers the PV+ cell population (Miettinen et al., 1996). In the MEC, the population of PV+ neurons with somas located in layer 2 (as is the case with most Cluster 2 neurons) contains basket cells and chandelier cells (Canto et al., 2008). Basket cells in the MEC were first described by Jones and Bühl (1993), who through unaided patching over several years successfully characterized 12 basket cells, both anatomically and electrophysiologically. In the anatomical description, they described cells with axonal projection mostly within layer 2, as we see for Cluster 2 neurons. Electrophysiologically, they described the PV+ interneurons as fast-spiking, and Cluster 2 neurons are the fastest spiking population in the present corpus. Additionally, the basket-like interneurons had action potential half-width as 0.51 + 0.05 ms, very similar to the AP half-width of Cluster 2 neurons at 0.536 + 0.014 ms. Finally, the cells in Cluster 2 were very likely to exhibit type 2 discontinuous frequency-current relationship (data not shown), a feature which has often been associated with fast-spiking PV+ cells (Mancilla et al., 2007). These cells are likely to make up the bulk of the Cluster 2 interneuron population. MEC horizontal chandelier cells, named for their vertically oriented axonal aggregations, have been described having a vertical axonal extent 100-200 µm long (Cluster 2 average is approximately 120 µm); the horizontal extent is usually 250-350 µm wide (Cluster 2 average is 512.2±12.5 µm, although some are narrower than 350 μm) (Soriano et al., 1993). By visual inspection, chandelier cells comprise a smaller fraction of the cells in Cluster 2 than basket cells.

Clusters 1 and 2 have similar anatomical distributions (axonal projections mainly in layers 2 and 3) and so are mainly distinguished by their temporal dynamics. Cluster 1 cells express slower firing rates, flatter F-I gains and a greater time constant than Cluster 2 cells. What role might these two interneuron populations play in the superficial MEC? First, fast-firing PV+ neurons like those in Cluster 2 have already been shown to mediate stellate-to-stellate cell connectivity (Couey et al., 2013), provide grid cell-driven recurrent inhibition to the local circuit (Buetfering et al., 2014), and drive theta-nested gamma oscillations (Pastoll et al., 2013). Second, cortical circuits throughout the brain receive a large dynamic range of excitatory inputs, input which is then balanced by an increase in inhibitory inputs (Borg-Graham et al., 1998; Monier et al., 2003; Wehr and Zador, 2003). This coordination occurs over a large dynamic range, meaning the inhibitory dynamics of each circuit is capable of matching excitatory input across this same temporal range. The existence of slow-firing (Cluster 1) and fast-firing (Cluster 2) inhibitory interneurons with axonal projections within the same layers may thus serve to provide enough sensitivity and dynamic range to address the heterogeneous multimodal inputs that the MEC receives, facilitating the spatial navigation functions that have been described in layers 2 and 3. Third, optogenetic stimulation of either the PV+ cell populations (as in Cluster 2) and SOM+ populations (as are likely present in Cluster 1) have been shown to produce ictal discharges *in vitro* in the superficial MEC (Yekhlef et al., 2015). Kumar and Buckmaster (2006) also showed that rats treated with pilocarpine showed reduced levels of these two cell types, which directly resulted in hyper-excitability of layer 2 stellate cells. The cells of both Clusters 1 and 2 may thus also play an important role in epilepsy.

Cluster 3 interneuron somas are mainly located in the layer 2 somas and have axonal projections into layer 1 and layer 2. Anatomical studies have described MEC and lateral entorhinal cortex cells with similar anatomical characteristics as multiform neurons, with axons similarly projecting into the white matter (layer 1) and intralaminarly in layer 2 (Tahvildari and Alonso, 2005). Electrophysiological characterization of these cells in the LEC by Tahvildari and Alonso (2005) showed cells with similar time constants (19.38±2.76 ms in this study, where they showed 20.7±1.32 ms) and peak firing rates (120.6±7.3 Hz compared to approximately 125±30 Hz). The average firing threshold they measured in the LEC was slightly more depolarized (-45.8±0.5 mV) than that measured in this study in the MEC (-41.2±1.1 mV); input resistance was also considerably lower in the LEC (55.7±6.85 MΩ) than in the MEC (294.7±22.9 MΩ), though our study used pipette tips of much lower resistance (~6 MΩ versus 80-120 MΩ). The cells of Cluster 3 may therefore be related to the multiform cells electrophysiologically characterized in the LEC and anatomically described in the MEC, although to our knowledge they were never previously described electrophysiologically. Being the cluster with the smallest sample size and most heterogeneous anatomical distribution, it is difficult to ascertain what role Cluster 3 interneurons may play in the MEC. They have the second fastest peak firing rate and steepest F-I gain to the PV+ Cluster 2 cells. Given that Cluster 3 and Cluster 4 both project into layer 1, the relatively slower firing rate of Cluster 4 cells suggest that these two populations play the same fast/slow complementary role that Clusters 1 and 2 play in layers 2 and 3, increasing the range of inhibitory responses available to respond to excitatory inputs.

The fourth cluster describes cells with somas in layer 1 (near the layer 1/2 border) and axonal projections mostly restricted to layer 1 with a horizontal extent on average 495.1±19.3 µm. Neurons with these anatomical characteristics have been previously described as both horizontal cells (Germroth et al., 1989) and multipolar cells (Wouterlood et al., 2000). Horizontal cells have been shown to express cholecystokinin (CCK) in the MEC (Schwerdtfeger et al., 1990), whereas layer 1 multipolar cells in the MEC have been described as calretinin (CR) positive (Wouterlood et al., 2000). Both cells have been described as having at least one axonal projection into the deeper layers of the MEC, a feature that was observed in several examples of the Cluster 4 neurons. Although Canto and Witter (2012) electrophysiologically characterized layer 1 horizontal and multipolar MEC neurons, their study was focused on principal cells and discarded interneuron-like cells (with shorter AP half-widths) from their analysis. Therefore, to our knowledge, this is the first characterization of these GABAergic, MEC-layer 1 projecting cells. Layer 1 interneurons have been suggested to play a delayed feedback role in cortical computation (Zhou and Hablitz, 1996). Basically, as excitatory inputs arrive from other brain regions and excite pyramidal cells and stellates cells in layers 2 and 3, interneurons in layer 1 may also be excited (either directly by the excitatory inputs or indirectly via principal cells) and inhibit the dendritic branches of the superficial MEC principal cells. Given the great width of their axonal projections, it is possible that input to one of these layer 1 cells has an effect on a wide area. These may mean inhibitory input onto other layer 1 cells (disinhibition) or inhibitory input onto the dendrites of principal cells in other cortical columns. Further work would be required to understand the specific role these layer 1-projecting Cluster 4 neurons play in the MEC.

Supplement

Alternative clustering approaches

In addition to the combined data k-means clustering method used in this study, we explored several different approaches to the clustering problem. First, we used hierarchical clustering to group the interneuron population and compared the results to those arrived at using k-means clustering. Second, we explored clustering the interneurons using either anatomical data or electrophysiological data, as opposed to combining both data types into one analysis.

Methods

Hierarchical clustering

The first four principal components of the combined anatomical/ electrophysiological data set (5 electrophysiological measures and 4 anatomical measures) were clustered using the unweighted pair group method with arithmetic mean (UPGAM) for hierarchical clustering (Sokal, 1958), using the least squared Euclidean distance to separate interneurons. As this method sequentially separates the population into different hierarchies, it is possible from one analysis to group interneurons into a few large clusters or several smaller clusters. For the purposes of comparing our results to those of k-means clustering, the cutoff for differentiating clusters was set to 57% of the maximum distance between any 2 interneurons. That is, all interneurons within a single cluster have to be no further than 57% of the maximum distance measured in this population; interneurons with a greater distance must be in separate clusters.

Anatomical and electrophysiological clustering

We separated out the 4 anatomical and 5 electrophysiological measures and conducted separate analyses. To reiterate, the electrophysiological features used for this analysis were input resistance, peak firing rate, AP half-width, change in impedance, and F-I gain. The anatomical features used were soma depth, the most superficial extent of the axonal tree, the deepest extent of the axonal tree, and the axonal width. For both sets of data, we z-scored the measurements and conducted PCA analysis, as described in the Materials and Methods section. For k-means clustering analysis, we set the cluster number to four, to match with the optimal cluster number for the combined analysis.

Correspondence between different clustering distributions

To compare different distributions, it was necessary to determine the optimal correspondence between clusters of one distribution to that of the combined k-means clustering distribution used in the study. We established the optimal correspondence by testing every possible permutation for assignment overlap (percentage of interneurons assigned to the same cluster in both distributions), and choosing the permutation of highest overlap.

Results

K-means clustering versus hierarchical clustering

We conducted UPGAM hierarchical clustering on the same 4-dimensional principal component anatomy/electrophysiology data used for k-means clustering in the study. This separated the 122 interneuron population into the dendrogram in Figure 3.8Ai, with each end point representing a single interneuron and the branch connections indicating linkages between interneurons. This created various levels ("hierarchies") into which the population could be grouped. Any separation would be based on the minimum required linkage between interneurons for these interneurons to be grouped into the same cluster. By visual inspection, we tested a range of cutoff distances in order to yield 4 clusters of similar sample sizes to the k-means clusters used in the study. We therefore set the cutoff at 57% of the maximum distance between any two interneurons in the population. The resulting 8 clusters are colored differently in Figure 3.8Ai. In order to adequately compare these clusters with those of the study, we inspected all possible permutations (8!=40,320) for maximum overlap. This produced the corresponding k-means cluster labels for the hierarchical clusters shown in Figure 3.8Ai.

The hierarchical clustering analysis had 83% overlap with the k-means clustering analysis, meaning 83% of interneurons were placed in the same cluster in both analyses. This indicates substantial agreement in the results between both methods. The distributions for each clustering analysis is shown in

Figure 3.8 Comparison of different clustering methods
A UPGAM hierarchical clustering using combined anatomical and electrophysiological data yielded similar results to k-means clustering. **i** UPGAM hierarchical dendrogram separates the 122 interneurons sequentially by the least squared Euclidean distance. Each branching point represents the splitting of a cluster into two clusters, until the clusters are comprised of single neurons. Each end point thus represents a single interneuron. Branch points above the height of 2.8 (a.u.), in this case representing 57% of the maximum distance in the population, are considered to represent distinct clusters. These resulted in 8 different clusters, half of which had 3 or fewer interneurons. In order to match up these clusters with those derived from the k-means clustering analysis, all possible permutations were tested. The permutation with maximum overlap, shown per the labels for each cluster, was used for further analysis. **ii** The clustering distribution for hierarchical clustering is shown on the left bar, with each color corresponding to the branch on the dendrogram. The 4 clusters with less than 4 interneurons were grouped into the gray "Other" category. The clustering distribution for the k-means clustering is shown on the right, in the same color scheme used throughout the rest of the chapter. For each distribution, red whiskers represent the PV+ interneurons. Black lines connect corresponding interneurons that were categorized differently in each distribution, therefore fewer lines indicate greater overlap between clustering methods. The 2 clustering methods showed 85% overlap, meaning 85% of interneurons were categorized within the same cluster. The number of interneurons in each cluster is noted beside each cluster, along with the percentage of that cluster which was classified into their corresponding cluster in the other clustering method. For example, Cluster 1 in the hierarchical clustering method has 45 interneurons, 89% of which were also classified into Cluster 1 in the k-means clustering method. **B** K-means clustering was used to cluster all 122 interneurons using only one type of data: either anatomical or electrophysiological. **i** Distribution plots for purely anatomical clustering and purely electrophysiological clustering are shown as in **Aii**. Both anatomical and electrophysiological clustering were matched to the combined, 4 cluster k-means clustering distribution, as described in the methods. The overlap between purely anatomical and purely electrophysiological clustering was 44%, indicating that some but not most interneurons could be matched to different anatomical and electrophysiological profiles. **ii** The same anatomical and electrophysiological distributions as in **Bi** are shown in comparison with the combined distribution in the center. There is a 70% overlap between the combined distribution and the anatomical; whereas there is 61% overlap between the combined and electrophysiological distribution.

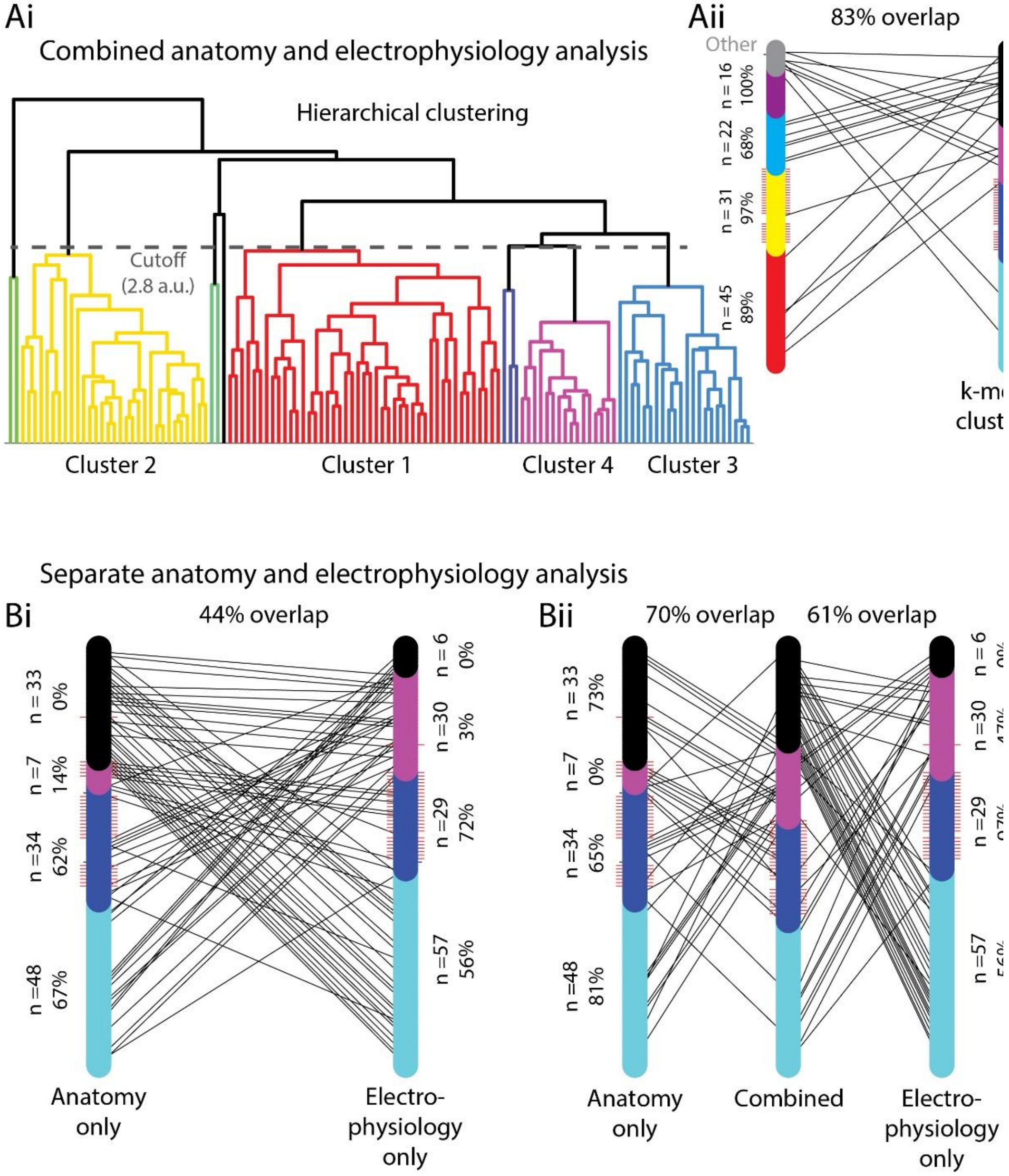
Ai
Combined anatomy and electrophysiology analysis
Hierarchical clustering
Cutoff
(2.8 a.u.)
Cluster 2
Cluster 1
Cluster 4
Cluster 3
Aii
83% overlap
Other
n = 16
100%
n = 22
68%
n = 31
97%
n = 45
89%
k-m
clust
Separate anatomy and electrophysiology analysis
Bi
44% overlap
n = 33
0%
n =7
14%
n =34
62%
n =48
67%
n = 6
0%
n =30
3%
n =29
72%
n =57
56%
Anatomy only
Electro-physiology only
Bii
70% overlap
61% overlap
n = 33
73%
n =7
0%
n =34
65%
n =48
81%
n = 6
n =30
n =29
n =57
Anatomy only
Combined
Electro-physiology only

Figure 3.8Aii. Cluster 1 had 45 interneurons in hierarchical clustering, 89% of which were categorized into the k-means Cluster 1; in turn, there were 42 interneurons in k-means Cluster 1, 95% of which were classified into hierarchical Cluster 1. The interneurons that were not classified into the same cluster are displayed as black lines leading to the corresponding cluster in Figure 3.8Aii. Both Cluster 2 populations contained all PV+ cells, as shown by the red whiskers indicating PV+ cells in Figure 3.8Aii. Hierarchical Cluster 2 had 31 interneurons, 97% classified into k-means Cluster 2; in turn, k-means Cluster 2 had 30 interneurons, all of which were classified into hierarchical Cluster 2. This shows a high degree of agreement in the predominantly PV+ Cluster 2. Cluster 3 in both analysis had 22 interneurons, although the overlap in each direction was only 68%. Hierarchical Cluster 4 had 16 interneurons, all of which were classified into k-means Cluster 4. This cluster had 28 interneurons and only 57% were classified into hierarchical Cluster 4, completely due to the difference in cluster size.

Combined data clustering versus separate data clustering

We conducted separate analyses using either anatomical or electrophysiological data, using the same principal components analysis and k-means clustering analysis as the study. We matched the resulting 4 clusters from each analysis to the combined, 4-cluster k-means analysis used in the study.

First, we compared the clustering results for the anatomy-only and electrophysiology-only data sets, shown in Figure 3.1Bi. These distributions showed only 44% overlap, suggesting that there is limited predictability for anatomy given electrophysiology, and vice versa. Sixty-seven percent of anatomical Cluster 1 cells (n = 48) matched up with electrophysiological Cluster 1 (n = 57), which in turn had 56% of its cells matched. Similarly, 62% of anatomical Cluster 2 cells (n = 34) matched with electrophysiological Cluster 2 (n = 29), of which 72% matched. Electrophysiological Cluster 2 had all but one of all the PV+ cells, which indicates that these cells could be well clustered using only electrophysiological data. Anatomical Cluster 2, however, had a smaller fraction of PV+ cells (20 out of 26, 77%), suggesting that anatomical data were not as clear cut a differentiator for PV+ cells. Anatomical Cluster 3 was small, with only 4 cells, only 14% of which matched with electrophysiological Cluster 3. This cluster had 29 cells, only 3% of which matched with anatomical Cluster 3. Overall Cluster 3 showed almost no correlation between its anatomy and its electrophysiology. Similarly, Cluster 4 showed no correct matches between the anatomical distribution (n = 33) and the electrophysiological (n = 6). This suggests that Clusters 3 and 4 had a less distinct paired anatomical and electrophysiological profile than Cluster 2.

We then inspected the similarity of each separate analysis to the combined distribution used in the study, as shown in Figure 3.8Bii. The anatomical distribution had 70% overlap with the combined distribution, whereas the electrophysiological cluster had 61% overlap with combined distribution. Anatomical clusters were matched with their corresponding combined clusters in proportions of 81%, 65%, 0%, and 73%, respectively. Electrophysiological clusters were matched with their corresponding combined clusters in proportions of 56%, 97%, 47%, and 0%, respectively. Notably, combined Cluster 4 had a large portion of its population assigned to electrophysiological Cluster 1 (68%).

Discussion

Hierarchical clustering showed substantial similarity with k-means clustering, with an overlap of 83% between both analyses. This lends support to the clustering method used in the study, as similar results could be obtained using a different method. It is important to note that the hierarchical clustering method produces 8 clusters, as opposed to 4, which meant that 8 of the 122 interneurons were not matched to corresponding k-means clusters. This set a ceiling of 93% on the possible overlap between the two distributions. Furthermore, for simplicity the k-means distribution used in this analysis included the 19 interneurons discarded in the main study for poor clustering. This may further explain the population of interneurons that were not matched in the two analyses.

Anatomical and electrophysiological clustering comparisons suggest there is only limited (44%) overlap between the separate anatomical and electrophysiological profiles of the interneuron population. Cluster 1 was in both distributions the largest cluster and showed higher than average amount of overlap. Cluster 2, as the cluster containing many PV+ cells, also showed higher overlap than average. Clusters 3 and 4, however, showed close to no overlap in their distributions. The greater disparity in cluster size in both the anatomical and electrophysiological distributions suggest that these data sets do not conform particularly to the division into 4 clusters, but rather may be better fit to 3 clusters. This result itself suggests that while combining the two data types yields 4 distinct profiles of interneurons, anatomy or electrophysiology alone would not predict the same number of clusters. Electrophysiological clustering grouped all but one PV+ cell into the same cluster, however, anatomical clustering had 6 PV+ cells assigned to other clusters. Electrophysiology, thus, may be a slightly more reliable predictor of PV expression than anatomy.

When comparing the separated analyses to the combined analysis distribution, we observed that the anatomical distribution had a 70% overlap with the combined distribution, whereas the electrophysiological distribution had 61% overlap. Some of the combined clusters corresponded to the separated clusters more poorly than others. For instance, anatomical Cluster 4 had 68% of its cells classified into electrophysiological Cluster 1. According to the results of the study, this indicates that the layer 1 projecting cells of Cluster 1 may have similar electrophysiological profiles to those of the main study's Cluster 1, but were differentiated mainly by the more superficial soma depth and axonal projections. This further validates our use of combined anatomical/electrophysiological clustering analysis in the main study.

CHAPTER 4

INHIBITION-MEDIATED GAMMA OSCILLATIONS IN THE MEC

Introduction

Gamma frequency (30-100Hz) oscillations in the MEC and other cortical structures are thought to coordinate interactions between local neurons and their efferent targets in the hippocampus (Chrobak and Buzsáki, 1998; Cunningham, 2004; Quilichini et al., 2010). Specifically, it is thought that cortical principal neurons that are phase-locked to gamma oscillations are more effective at exciting downstream hippocampal neurons relative to non-gamma phase locked neurons. Although robust MEC gamma oscillations have been observed in rodents and human, the mechanism by which these gamma oscillations can be so robustly maintained *in vivo* are not fully understood (Buzsáki and Wang, 2012; Wang, 2010). In a circuit with high inhibitory interconnectivity and heterogeneous inputs like the MEC (Beed et al., 2010; Couey et al., 2013; Pastoll et al., 2013; Woodhall et al., 2005), fluctuation-driven stochastic inhibition-mediated networks are an attractive model for gamma generation. Recent work by Tikidji-Hamburyan and Canavier (2013) suggests that I-I networks with resonant (as opposed to integrating) interneurons produce a more robust model for I-I gamma generation, a finding also supported by Baroni et al. (2014) and

Moca et al. (2014).

The model proposed by Tikidji-Hamburyan and Canavier describes interneurons as resonators, capable of responding to synaptic inputs with ringing, as in Figure 4.1Ai. This property implies that interneurons can exhibit post-inhibitory rebound (PIR) firing, i.e., a strong enough inhibitory synaptic impulse near threshold can produce a large enough depolarization (after the initial hyperpolarization) to cross the neuron's firing threshold and initiate an action potential (Figure 4.1Aii). The model further predicts that an interneuron synaptically coupled to itself via an inhibitory autapse (as in Figure 4.1B; this is a highly reduced model representing an interconnected population of interneurons) can self-sustain continuous fire. In a randomly connected network with no noisy inputs, these properties would result in a single, stable network frequency with all cells firing in synchrony (Figure 4.2Ai). An important feature of this model, however, is that the network frequency remains robust when noise is introduced into the inputs. In the noisy input regime, single cells begin to skip cycles while the network frequency period remains the same, as shown in Figure 4.2Aii-iii. This is evident in Figure 4.2Bi-ii in the difference between the interspike intervals (ISI) of the network, which remains constant at longer time spans, and the interspike intervals of single neurons, which become reduced in count across longer time spans. Figure 4.2C shows that the probability of a PIR spike occurring at a given neuron is dependent on the number of presynaptic spikes and the synchrony (or its inverse jitter) of those inputs. In short, a minimum number of inputs are necessary, and low jitter greatly facilitates the firing of a PIR

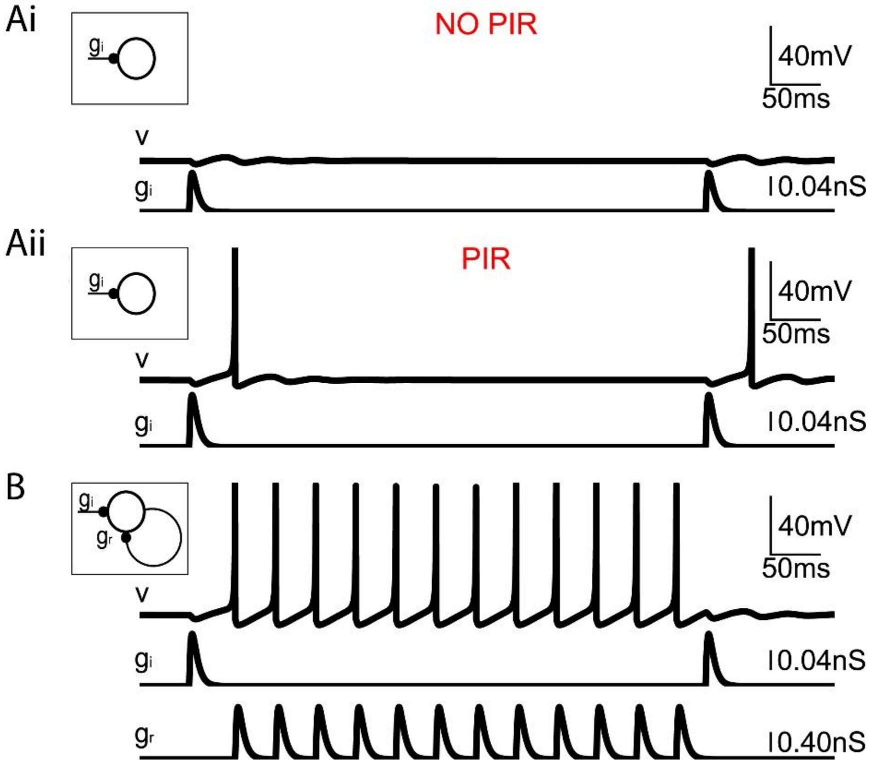

Figure 4.1 Model resonant interneuron characteristics

Ai A model resonant interneuron with an inhibitory input does not elicit a post-inhibitory rebound (PIR) spike if the input is too small. The voltage (V) trace is shown above the input conductance (gi) trace. **ii** A slightly larger input elicits a PIR spike. **B** A model resonant interneuron with both an inhibitory input and autapse can sustain a train of oscillatory firing, emulating behavior within a network. The voltage (V) trace is shown above the synaptic input conductance (gi) and autapse input conductance (gr) traces.

Figure 4.2 Model resonant interneuron network behavior under noisy input
Ai Each point represents the firing of an action potential. In a randomly connected network with no noise, these resonant interneurons would exhibit stable tonic firing with each neuron firing in each cycle. **ii** When noise is added to the resonant interneuron network, the network frequency is maintained, but interneurons exhibit cycle skipping. **iii** Single cell voltage trace within a noisy network regime shows that the neuron skips cycles but its firing remains entrained to the network frequency. **Bi** The network ISI is consistent with peaks at multiples of 40 ms. **ii** However the single neuron ISI is less consistent at greater interspike intervals, due to cycle skipping. **C** The probability of a PIR spike being elicited in any particular neuron is plotted as a function of both input jitter and the number of presynaptic spikes. A PIR spike requires a minimum number of presynaptic neurons to spike and for the jitter among those spikes to be low. **D** When the variance of input current is increased, the IPSP-to-spike latency peak is decreased. Since the IPSP-to-spike latency determines how fast inputs result in spikes, the network period is set by the IPSP-to-spike latency.

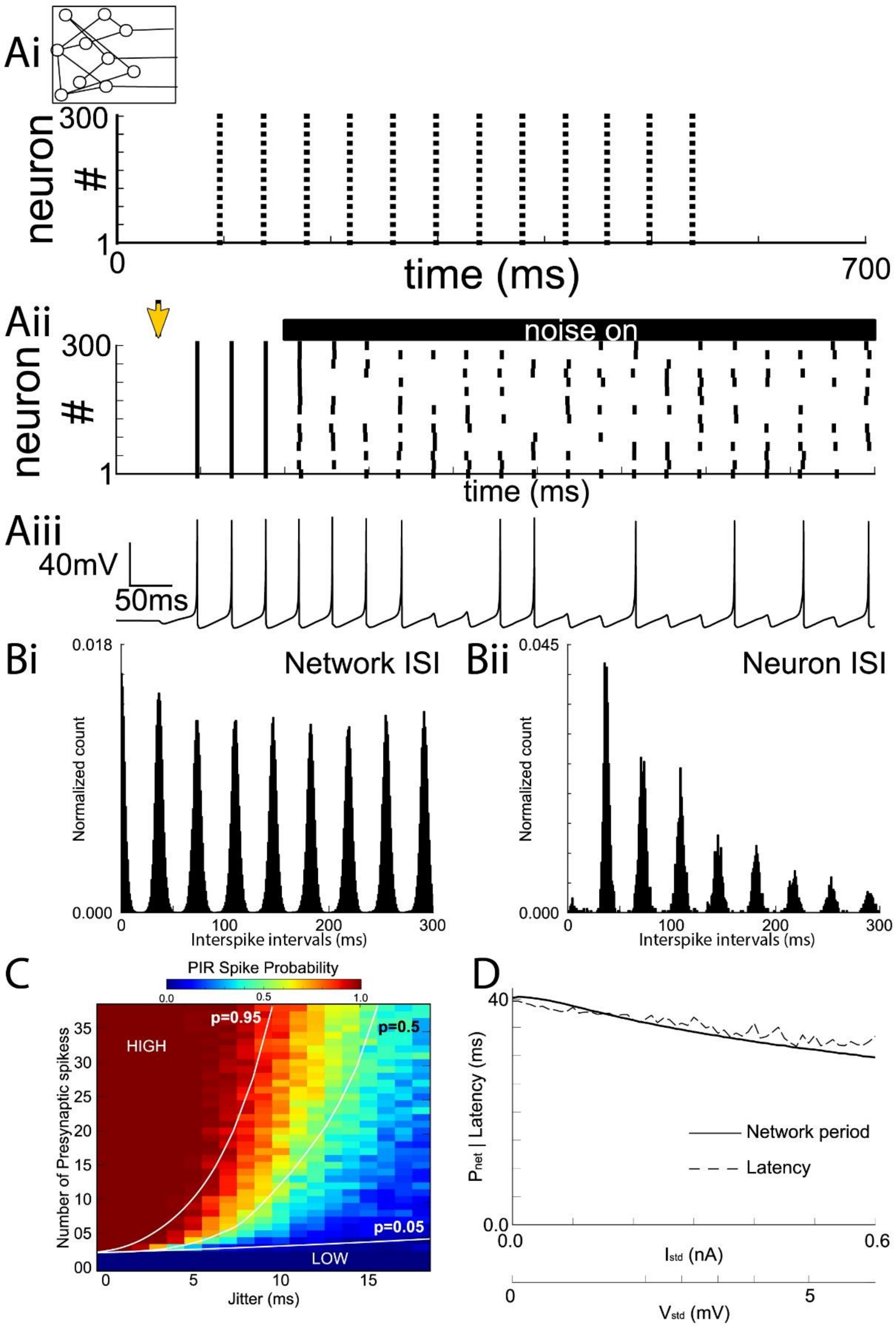
Ai
neuron #
300
1
0
time (ms)
700
Aii
noise on
neuron #
300
1
time (ms)
Aiii
40mV
50ms
Bi
Network ISI
0.018
0.000
Normalized count
0
100
200
300
Interspike intervals (ms)
Bii
Neuron ISI
0.045
0.000
Normalized count
0
100
200
300
Interspike intervals (ms)
C
PIR Spike Probability
0.0
0.5
1.0
p=0.95
p=0.5
p=0.05
HIGH
LOW
Number of Presynaptic spikess
35
30
25
20
15
10
05
00
0
5
10
15
Jitter (ms)
D
40
0.0
P_{net} | Latency (ms)
Network period
Latency
0.0
0.6
I_{std} (nA)
0
5
V_{std} (mV)

spike. Finally, Figure 4.2D shows how the network period is closely matched to the average input-to-spike latency at several variance levels of input current. For the gamma rhythmogenesis network model to produce 30-100 Hz oscillations, interneurons would thus have to exhibit input-to-spike latencies on the order of 10-33 ms.

The network hypothesized by Tikidji-Hamburyan and Canavier relies on postinhibitory rebound (PIR) spiking between interneurons to drive firing and synchronize interneuron ensembles. Network period in these simulations is commensurate with the synaptic input-to-spike latency, and cycle skipping is caused by disruptive inhibitory synaptic inputs that arrive just prior to the action potential initiation. However, there is no evidence that MEC interneurons express the electrophysiological properties—such as PIR spiking at the appropriate input-to-spike delay—necessary to exhibit these behaviors. Furthermore, it is currently not known whether these properties are preferentially expressed in certain interneuron cell types and not others.

Using whole-cell dynamic clamp to elicit inhibitory synaptic inputs (Economo and White, 2012), we tested whether GAD2+ and PV+ interneurons were capable of exhibiting PIR firing in response to inhibitory postsynaptic conductances (IPSGs). In cells for which PIR firing could be elicited, we also simulated network conditions for firing by introducing an artificial autapse that inhibits the cell upon it firing. To determine whether the autapse-induced firing regime responded to “mistimed” inhibitory synaptic inputs, we also injected randomly-timed disruptive IPSGs. We find that parvalbumin positive (PV+)

populations of MEC interneurons are significantly more likely to exhibit PIR-induced firing than the general (GAD2+) interneuron population. This spiking occurs with IPSG-to-spike delay commensurate to maintaining a gamma band oscillation (22±6 ms, corresponding to an average gamma frequency of 45 Hz). We further find that PV+ cells are more likely than the general GAD2+ population to readily maintain autapse-mediated firing. The input phase to phase delay response these cells exhibit to disruptive IPSGs (during the autapse-driven firing regime), however, is linear, as opposed to the exponential relationship predicted by the Tikidji-Hamburyan and Canavier model. We conclude that the expression of these electrophysiological properties in PV+ cells suggest that the gamma rhythmogenesis mechanism proposed by Tikidji-Hamburyan and Canavier is viable in the MEC, although the precise network dynamics these cells exhibit *in vivo* might be different.

Materials and methods

Electrophysiology

All electrophysiology experiments were conducted according to protocols approved by the University of Utah Animal Care and Use Committee. Brain slices were harvested from 18-35 day old transgenic mice. Two transgenic strains were used: cre-dependent GAD2-IRES-tdTomato transgenic mice (Taniguchi et al., 2011, strain 010802, The Jackson Laboratories; Bar Harbor, ME), which labeled glutamic acid decarboxylase 2 gene (GAD2) expressing cells, and thus facilitated targeting of GABAergic cortical interneurons; and PV-tdTomato transgenic mice (Hippenmeyer et al., 2005, strain 008069, The

Jackson Laboratories; Hamden, CT), which labeled all parvalbumin (PV) expressing cells, and thus facilitated targeting of the specific PV+ genotype in inhibitory interneurons. These mice were anesthetized with isoflurane and decapitated. The brain was then harvested, chilled in sucrose-substituted artificial cerebrospinal fluid (ACSF, units in mM, 185 sucrose, 2.5 KCl, 1.25 NaH_2PO_4, 10 $MgCl_2$, 25 $NaHCO_3$, 12.5 glucose, 0.5 $CaCl_2$), and cut parasagittally into 300 µm thick slices using a vibrating microtome (Vibratome VT1200, Leica; Buffalo Grove, IL). Slices were incubated for 15 min in ACSF (units in mM, 125 NaCl, 2.5 KCl, 1.25 NaH_2PO_4, 10 $MgCl_2$, 25 $NaHCO_3$, 25 Glucose, 2 $CaCl_2$) at 37°C, and then allowed to recover for at least 30 min at room temperature. For recordings, slices were transferred to a heated (32-34°C) slice chamber (Warner Instruments; Hamden, CT) that is mounted on an upright microscope stage (Olympus BX53, Olympus; Tokyo, Japan) and perfused with 95/5% O2/C02 ACSF. GAD2+/PV+ neurons were visualized using fluorescence and whole-cell patch clamp clamped using patch pipettes (5-6 MΩ) fabricated from borosilicate glass (1.5 O.D. 1.1 I.D., Sutter Instruments; Novato, CA) and filled with artificial intracellular fluid (ICF, units in mM, 120 K-Gluconate, 5 $MgCl_2$, 0.2 EGTA, 10 HEPES, 20 KCl, 7 di(tris) phosphocreatine, 4 Na_2ATP, 0.3 Tris-GTP) loaded with biocytin (1% by weight) for posthoc reconstruction. Presented data were not corrected for the junction potential, assumed to be 10-12 mV.

Dynamic clamp synaptic stimulation protocol

For all experimental protocols, synaptic conductances were simulated using dynamic clamp software (rtxi.org; Bettencourt et al., 2008; Dorval et al., 2001; Lin et al., 2010) on a Pentium 4 computer running Linux Ubuntu with a patched version of the real-time application interface (RTAI) kernel. Voltage was measured and a control current applied with a MultiClamp 700B amplifier (Axon Instruments, Union City, CA). Conductances were implemented according to $I_{syn}(t)=g_{max}\cdot s(t)(V-E_{syn})$, where gmax is maximal conductance, V is membrane voltage, Esyn is the reversal potential of the synapse (-75 mV for inhibitory, 0 mV for excitatory), and s(t) is the difference of two exponentials with time constants of τrise = 1 ms and τfall = 3 ms. Maximal conductances ranged between 2 and 10 nS. In order to examine a neuron's ability to exhibit postinhibitory rebound firing, single artificial inhibitory postsynaptic conductances (IPSGs) were elicited near threshold with varying maximal conductances. If a neuron was able to exhibit PIR firing in more than 30% of induced IPSGs, then it was determined to be capable of PIR spiking. In neurons exhibiting PIR firing, an artificial inhibitory autapse was introduced wherein the detection of an action potential (determined by a crossing of the -20 mV potential threshold) was followed by an artificial IPSG with a 2 ms delay. Neurons that were able to exhibit PIR firing but not autapse-sustained firing were labeled as such and no further autapse trials were run. In some cells, conductance-based leak was added with a reversal potential of -70 mV and magnitude of 10-20 nS, in order to prevent intrinsic burst firing. To show phase resetting by an additional nonautapse induced IPSG, in some trials an IPSG was inserted randomly 100-300 ms after the initiation of autapse driven firing.

Data analysis

Data analysis was performed using scripts written in MATLAB (The Mathworks, Natick, MA). IPSP-to-spike delays were measured from the initial voltage deflection due to the IPSP to the action potential crossing of the -20 mV threshold. When comparing among groups, reported p values were calculated using a one-way ANOVA with a Tukey test for means when comparing groups assuming equal variance, except when otherwise noted. P values reported for correlation coefficients were calculated with the 'corrcoef' function in MATLAB and represent the probability that a correlation coefficient as large as or larger than the reported value would be obtained by chance. Interspike intervals in autapse trials were calculated as the time between action potential peaks for autapse-driven peaks. A single cycle in all phase analyses was also considered to be action potential peak-to-peak. In trials with disruptive IPSGs, the average cycle period was calculated as the median interspike interval for that trial, and disruptive IPSG introduction phase was calculated with the previous action potential as phase equal to zero. The resulting phase delay was calculated as the total time between the previous spike and the following spike (in the cycle where a disruptive PSG was introduced) divided by the average cycle period. Linear regression fits to the phase/phase delay data were calculated with the least-squares ‘polyfit’ function in MATLAB for a first order polynomial. In trials with a disruptive IPSG, instances where a disruptive IPSG resulted in no further spiking (i.e., the autapse-driven regime was terminated) were labeled failures. The probability of failure was calculated as the proportion of all trials in that phase band which resulted in failure.

Results

Postinhibitory rebound firing

In silico, neurons modeled as resonators exhibit a characteristic “ringing” following a synaptic impulse. This effect can be seen in Figure 4.3Ai. To determine whether physiological interneurons could express this characteristic, whole cell dynamic clamp was used to patch GAD2+ or PV+ cells in acute mouse brain slices. Upon patching these inhibitory interneurons, the membrane was depolarized to the perithreshold region and an inhibitory post-synaptic conductance (IPSG) was injected using dynamic clamp. The resulting hyperpolarization followed by a smaller depolarization and “ringing” can be seen in Figure 4.3Aii.

Under perithreshold conditions, resonant neurons also exhibit post-inhibitory rebound spiking in response to strong enough inhibitory input, as shown in Figure 4.3Bi. The same interneuron shown in Figure 4.3Aii is shown in Figure 4.3Bii receiving a stronger inhibitory synaptic input. The voltage response shows that the stronger inhibitory pulse can produce the postinhibitory rebound firing required for the gamma rhythmogenesis model proposed by Tikidji-Hamburyan and Canavier to work. These initial findings were important to establishing that these resonant properties existed in at least some MEC interneurons.

Autapse-driven firing

Having established that some MEC interneurons can exhibit postinhibitory rebound firing, it was important to establish whether these interneurons could

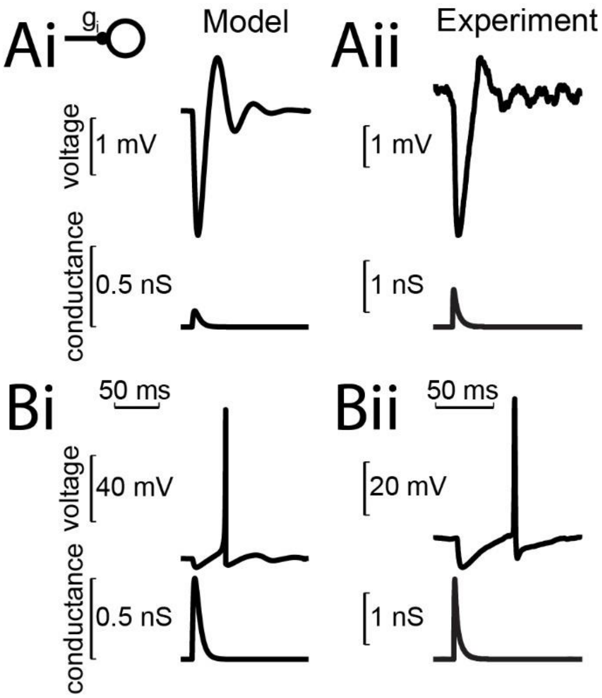

Figure 4.3 Model cell and physiological cell single input comparison
Ai In the model, a weak inhibitory input fails to elicit a PIR spike but is instead followed by resonant ringing. **ii** Similarly, in a whole cell patch clamped GAD2+ inhibitory interneuron, a weak inhibitory input is followed by resonant ringing. **Bi** In the model, a strong inhibitory input results in a PIR spike. **ii** This PIR spiking is also replicated in a GAD2+ inhibitory interneuron.

replicate the in-network dynamics of the model. As an alternative to attempting to simulate an entire network of cells in the dynamic clamp environment, an inhibitory autapse was used as a proxy for network inputs onto the interneuron. Two milliseconds after each action potential, the interneuron would receive an inhibitory synaptic conductance, simulating the type of firing it would receive within a mutually inhibitory network. In this manner, model neurons (Figure 4.4Ai) and actual interneurons (Figure 4.4Aii) could enter an autapse-sustained continuous firing regime. The interspike intervals for each autapse trial is shown in Figure 4.4Bi-ii. Whereas the peak for the model cell centered and peaked at approximately 38 ms, the patched interneuron ISI is centered around 26 ms.

Differences in PIR spiking and autapse-driven firing expression between GAD2 cells and PV cells

In this study, both GAD2+ and PV+ interneurons were examined for expression of PIR firing and autapse-maintained firing. Not all interneurons that were able to fire in response to postinhibitory rebound firing were capable of maintaining autapse-driven firing. All in all, 95 cells were examined for these properties: 25 PV+ cells and 70 GAD2+ cells. The proportion of GAD2+ cells that exhibited either of the inspected properties was low. Only 23 cells out of 70 (33%) were able to fire in response to an inhibitory input and only 6 of those (9% of the total) were able to maintain autapse-driven firing (it is important to note here that GAD2+ cells include PV+ cells within its population). In general, however, a majority of PV+ cells readily exhibited PIR firing and were able to maintain autapse-induced firing. Of the 25 PV+ cells examined, 18 (72%) could fire in response to an inhibitory synaptic conductance. Of those, 14 (56%

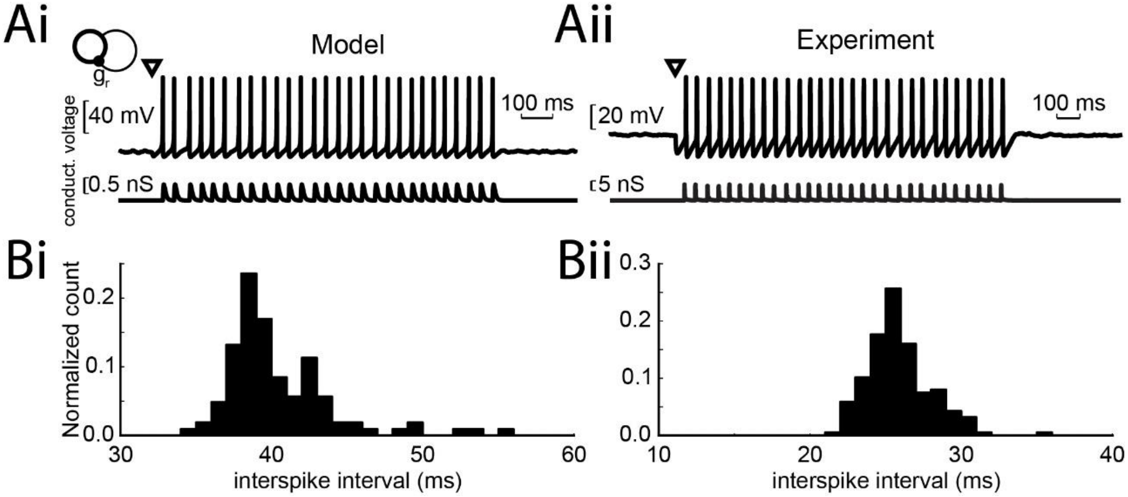

Figure 4.4 Model and physiological autapse input comparison
Ai In the model, an inhibitory autapse elicits sustained firing. The voltage trace is located above the autapse input conductance trace. **ii** In a GAD2+ inhibitory interneuron, a simulated inhibitory autapse (introduced using dynamic clamp) also elicits sustained firing. **Bi** The model neuron exhibits an interspike interval distribution with a peak at 38 ms. **ii** The GAD2+ inhibitory interneuron interspike interval distribution for this cell has a peak at 25 ms.

of the total) could also maintain autapse-induced firing (see Table 4.1). The input-to-spike delay (which the model predicts should be between 10-33 ms long to account for a 30-100 Hz gamma rhythm) for these groups were different. GAD2+ interneurons had IPSG-to-spike latencies 46±16 ms (n = 17) in cells that could not exhibit autapse-induced firing and 44±16 ms (n = 6) for those that could (n.s.). PV+ neurons, in turn, had far shorter latencies. PV+ cells that could not maintain autapse-driven firing had average IPSG-to-spike delays of 31±8 ms (n = 4). PV+ cells that could also engage in an autapse-driven firing had significantly shorter ($p < 0.05$) IPSG to spike delay than those that could not 22±6 ms (n = 14). This disparity could suggest that in PV+ cells shorter delays are important for enabling autapse-driven continuous firing.

Disruptive IPSG injection in the autapse-driven firing regime

A key aspect of the model proposed by Tikidji-Hamburyan and Canavier is how the timing of inputs in the network affect population synchrony: inhibitory inputs can delay the firing of an action potential in a single cell (see Figure 4.5Ai), which will in turn affect that interneuron’s output to other interneurons. Specifically, the network predicts that while inputs arriving in the first half of the spike-to-spike cycle (the normalized phase band between 0 and 0.5), inputs arriving in the second half of the cycle can substantially delay the next spike or even terminate the next action potential entirely (this effect is labeled “oscillator death”). This relationship between the timing of the IPSG and the resulting delay to the next spike is illustrated in Figure 4.5Bi.

Table 4.1 Cell counts for each PIR response phenotype

Cell counts per cell type	No PIPSR	PIPSR+ but cannot maintain autapse firing	PIPSR+ and can maintain autapse firing
PV+	7	4	14
GAD2+ only	47	17	6

The cell counts for all possible postinhibitory rebound responses examined are shown for both PV+ and GAD2+ cells. The first column shows the total number of cells in each cell type that failed to show postinhibitory synapse rebound (PIPSR) firing. The second column shows the counts for cells that expressed PIPSR firing but could not successfully maintain autapse-driven firing. The third column shows the counts for cells that both expressed PIPSR firing and could robustly maintain autapse-driven firing.

Figure 4.5 Effect of a disruptive IPSG during the autapse-sustained firing regime
Ai In the model, injecting a random, disruptive IPSG to the autapse-sustained firing regime can delay the next spike. The voltage trace is located above the autapse input conductance trace and also the disruptive inhibitory conductance. **ii** Similarly, injecting a disruptive IPSG to a GAD2+ inhibitory interneuron can delay the next spike. **Bi** The model predicts that the resulting delay that the disruptive IPSG will elicit, depending on the phase of the spike-to-spike cycle at which it arrives. IPSGs arriving in the first half of the phase are predicted to not delay the next spike, however, past the half phase point the resulting delay increases dramatically until it reaches an "oscillator death" zone, upon which a disruptive IPSG is likely to terminate the autapse-sustained firing. Following the "oscillator death" zone, the phase delay elicited by the IPSG approaches zero. **ii** In a GAD2+ inhibitory interneuron, interneurons in an induced autapse-sustained firing regime were injected with a random, disruptive IPSG. The phase at which these IPSGs were injected are plotted against the resulting phase delay, with each point representing a single trial. The red line shows the average membrane potential for a single cycle, showing the first hyperpolarization following the previous action potential, a steady rise to the next action potential throughout the cycle and ending with the steep depolarization of the next action potential. The blue line represents the linear regression fit to the data, which has a slope of 1.32. Unlike the model, the resulting delay of disruptive IPSGs in the physiological interneuron is best represented by a straight line. **C** The probability of a disruptive IPSG terminating the autapse-sustained firing regime is dependent on the phase at which the IPSG is injected. In PV+ cells, the phase band between 0.8 and 0.9 has the highest probability of failure (0.4) of any other phase band, replicating the prediction of the model. **D** PV+ cells that successfully exhibited autapse-sustained firing had a significantly lower (22±6 ms) IPSP-to-spike delay than PV+ which failed to exhibit autapse-sustained firing (31±8 ms). There was no significant difference in the IPSP-to-spike delay between successful and failed autapse GAD2+ cells.

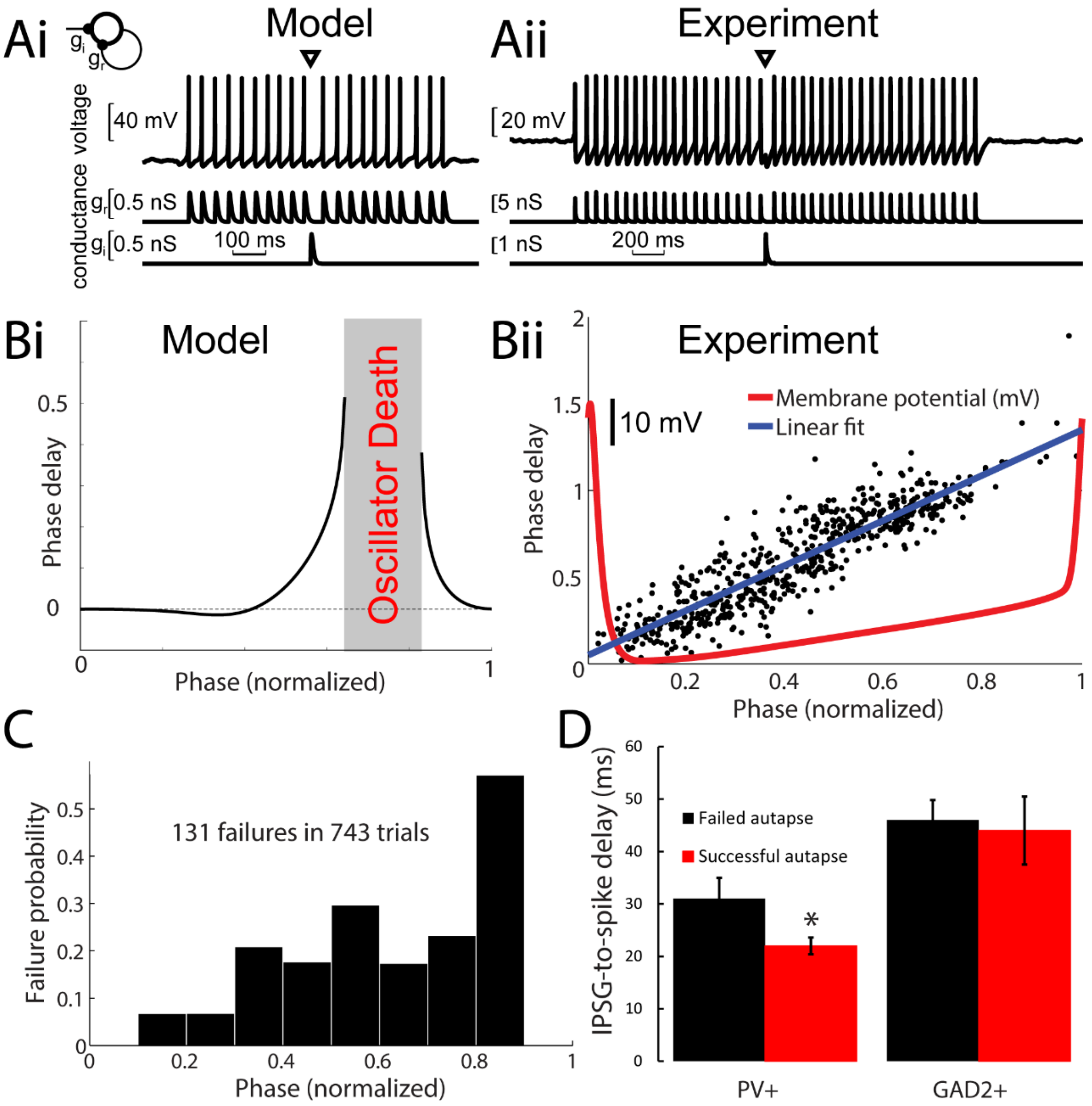
Ai
g_i
g_r
Model
voltage
40 mV
conductance
g_r 0.5 nS
g_i 0.5 nS
100 ms
Aii
Experiment
20 mV
5 nS
1 nS
200 ms
Bi
Model
Oscillator Death
Phase delay
0.5
0
0
1
Phase (normalized)
Bii
Experiment
Phase delay
2
1.5
1
0.5
0
10 mV
Membrane potential (mV)
Linear fit
0.2
0.4
0.6
0.8
1
Phase (normalized)
C
131 failures in 743 trials
Failure probability
0.5
0.4
0.3
0.2
0.1
0
0
0.2
0.4
0.6
0.8
1
Phase (normalized)
D
IPSG-to-spike delay (ms)
60
50
40
30
20
10
0
Failed autapse
Successful autapse
*
PV+
GAD2+

In order to replicate these conditions in the dynamic clamp environment, PV+ cells in the autapse-driven firing regime were injected with an additional IPSG at a random time point, as shown in Figure 4.5Aii. The phase timing of this random input was determined within the spike-to-spike cycle that the input was injected, and the resulting delay to the next spike was calculated as described in Materials and Methods. The results from 612 successful disrupted autapse trials in 10 PV+ cells are shown in Figure 4.5Bii. The relationship is best fitted with a line with slope 1.32 and intercept of 0.05 (in blue); the coefficient of determination is 0.847. (The average membrane potential for a single spike-to-spike cycle is shown in red in Figure 4.5Bii.) The phase-phase delay effect of IPSGs is linear, and thus different than that predicted from the model, which implies that the mechanism by which inhibitory interneurons might synchronize in gamma within a network is not well-explained by the proposed model.

The “oscillator death” zone in the model predicts the phase space (approximately 0.6 to 0.8) where the disruptive IPSG would most likely prevent the next action potential from happening. In the simulated autapse environment, this would lead to a complete termination of the autapse-driven firing regime. Disruptive IPSGs that were not followed by an action potential were labeled “failure” autapse trials. These trials comprised 131 of the total 743 trials (17.6%) conducted in 10 PV+ cells. Figure 4.5C shows the probability of these failures occurring depending on the phase at which the disruptive IPSG arrived. While failures occurred throughout the phase space between 0.1 and 0.9, the peak failure probability is in the phase space between 0.8 and 0.9, which is similar to that predicted by the model.

Discussion

We have demonstrated that PV+ MEC interneurons are more likely than the GAD2+ population to exhibit the resonant behaviors necessary for viability of the proposed gamma rhythmogenesis. The input-to-spike delay in these PV+ interneurons is appropriate for such a network to exhibit gamma oscillations, with 22±6 ms delays predicting network frequencies between 40-50 Hz. The results have also demonstrated that PV+ interneurons are more likely to enter an autapse-mediated firing regime in response to an inhibitory autapse, a network analogue that suggests the cells would behave similarly in a network of similarly resonant cells. The input phase to phase delay response of these cells, however, are different to those exhibited in the model, being best described by a linear fit of slope 1.32 rather than an exponential fit shown in the model.

Our findings agree with previous work suggesting that the PV+ interneuronal population can exhibit resonant behaviors. Mancilla et al. (2007) showed that fast-firing interneurons in the rat barrel cortex were more likely to exhibit type 2 discontinuous frequency-current relationships, whereby neurons are unable to fire at arbitrarily low frequencies. This frequency-current relationship is associated with resonant firing behavior (Izhikevich, 2007). Tateno (2004) described fast-firing interneurons in the rat somatosensory cortex that alternated between a fast firing regime and a nonfiring, subthreshold regime, another feature of resonant behavior. Both these observations were made in several superficial MEC PV+ cells in this study through protocols conducted for the study in Chapter 3 (data not shown).

The ability of PV+ to exhibit the resonant behaviors described here is promising for the viability of the I-I resonator network model proposed by Tikidji-Hamburyan and Canavier (2013). First, previous work has shown PV+ interneurons in the cortex have dense, unspecific interconnectivity with other PV+ neurons (Packer and Yuste, 2011). This connectivity profile is similar to the gamma network model, lending further support to the viability of the model. Second, PV+ cells have already been implicated in gamma rhythmogenesis, both *in vitro* (Gulyas et al., 2010) and in *vivo* (Cardin et al., 2009). Cardin et al. (2009) showed that optogenetically driving PV+ interneurons can induce gamma oscillations in barrel cortex of anesthetized mice. Both these results support our finding suggesting PV+ neurons are more likely to participate in the proposed gamma rhythmogenesis model.

In MEC PV+ cells that were able to enter the autapse-induced firing regime, the measured input-to-spike delay (22±6 ms) was generally in agreement with the electrophysiological features required for the gamma rhythmogenesis model. The input phase to phase delay relationship, however, was notably different than the one predicted by the model. The model predicts the phase delay to be relatively unaffected if the input arrives in the first half of the cycle, whereas inputs arriving in the second half of the cycle are predicted to quickly increase the resulting delay to the next spike (Figure 4.5Bi). The relationship measured in PV+ cells, however, was best described by a straight linear relationship. This difference may be due to the simplified resonator neuron model used in the network simulation, which lacks the full membrane dynamics present in an actual cell. In particular, the model neuron used in the simulation implements a postaction potential artificial reset to -65 mV to simulate the afterhyperpolarizing potential. Once the model neuron is reset, it is then depolarized from -65 mV back to the perithreshold resonant regime, which results in a region at the beginning of the cycle where hyperpolarizing inputs with a reversal potential of -75 mV could have a diminished impact on the subsequent action potential timing. In the real cell, however, there exists two key differences. First, the beginning of the cycle is set near the peak of the previous action potential, therefore, the first tenth of each cycle generally describes the region including the peak of the action potential, the downstroke of the action potential, and the final minimum spike AHP. The red trace in Figure 4.5Bii describing the average autapse cycle membrane potential illustrates this region in the phase space between 0 and 0.1. Second, the maximum post-spike hyperpolarization for PV+ cells in the autapse-induced firing regime is approximately -55 mV, not -65 mV as in the model. This means the cell's membrane potential is usually more depolarized than in the model cell in the first half of the cycle. Since inhibitory conductance inputs are based on the difference between the membrane potential and the GABA reversal potential (i.e., the driving force), PV+ cells receive inhibitory inputs larger in amplitude than the model cells in the network. This disparity in input size likely explains the significant delaying effect that disruptive IPSGs have in the first half of the cycle. Finally, the oscillation death zone measured in the cells, in turn, was similar to the zone predicted in the model, with both the model and the measured physiology predicting a maximum probability of oscillation death in the phase space between 0.8 and 0.9, as shown in Figure 4.5C.

Although we emphasize the disposition for PV+ neurons to exhibit resonant properties, it is equally important that the GAD2+ interneuron population exhibits low rates of both PIR-induced firing (33%) and autapse-induced firing (9%). In the proposed model, networks are constructed either entirely with resonant or entirely with integrator interneurons: resonant interneuron networks produce gamma oscillations whereas integrator networks do not (Tikidji-Hamburyan and Canavier, 2013). Our findings, however, suggest there is heterogeneity in the expression of resonant properties in the MEC interneuron population. An interesting venue for future work is to investigate the robustness of this gamma rhythmogenesis model in networks with varying fractions of resonant interneurons.

Collaborator contributions

The work in this chapter was completed in collaboration with Ruben Tikidji-Hamburyan and Carmen C. Canavier at Louisiana State University. RTH and CCC conceived of the model that is validated in this chapter. JJMC collected all electrophysiological data presented here, conducted all of the analysis of these data, and wrote the chapter text in its entirety. RTH produced the panels shown in Figures 4.1 and 4.2 and the model-specific panels in Figures 4.3 and 4.4. JJMC produced all other subpanels in the chapter.

CHAPTER 5

CONCLUSION

Major findings

Understanding the role of the medial entorhinal cortex in spatial navigation, learning, memory, and multimodal sensory processing remains an intense focus of research. The discovery of grid cells in the superficial MEC in particular has spurred interest in how this cortical circuit is capable of producing this spatially modulated activity and what purpose this activity has in the larger task of navigation. The work presented in this dissertation, while not addressing behavioral functionality directly, attempts to address the relatively understudied inhibitory dynamics within this brain region. We have identified how an input integration phenomenon may play a role in how inhibitory synaptic inputs impact stellate cell activity, we have classified superficial MEC interneurons into distinct anatomical/electrophysiological clusters, and we have helped validate a gamma rhythmogenesis mechanism in the superficial MEC. These major findings are summarized in Chapter 5.1. In Chapter 5.2 we look at the future directions for research that may prove fruitful to fully understanding the superficial MEC circuit.

In our first study, we found that entorhinal stellates integrated synaptic inputs in a nonlinear manner, amplifying inputs arriving at more depolarized membrane potentials. We chose to explore this phenomenon because stellate neurons in the superficial MEC exhibit ~10 mV membrane potential oscillations during *in vivo* movement, coinciding with population-level local field potential theta (4-12 Hz) rhythms (Domnisoru et al., 2013; Quilichini et al., 2010; Schmidt-Hieber and Häusser, 2013). *In vitro,* stellate cells also have a pronounced theta band resonant peak in their impedance spectra (Burton et al., 2008; Erchova et al., 2004; Fernandez and White, 2008; Garden et al., 2008; Haas et al., 2007; Nolan et al., 2007), which indicates that synaptic inputs are preferentially amplified near the peaks of their membrane potential oscillations. This membrane potential-dependent increase in subthreshold impedance is produced by the persistent sodium channels expressed in stellate cells. We confirmed these prior findings by showing that the subthreshold impedance of stellate cells is sensitive to the membrane potential and that this increase can be eliminated with the introduction of sodium channel blocker tetrodotoxin. This result implicates the persistent sodium conductance in generating this increase in impedance. In order to study the effect of this impedance increase on synaptic integration, we used dynamic clamp to inject artificial synaptic conductances into the cell at the perithreshold region. We found that the resulting postsynaptic potential amplitudes were dependent on the membrane potential at which they were elicited: PSPs injected at more depolarized potentials were larger than those elicited at more hyperpolarized potentials. This result was true of both excitatory and inhibitory inputs, and amounted to approximately a 4-5% increase in PSP amplitude per millivolt of depolarization. Quantitatively, this indicates that PSP amplitudes may be modulated by as much as 30-60% *in vivo*, given that stellate cells undergo ~10 mV synaptically-driven oscillations during movement. This voltage dependence, however, is eliminated upon the blockage of Na^+ channels and can be attenuated by blocking the underlying hyperpolarization activated cation current. The result holds if, instead of looking directly at membrane potential, the PSP amplitudes are compared across different oscillation phases: inputs arriving at the peak of the oscillation are significantly greater than those arriving at the trough of the oscillation. Given that stellate cells receive spatially-modulated inputs *in vivo* (Schmidt-Hieber and Häusser, 2013), these results indicate that both excitatory and particularly inhibitory inputs may be amplified/modulated depending on the location of the animal.

In another study, we characterized and classified the interneuron population of the superficial MEC, a relatively understudied component of the medial entorhinal circuit. Recent studies have suggested that GABAergic interneurons in the superficial MEC play an important role in the region's spatial navigation functions (Buetfering et al., 2014; Couey et al., 2013; Domnisoru et al., 2013; Garden et al., 2008; Pastoll et al., 2013; Varga et al., 2010). Among other results, these studies found stellate-to-stellate cell connectivity is mediated by inhibitory interneurons (Couey et al., 2013), spontaneous inhibitory currents were much more frequent in the superficial layers than in the deeper MEC layers (Woodhall et al., 2005), and that PV+ interneurons received inputs from various grid cells that result in a broadly tuned spatial firing profile (Buetfering et al., 2014). Despite the increasing appreciation for the role of GABAergic interneurons, there remained a paucity of data on the combined anatomical and electrophysiological profiles of the superficial MEC's interneurons. This was due to interneurons' representing a minority of the neuronal population (~10%) (Gatome et al., 2010) and the population being incredibly diverse (Ascoli et al., 2008; Buzsáki et al., 2004; Maccaferri and Lacaille, 2003; McBain and Fisahn, 2001; Whittington and Traub, 2003). This study used transgenic techniques to greatly facilitate the targeting of GAD2+ and PV+ for whole cell patch clamp recordings. We used this technique to systematically patch and fill GABAergic interneurons in the superficial MEC, collecting electrophysiological and anatomical data to compile a neuronal profile. Multidimensional clustering analysis was then used to classify the profiled interneurons into distinct groups. We successfully characterized and classified 105 interneurons into four groups. Thirty neurons were classified as layer 2/3-projecting slow firing interneurons, which share features with previously anatomically identified pyramidal-looking interneurons (Kumar and Buckmaster, 2006), multipolar cells (Gloveli et al., 1997), and bipolar cells (Wouterlood et al., 2000). Thirty other neurons were classified as fast spiking, layer 2/3-projecting fast-firing interneurons, the vast majority of which were PV+ and shared characteristic profiles of MEC basket cells (Jones and Bühl, 1993). Fifteen neurons were identified as layer 1/2-projecting interneurons, similar to the multiform neurons described in Tahvildari and Alonso (2005). Finally, 28 interneurons were classified as layer 1-projecting interneurons, similar to the multipolar (Wouterlood et al., 2000) and horizontal cells (Germroth et al., 1989) previously described. This classification scheme can serve as the foundation for future studies into inhibitory dynamics in the superficial MEC. Already, work has shown that PV+ interneurons (as in the second cluster) are important to grid cell formation and gamma oscillations despite their nonspatially tuned firing fields (Buetfering et al., 2014; Couey et al., 2013; Pastoll et al., 2013). The deeper, slow-firing interneurons of the first cluster, in turn, are likely to play a more nuanced role in the associative networks within MEC layer 3. Their projections exclusively onto layer suggest that interneurons of the fourth cluster may play modulate multimodal inputs onto the MEC.

In a concurrent study, we provided some physiological validation for a gamma rhythmogenesis model proposed by Tikidji-Hamburyan and Canavier (2013), showing that PV+ interneurons in the MEC can exhibit resonant firing properties. This is of substantial importance in the MEC as gamma oscillations are believed to coordinate communication between the MEC and the hippocampus (Schomburg et al., 2014), a mechanism which would require some uniformity in gamma network frequencies in response to noisy inputs. The Tikidji-Hamburyan and Canavier (2013) model produces such a network in a sparsely connected I-I network of type 2 resonator interneurons (Izhikevich, 2003). This model relies on interneurons inhibiting one another, eliciting a postinhibitory rebound (PIR) spike, and overall producing a synchronized network. The network frequency is determined by the input-to-spike delay and is robust to heterogeneity in input. Our study attempted to establish whether the superficial MEC interneurons were capable of exhibiting the resonant characteristics necessary for this model to work, and whether these features were expressed differently in different neuronal subtypes. Using whole cell dynamic clamp to simulate inhibitory synaptic inputs, we examined GAD2+ and PV+ superficial MEC interneurons for their ability to exhibit PIR firing and maintain autapse-induced firing—an attempt to emulate “within the network” input conditions. We found that PV+ cells were much more likely than GAD2+ cells to exhibit both these resonant behaviors. PV+ cells exhibited an average input-to-spike delay of 22±6 ms (for those that could also maintain autapse-induced firing), which predicts that within network these neurons would maintain firing at approximately 45 Hz. GAD2+ interneurons had on average 46±16 ms input delays, too slow to elicit gamma rhythm firing in this model. In the PV+ cell autapse-sustained firing regime, we also found that introducing a disruptive IPSG will delay the firing of the next action potential linearly, contrary to the predicted phase-input-to-phase-delay relationship in the model. Specifically, whereas the PV+ cells had a straight linear relationship with slope 1.32, the model predicts that inputs arriving in the first half of the cycle will not delay the next action potential. Furthermore, inputs arriving further into the second half of the cycle were expected to exponentially increase the delay, with a significant oscillator death zone in the 0.8 to 0.9 phase band. While the oscillator death zone was observed in PV+ cells (inputs arriving in the 0.8 to 0.9 phase band had a ~40% probability of failure), the PV+ cells continued to have a continuous linear relationship between input phase and phase delay. Our findings in this study suggest that the PV+ interneurons in the superficial MEC are capable of exhibiting the resonant behaviors necessary for the Tikidji-Hamburyan and

Canavier (2013) model to work, however exact network dynamics that exist *in vivo* are likely to be different than the model predicts.

This collection of results overall offers insight into several inhibitory mechanisms of the superficial medial entorhinal cortex. First, we understand how inhibitory inputs onto stellate cell somata are preferentially amplified if they arrive at the peak of the stellate cell's theta-modulated and/or spatially-modulated excitatory inputs. Second, we have established that PV+ MEC interneurons exhibit resonant properties that suggest they could participate in a PIR-driven gamma rhythmogenesis mechanism. Finally, we have characterized and classified the interneuron population in the superficial MEC, grouping them according to the depth of the somas, the extent of their axonal projections, and their electrophysiological characteristics.

Future directions

We remain far from completely understanding the inhibitory dynamics of the superficial medial entorhinal cortex. Both the diverse mechanisms that doubtlessly modulate local circuit activity and their role in the larger functions of spatial navigation, learning, memory, and sensory integration will continue to be areas of intense research. The work here nevertheless first offers insight into some of the mechanisms that inhibitory interneurons take part in within the MEC circuit, and second, provides a characterization and classification framework for which to direct future research. The implications of our first study leads directly to future computational work to understand the possible consequences of nonlinear synaptic integration in MEC stellate cells. At this stage, simulations would be the ideal venue to understand how this 4-5% increase in PSP amplitude per millivolt of depolarization can impact the processing of sensory inputs, the maintenance of theta rhythms, and the spatially-modulated activity in the superficial MEC. This effect may prove valuable in the recent drive toward modeling and understanding grid cell-generating mechanisms in this brain region.

The physiological validation of a gamma rhythmogenesis model in our third study suggests that the originally proposed model needs to be reevaluated, based on the difference in the input-phase-to-phase-delay relationship between model and physiological reality. This difference is likely to produce different synchronization regimes within the network, particularly in the face of noisy inputs. Furthermore, our finding that PV+ cells were much more likely than the general GAD2+ population to exhibit resonant properties asks the question whether a similar I-I network with heterogeneous expression of resonant properties is capable of producing the same robust gamma generating network.

Such an endeavor would be aided by the findings of our second study, where we characterized and classified the interneurons of the superficial MEC. Our findings point toward several avenues for future research. For example, the interplay between the slow-firing and fast-firing interneuron populations of layers 2 and 3 is a promising target for understanding the grid cell mechanism. Selective optogenetic manipulation of PV+ and SOM+ populations *in vivo* may help explain how the superficial MEC responds to very heterogeneous inputs and generates grid fields. Anatomical work on the layer 1-projecting cells in this study would explain where this interneuronal population receives inputs (whether mainly from other brain regions or local principal cells) and where its main output targets lie (whether mainly principal cell dendrites or other layer 1 interneurons). Future studies of the inhibitory populations of the superficial MEC could explore different molecular genotypes (such as the PV+, SOM+, and CCK+ populations already mentioned) specifically, as opposed to focusing on the overarching GAD2+ population. This approach is particularly attractive as optogenetic manipulations can harness these molecular markers to target specific subpopulations *in vivo*. Furthermore, spatial variations in interneuronal physiology along the MEC's dorsoventral axis (DVA) could provide vital clues as to the cortical mechanisms behind spatial navigation. Grid field spacing has been shown to increase along the DVA (Hafting et al., 2005). This decrease is matched by a decrease of PV+ inputs and an increase in non-PV+ inputs onto the MEC principal cells (Beed et al., 2010), so there exists an inhibitory gradient along the DVA. Given the known spatial correlates along the DVA, uncovering differences in interneuron physiology (for any of the interneuron populations) between the dorsal end interneurons characterized in this study and the unstudied ventral end interneuronal population would be of particular value to the field. As our understanding of this brain region expands and deepens, the research presented here may provide valuable insight that helps answer fundamental questions about the medial entorhinal cortex's greater role in cortical computation.

REFERENCES

Alonso, A., and García-Austt, E. (1987). Neuronal sources of theta rhythm in the entorhinal cortex of the rat: II. Phase relations between unit discharges and theta field potentials. Exp. Brain Res. *67*, 502–509.

Alonso, A., and Klink, R. (1993). Differential electroresponsiveness of stellate and pyramidal-like cells of medial entorhinal cortex layer II. J. Neurophysiol. *70*, 128–143.

Alonso, A., and Llinás, R.R. (1989). Subthreshold Na+-dependent theta-like rhythmicity in stellate cells of entorhinal cortex layer II. Nature *342*, 175–177.

Ascoli, G.A., Alonso-Nanclares, L., Anderson, S.A., Barrionuevo, G., Benavides-Piccione, R., Burkhalter, A., Buzsáki, G., Cauli, B., Defelipe, J., and Fairén, A. (2008). Petilla terminology: nomenclature of features of GABAergic interneurons of the cerebral cortex. Nat. Rev. Neurosci. *9*, 557–568.

Baroni, F., Burkitt, A.N., and Grayden, D.B. (2014). Interplay of intrinsic and synaptic conductances in the generation of high-frequency oscillations in interneuronal networks with irregular spiking. PLoS Comput. Biol. *10*, e1003574.

Bartolomei, F., Khalil, M., Wendling, F., Sontheimer, A., Régis, J., Ranjeva, J.-P., Guye, M., and Chauvel, P. (2005). Entorhinal cortex involvement in human mesial temporal lobe epilepsy: an electrophysiologic and volumetric study. Epilepsia *46*, 677–687.

Beed, P., Bendels, M.H.K., Wiegand, H.F., Leibold, C., Johenning, F.W., and Schmitz, D. (2010). Analysis of excitatory microcircuitry in the medial entorhinal cortex reveals cell-type-specific differences. Neuron *68*, 1059–1066.

Bettencourt, J.C., Lillis, K.P., Stupin, L.R., and White, J.A. (2008). Effects of imperfect dynamic clamp: computational and experimental results. J. Neurosci. Methods *169*, 282–289.

Bland, B.H., and Oddie, S.D. (2001). Theta band oscillation and synchrony in the hippocampal formation and associated structures: the case for its role in sensorimotor integration. Behav. Brain Res. *127*, 119–136.

Bland, S.K., and Bland, B.H. (1986). Medial septal modulation of hippocampal theta cell discharges. Brain Res. *375*, 102–116.

Boehlen, A., Henneberger, C., Heinemann, U., and Erchova, I. (2013). Contribution of near-threshold currents to intrinsic oscillatory activity in rat medial entorhinal cortex layer II stellate cells. J. Neurophysiol. *109*, 445–463.

Borg-Graham, L.J., Monier, C., and Fregnac, Y. (1998). Visual input evokes transient and strong shunting inhibition in visual cortical neurons. Nature *393*, 369–373.

Brandon, M.P., Bogaard, A.R., Libby, C.P., Connerney, M.A., Gupta, K., and Hasselmo, M.E. (2011). Reduction of theta rhythm dissociates grid cell spatial periodicity from directional tuning. Science *332*, 595–599.

Brunel, N. (2003). What determines the frequency of fast network oscillations with irregular neural discharges? I. Synaptic dynamics and excitation-inhibition balance. J. Neurophysiol. *90*, 415–430.

Buetfering, C., Allen, K., and Monyer, H. (2014). Parvalbumin interneurons provide grid cell–driven recurrent inhibition in the medial entorhinal cortex. Nat. Neurosci. *17*, 710–718.

Burak, Y., and Fiete, I.R. (2009). Accurate path integration in continuous attractor network models of grid cells. PLoS Comput. Biol. *5*, e1000291.

Burton, B.G., Economo, M.N., Lee, G.J., and White, J.A. (2008). Development of theta rhythmicity in entorhinal stellate cells of the juvenile rat. J. Neurophysiol. *100*, 3144–3157.

Burwell, R.D. (2006). The parahippocampal region: corticocortical connectivity. Ann. N. Y. Acad. Sci. *911*, 25–42.

Buzsáki, G. (2002). Theta oscillations in the hippocampus. Neuron *33*, 325–340.

Buzsáki, G. (2006). Rhythms of the Brain (New York: Oxford University Press).

Buzsáki, G., and Wang, X.-J. (2012). Mechanisms of gamma oscillations. Annu. Rev. Neurosci. *35*, 203–225.

Buzsáki, G., Geisler, C., Henze, D.A., and Wang, X.-J. (2004). Interneuron Diversity series: Circuit complexity and axon wiring economy of cortical interneurons. Trends Neurosci. *27*, 186–193.

Canto, C.B., and Witter, M.P. (2012). Cellular properties of principal neurons in the rat entorhinal cortex. II. The medial entorhinal cortex. Hippocampus *22*, 1277–1299.

Canto, C.B., Wouterlood, F.G., and Witter, M.P. (2008). What does the anatomical organization of the entorhinal cortex tell us? Neural Plast. *2008*, 1–18.

Cardin, J.A., Carlén, M., Meletis, K., Knoblich, U., Zhang, F., Deisseroth, K., Tsai, L.-H., and Moore, C.I. (2009). Driving fast-spiking cells induces gamma rhythm and controls sensory responses. Nature *459*, 663–667.

Cauli, B., Porter, J.T., Tsuzuki, K., Lambolez, B., Rossier, J., Quenet, B., and Audinat, E. (2000). Classification of fusiform neocortical interneurons based on unsupervised clustering. Proc. Natl. Acad. Sci. *97*, 6144–6149.

Chrobak, J.J., and Buzsáki, G. (1998). Gamma oscillations in the entorhinal cortex of the freely behaving rat. J. Neurosci. *18*, 388–398.

Couey, J.J., Witoelar, A., Zhang, S.-J., Zheng, K., Ye, J., Dunn, B., Czajkowski, R., Moser, M.-B., Moser, E.I., Roudi, Y., et al. (2013). Recurrent inhibitory circuitry as a mechanism for grid formation. Nat. Neurosci. *16*, 318–324.

Crill, W.E. (1996). Persistent sodium current in mammalian central neurons. Annu. Rev. Physiol. *58*, 349–362.

Csicsvari, J., Jamieson, B., Wise, K.D., and Buzsáki, G. (2003). Mechanisms of gamma oscillations in the hippocampus of the behaving rat. Neuron *37*, 311–322.

Cunningham, M.O. (2004). Coexistence of gamma and high-frequency oscillations in rat medial entorhinal cortex in vitro. J. Physiol. *559*, 347–353.

Cunningham, M.O. (2006). Region-specific reduction in entorhinal gamma oscillations and parvalbumin-immunoreactive neurons in animal models of psychiatric illness. J. Neurosci. *26*, 2767–2776.

Cunningham, M.O., Davies, C.H., Buhl, E.H., Kopell, N., and Whittington, M.A. (2003). Gamma oscillations induced by kainate receptor activation in the entorhinal cortex in vitro. J. Neurosci. Off. J. Soc. Neurosci. *23*, 9761–9769.

DeFelipe, J., López-Cruz, P.L., Benavides-Piccione, R., Bielza, C., Larrañaga, P., Anderson, S., Burkhalter, A., Cauli, B., Fairén, A., Feldmeyer, D., et al. (2013). New insights into the classification and nomenclature of cortical GABAergic interneurons. Nat. Rev. Neurosci. *14*, 202–216.

Dickson, C.., Mena, A.., and Alonso, A. (1997). Electroresponsiveness of medial entorhinal cortex layer III neurons in vitro. Neurosci. *81*, 937–950.

Dickson, C.T., Magistretti, J., Shalinsky, M.H., Fransén, E., Hasselmo, M.E., and Alonso, A. (2000). Properties and role of Ih in the pacing of subthreshold oscillations in entorhinal cortex layer II neurons. J. Neurophysiol.

83, 2562–2579.

Domnisoru, C., Kinkhabwala, A.A., and Tank, D.W. (2013). Membrane potential dynamics of grid cells. Nature *495*, 199–204.

Dorval, A.D. (2005). Channel noise is essential for perithreshold oscillations in entorhinal stellate neurons. J. Neurosci. *25*, 10025–10028.

Dorval, A.D., and White, J.A. (2005). Channel noise is essential for perithreshold oscillations in entorhinal stellate neurons. J. Neurosci. *25*, 10025–10028.

Dorval, A.D., Christini, D.J., and White, J.A. (2001). Real-time linux dynamic clamp: a fast and flexible way to construct virtual ion channels in living cells. Ann. Biomed. Eng. *29*, 897–907.

Dumitriu, D., Cossart, R., Huang, J., and Yuste, R. (2006). Correlation between axonal morphologies and synaptic input kinetics of interneurons from mouse visual cortex. Cereb. Cortex *17*, 81–91.

Economo, M.N., and White, J.A. (2012). Membrane properties and the balance between excitation and inhibition control gamma-frequency oscillations arising from feedback inhibition. PLoS Comput. Biol. *8*, e1002354.

Economo, M.N., Martínez, J.J., and White, J.A. (2014). Membrane potential-dependent integration of synaptic inputs in entorhinal stellate neurons. Hippocampus *24*, 1493–1505.

Engel, J., and Pedley, T.A. (2008). Epilepsy: a comprehensive textbook (Philadelphia: Wolters Kluwer Health/Lippincott Williams & Wilkins).

Erchova, I., Kreck, G., Heinemann, U., and Herz, A.V.M. (2004). Dynamics of rat entorhinal cortex layer II and III cells: characteristics of membrane potential resonance at rest predict oscillation properties near threshold. J Physiol *560*, 89–110.

Fernandez, F.R., and White, J.A. (2008). Artificial synaptic conductances reduce subthreshold oscillations and periodic firing in stellate cells of the entorhinal cortex. J. Neurosci. *28*, 3790–3803.

Fernandez, F.R., Malerba, P., Bressloff, P.C., and White, J.A. (2013). Entorhinal stellate cells show preferred spike phase-locking to theta inputs that is enhanced by correlations in synaptic activity. J. Neurosci. Off. J. Soc. Neurosci. *33*, 6027–6040.

Frank, L.M., Brown, E.N., and Wilson, M.A. (2001). A comparison of the firing properties of putative excitatory and inhibitory neurons from CA1 and the entorhinal cortex. J. Neurophysiol. *86*, 2029–2040.

Freund, T.F., and Antal, M. (1988). GABA-containing neurons in the septum control inhibitory interneurons in the hippocampus. Nature *336*, 170–173.

Freund, T.F., and Buzsáki, G. (1996). Interneurons of the hippocampus. Hippocampus *6*, 347–470.

Garden, D.L.F., Dodson, P.D., O'Donnell, C., White, M.D., and Nolan, M.F. (2008). Tuning of synaptic integration in the medial entorhinal cortex to the organization of grid cell firing fields. Neuron *60*, 875–889.

Gatome, C.W., Slomianka, L., Lipp, H.P., and Amrein, I. (2010). Number estimates of neuronal phenotypes in layer II of the medial entorhinal cortex of rat and mouse. Neurosci. *170*, 156–165.

Germroth, P., Schwerdtfeger, W.K., and Buhl, E.H. (1989). Morphology of identified entorhinal neurons projecting to the hippocampus. A light microscopical study combining retrograde tracing and intracellular injection. Neurosci. *30*, 683–691.

Gillies, M.J., Traub, R.D., LeBeau, F.E.N., Davies, C.H., Gloveli, T., Buhl, E.H., and Whittington, M.A. (2002). A model of atropine-resistant theta oscillations in rat hippocampal area CA1. J. Physiol. *543*, 779–793.

Giocomo, L.M., Zilli, E.A., Fransén, E., and Hasselmo, M.E. (2007). Temporal frequency of subthreshold oscillations scales with entorhinal grid cell field spacing. Science *315*, 1719–1722.

Gloveli, T., Schmitz, D., Empson, R.., Dugladze, T., and Heinemann, U. (1997). Morphological and electrophysiological characterization of layer III cells of the medial entorhinal cortex of the rat. Neurosci. *77*, 629–648.

Gloveli, T., Dugladze, T., Rotstein, H.G., Traub, R.D., Monyer, H., Heinemann, U., Whittington, M.A., and Kopell, N.J. (2005a). Orthogonal arrangement of rhythm-generating microcircuits in the hippocampus. Proc. Natl. Acad. Sci. U A *102*, 13295–13300.

Gloveli, T., Dugladze, T., Saha, S., Monyer, H., Heinemann, U., Traub, R.D., Whittington, M.A., and Buhl, E.H. (2005b). Differential involvement of oriens/pyramidale interneurones in hippocampal network oscillations in vitro. J. Physiol. *562*, 131–147.

Goldin, M., Epsztein, J., Jorquera, I., Represa, A., Ben-Ari, Y., Crépel, V., and Cossart, R. (2007). Synaptic kainate receptors tune oriens-lacunosum moleculare interneurons to operate at theta frequency. J. Neurosci. *27*, 9560–9572.

Goutagny, R., Manseau, F., Jackson, J., Danik, M., and Williams, S. (2008). In vitro activation of the medial septum-diagonal band complex generates atropine-sensitive and atropine-resistant hippocampal theta rhythm: An investigation using a complete septohippocampal preparation. Hippocampus *18*, 531–535.

Gulyas, A.I., Szabo, G.G., Ulbert, I., Holderith, N., Monyer, H., Erdelyi, F., Szabo, G., Freund, T.F., and Hajos, N. (2010). Parvalbumin-containing fast-spiking basket cells generate the field potential oscillations induced by cholinergic receptor activation in the hippocampus. J. Neurosci. *30*, 15134–15145.

Haas, J.S., and White, J.A. (2002). Frequency selectivity of layer II stellate cells in the medial entorhinal cortex. J. Neurophysiol. *88*, 2422–2429.

Haas, J.S., Dorval, A.D., and White, J.A. (2007). Contributions of Ih to feature selectivity in layer II stellate cells of the entorhinal cortex. J. Comput. Neurosci. *22*, 161–171.

Hafting, T., Fyhn, M., Molden, S., Moser, M.-B., and Moser, E.I. (2005). Microstructure of a spatial map in the entorhinal cortex. Nature *436*, 801–806.

Hafting, T., Fyhn, M., Bonnevie, T., Moser, M.-B., and Moser, E.I. (2008). Hippocampus-independent phase precession in entorhinal grid cells. Nature *453*, 1248–1252.

Halabisky, B. (2006). Electrophysiological classification of somatostatin-positive interneurons in mouse sensorimotor cortex. J. Neurophysiol. *96*, 834–845.

Hangya, B., Borhegyi, Z., Szilágyi, N., Freund, T.F., and Varga, V. (2009). GABAergic neurons of the medial septum lead the hippocampal network during theta activity. J. Neurosci. *29*, 8094–8102.

Harris, N.C., and Constanti, A. (1995). Mechanism of block by ZD 7288 of the hyperpolarization-activated inward rectifying current in guinea pig substantia nigra neurons in vitro. J. Neurophysiol. *74*, 2366–2378.

Harvey, C.D., Collman, F., Dombeck, D.A., and Tank, D.W. (2009). Intracellular dynamics of hippocampal place cells during virtual navigation. Nature *461*, 941–946.

Hasselmo, M.E., Fransen, E., Dickson, C., and Alonso, A.A. (2000). Computational modeling of entorhinal cortex. Ann. N. Y. Acad. Sci. *911*, 418–446.

Helm, J., Akgul, G., and Wollmuth, L.P. (2013). Subgroups of parvalbumin-expressing interneurons in layers 2/3 of the visual cortex. J. Neurophysiol. *109*, 1600–1613.

Heys, J.G., MacLeod, K.M., Moss, C.F., and Hasselmo, M.E. (2013). Bat and rat neurons differ in theta-frequency resonance despite similar coding of space. Science *340*, 363–367.

Hippenmeyer, S., Vrieseling, E., Sigrist, M., Portmann, T., Laengle, C., Ladle, D.R., and Arber, S. (2005). A developmental switch in the response of drg neurons to ets transcription factor signaling. PLoS Biol. *3*, e159.

Hu, H., Vervaeke, K., and Storm, J.F. (2002). Two forms of electrical resonance at theta frequencies, generated by M-current, h-current and persistent Na+ current in rat hippocampal pyramidal cells. J. Physiol. *545*, 783–805.

Hu, H., Martina, M., and Jonas, P. (2010). Dendritic mechanisms underlying rapid synaptic activation of fast-spiking hippocampal interneurons. Science *327*, 52–58.

Huerta, P.T., and Lisman, J.E. (1993). Heightened synaptic plasticity of hippocampal CA1 neurons during a cholinergically induced rhythmic state. Nature *364*, 723–725.

Huerta, P.T., and Lisman, J.E. (1995). Bidirectional synaptic plasticity induced by a single burst during cholinergic theta oscillation in CA1 in vitro. Neuron *15*, 1053–1063.

Izhikevich, E.M. (2003). Simple model of spiking neurons. IEEE Trans. Neural Netw. *14*, 1569–1572.

Izhikevich, E.M. (2007). Dynamical Systems in Neuroscience: The Geometry of Excitability and Bursting (Cambridge, Mass: MIT Press).

Jarsky, T., Roxin, A., Kath, W.L., and Spruston, N. (2005). Conditional dendritic spike propagation following distal synaptic activation of hippocampal CA1 pyramidal neurons. Nat. Neurosci. *8*, 1667–1676.

Jensen, O., and Colgin, L.L. (2007). Cross-frequency coupling between neuronal oscillations. Trends Cogn. Sci. *11*, 267–269.

Jolliffe, I.T. (2002). Principal component analysis (New York: Springer).

Jones, R.S.G., and Bühl, E.H. (1993). Basket-like interneurones in layer II of the entorhinal cortex exhibit a powerful NMDA-mediated synaptic excitation. Neurosci. Lett. *149*, 35–39.

Kepecs, A., and Fishell, G. (2014). Interneuron cell types are fit to function. Nature *505*, 318–326.

Khirug, S., Yamada, J., Afzalov, R., Voipio, J., Khiroug, L., and Kaila, K. (2008). GABAergic depolarization of the axon initial segment in cortical principal neurons is caused by the Na-K-2Cl cotransporter NKCC1. J. Neurosci. *28*, 4635–4639.

Kispersky, T.J., Fernandez, F.R., Economo, M.N., and White, J.A. (2012). Spike resonance properties in hippocampal o-lm cells are dependent on refractory dynamics. J. Neurosci. *32*, 3637–3651.

Kocsis, B., Bragin, A., and Buzsáki, G. (1999). Interdependence of multiple theta generators in the hippocampus: a partial coherence analysis. J. Neurosci. Off. J. Soc. Neurosci. *19*, 6200–6212.

Koenig, J., Linder, A.N., Leutgeb, J.K., and Leutgeb, S. (2011). The spatial periodicity of grid cells is not sustained during reduced theta oscillations. Science *332*, 592–595.

Kramis, R., Vanderwolf, C.H., and Bland, B.H. (1975). Two types of hippocampal rhythmical slow activity in both the rabbit and the rat: relations to behavior and effects of atropine, diethyl ether, urethane, and pentobarbital. Exp. Neurol. *49*, 58–85.

Krimer, L.S. (2005). Cluster analysis-based physiological classification and morphological properties of inhibitory neurons in layers 2-3 of monkey dorsolateral prefrontal cortex. J. Neurophysiol. *94*, 3009–3022.

Kumar, S.S., and Buckmaster, P.S. (2006). Hyperexcitability, interneurons, and loss of gabaergic synapses in entorhinal cortex in a model of temporal lobe epilepsy. J. Neurosci. *26*, 4613–4623.

Li, W.-C. (2004). A direct comparison of whole cell patch and sharp electrodes by simultaneous recording from single spinal neurons in frog tadpoles. J. Neurophysiol. *92*, 380–386.

Lin, R.J., Bettencourt, J., Wha Ite, J., Christini, D.J., and Butera, R.J. (2010). Real-time experiment interface for biological control applications. Conf. Proc. Annu. Int. Conf. IEEE Eng. Med. Biol. Soc. IEEE Eng. Med. Biol. Soc. Conf. *1*, 4160–4163.

Lisman, J. (2010). Working memory: the importance of theta and gamma oscillations. Curr. Biol. CB *20*, R490–R492.

Ma, Y. (2006). Distinct subtypes of somatostatin-containing neocortical interneurons revealed in transgenic mice. J. Neurosci. *26*, 5069–5082.

Maccaferri, G., and Lacaille, J.-C. (2003). Interneuron Diversity series: Hippocampal interneuron classifications: making things as simple as possible, not simpler. Trends Neurosci. *26*, 564–571.

MacQueen, J.B. (1967). Some methods for classification and analysis of multivariate observations. L.M.L. Cam, and J. Neyman, eds. (University of California Press), pp. 281–297.

Magistretti, J., and Alonso, A. (1999). Biophysical properties and slow voltage-dependent inactivation of a sustained sodium current in entorhinal cortex layer-II principal neurons: a whole-cell and single-channel study. J. Gen. Physiol. *114*, 491–509.

Mancilla, J.G., Lewis, T.J., Pinto, D.J., Rinzel, J., and Connors, B.W. (2007). Synchronization of electrically coupled pairs of inhibitory interneurons in neocortex. J. Neurosci. *27*, 2058–2073.

Manseau, F., Goutagny, R., Danik, M., and Williams, S. (2008). The hippocamposeptal pathway generates rhythmic firing of gabaergic neurons in the medial septum and diagonal bands: An investigation using a complete septohippocampal preparation in vitro. J. Neurosci. *28*, 4096–4107.

McBain, C.J., and Fisahn, A. (2001). Interneurons unbound. Nat. Rev. Neurosci. *2*, 11–23.

McGarry (2010). Quantitative classification of somatostatin-positive neocortical interneurons identifies three interneuron subtypes. Front. Neural Circuits.

McNaughton, B.L., Battaglia, F.P., Jensen, O., Moser, E.I., and Moser, M.-B. (2006). Path integration and the neural basis of the “cognitive map.” Nat. Rev. Neurosci. *7*, 663–678.

Middleton, S., Jalics, J., Kispersky, T., LeBeau, F.E.N., Roopun, A.K., Kopell, N.J., Whittington, M.A., and Cunningham, M.O. (2008). NMDA receptor-dependent switching between different gamma rhythm-generating microcircuits in entorhinal cortex. Proc. Natl. Acad. Sci. *105*, 18572–18577.

Miettinen, M., Koivisto, E., Riekkinen, P., and Miettinen, R. (1996). Coexistence of parvalbumin and GABA in nonpyramidal neurons of the rat entorhinal cortex. Brain Res. *706*, 113–122.

Mitchell, S.J., and Ranck, J.B. (1980). Generation of theta rhythm in medial entorhinal cortex of freely moving rats. Brain Res. *189*, 49–66.

Moca, V.V., Nikolic, D., Singer, W., and Muresan, R.C. (2014). Membrane resonance enables stable and robust gamma oscillations. Cereb. Cortex *24*, 119–142.

Monier, C., Chavane, F., Baudot, P., Graham, L.J., and Frégnac, Y. (2003). Orientation and direction selectivity of synaptic inputs in visual cortical neurons. Neuron *37*, 663–680.

Moser, E.I., Kropff, E., and Moser, M.-B. (2008). Place cells, grid cells, and the brain’s spatial representation system. Annu. Rev. Neurosci. *31*, 69–89.

Nolan, M.F., Dudman, J.T., Dodson, P.D., and Santoro, B. (2007). HCN1 channels control resting and active integrative properties of stellate cells from layer II of the entorhinal cortex. J. Neurosci. Off. J. Soc. Neurosci. *27*, 12440–12451.

Packer, A.M., and Yuste, R. (2011). Dense, unspecific connectivity of neocortical parvalbumin-positive interneurons: A canonical microcircuit for inhibition? J. Neurosci. *31*, 13260–13271.

Pastoll, H., Ramsden, H.L., and Nolan, M.F. (2012). Intrinsic electrophysiological properties of entorhinal cortex stellate cells and their contribution to grid cell firing fields. Front. Neural Circuits *6*, 17.

Pastoll, H., Solanka, L., van Rossum, M.C.W., and Nolan, M.F. (2013). Feedback inhibition enables theta-nested gamma oscillations and grid firing fields. Neuron *77*, 141–154.

Quilichini, P., Sirota, A., and Buzsaki, G. (2010). Intrinsic circuit organization and theta-gamma oscillation dynamics in the entorhinal cortex of the rat. J. Neurosci. *30*, 11128–11142.

Remme, M.W.H., Lengyel, M., and Gutkin, B.S. (2010). Democracy-independence trade-off in oscillating dendrites and its implications for grid cells. Neuron *66*, 429–437.

Richter, H., Heinemann, U., and Eder, C. (2000). Hyperpolarization-activated cation currents in stellate and pyramidal neurons of rat entorhinal cortex. Neurosci. Lett. *281*, 33–36.

Rousseeuw, P.J. (1987). Silhouettes: A graphical aid to the interpretation and validation of cluster analysis. J. Comput. Appl. Math. *20*, 53–65.

Sargolini, F. (2006). Conjunctive representation of position, direction, and velocity in entorhinal cortex. Science *312*, 758–762.

Schmidt-Hieber, C., and Häusser, M. (2013). Cellular mechanisms of spatial navigation in the medial entorhinal cortex. Nat. Neurosci. *16*, 325–331.

Schomburg, E.W., Fernández-Ruiz, A., Mizuseki, K., Berényi, A., Anastassiou, C.A., Koch, C., and Buzsáki, G. (2014). Theta phase segregation of input-specific gamma patterns in entorhinal-hippocampal networks. Neuron *84*, 470–485.

Schwerdtfeger, W.K., Buhl, E.H., and Germroth, P. (1990). Disynaptic olfactory input to the hippocampus mediated by stellate cells in the entorhinal cortex. J. Comp. Neurol. *292*, 163–177.

Seidenbecher, T., Laxmi, T.R., Stork, O., and Pape, H.-C. (2003). Amygdalar and hippocampal theta rhythm synchronization during fear memory retrieval. Science *301*, 846–850.

Siapas, A.G., Lubenov, E.V., and Wilson, M.A. (2005). Prefrontal phase locking to hippocampal theta oscillations. Neuron *46*, 141–151.

Singer, W. (2006). Consciousness and the Binding Problem. Ann. N. Y. Acad. Sci. *929*, 123–146.

Solstad, T., Boccara, C.N., Kropff, E., Moser, M.-B., and Moser, E.I. (2008). Representation of geometric borders in the entorhinal cortex. Science *322*, 1865–1868.

Soriano, E., Martinez, A., Farińas, I., and Frotscher, M. (1993). Chandelier cells in the hippocampal formation of the rat: the entorhinal area and subicular complex. J. Comp. Neurol. *337*, 151–167.

Spencer, S.S., and Spencer, D.D. (1994). Entorhinal-hippocampal interactions in medial temporal lobe epilepsy. Epilepsia *35*, 721–727.

Squire, L.R., Stark, C.E.L., and Clark, R.E. (2004). The medial temporal lobe. Annu. Rev. Neurosci. *27*, 279–306.

Stafstrom, C.E., Schwindt, P.C., and Crill, W.E. (1982). Negative slope conductance due to a persistent subthreshold sodium current in cat neocortical neurons in vitro. Brain Res. *236*, 221–226.

Stensola, H., Stensola, T., Solstad, T., Froland, K., Moser, M.-B., and Moser, E.I. (2012). The entorhinal grid map is discretized. Nature *492*, 72–78.

Stewart, M., and Fox, S.E. (1990). Firing relations of lateral septal neurons to the hippocampal theta rhythm in urethane anesthetized rats. Exp. Brain Res. *79*.

Stuart, G.J., and Sakmann, B. (1994). Active propagation of somatic action potentials into neocortical pyramidal cell dendrites. Nature *367*, 69–72.

Stuart, G., and Sakmann, B. (1995). Amplification of EPSPs by axosomatic sodium channels in neocortical pyramidal neurons. Neuron *15*, 1065–1076.

Tahvildari, B., and Alonso, A. (2005). Morphological and electrophysiological properties of lateral entorhinal cortex layers II and III principal neurons. J. Comp. Neurol. *491*, 123–140.

Tateno, T. (2004). Threshold firing frequency-current relationships of neurons in rat somatosensory cortex: type 1 and type 2 dynamics. J. Neurophysiol. *92*, 2283–2294.

Taube, J.S., and Muller, R.U. (1998). Comparisons of head direction cell activity in the postsubiculum and anterior thalamus of freely moving rats. Hippocampus *8*, 87–108.

Thurley, K., Hellmundt, F., and Leibold, C. (2013). Phase precession of grid cells in a network model without external pacemaker. Hippocampus.

Tikidji-Hamburyan, R., and Canavier, C. (2013). Critical role for noise and resonance in gamma band synchronization. (Program No.425.16 2013 Neuroscience Meeting Planner. San Diego, CA: Society for Neuroscience, 2013),.

Tort, A.B.L., Rotstein, H.G., Dugladze, T., Gloveli, T., and Kopell, N.J. (2007). On the formation of gamma-coherent cell assemblies by oriens lacunosum-moleculare interneurons in the hippocampus. Proc. Natl. Acad. Sci. U. A. *104*, 13490–13495.

Vanderwolf, C.H. (1969). Hippocampal electrical activity and voluntary movement in the rat. Electroencephalogr. Clin. Neurophysiol. *26*, 407–418.

Varga, C., Lee, S.Y., and Soltesz, I. (2010). Target-selective GABAergic control of entorhinal cortex output. Nat. Neurosci. *13*, 822–824.

Vida, I., Bartos, M., and Jonas, P. (2006). Shunting inhibition improves robustness of gamma oscillations in hippocampal interneuron networks by homogenizing firing rates. Neuron *49*, 107–117.

Wang, X.-J. (2002). Pacemaker neurons for the theta rhythm and their synchronization in the septohippocampal reciprocal loop. J. Neurophysiol. *87*, 889–900.

Wang, X.-J. (2010). Neurophysiological and computational principles of cortical rhythms in cognition. Physiol. Rev. *90*, 1195–1268.

Wehr, M., and Zador, A.M. (2003). Balanced inhibition underlies tuning and sharpens spike timing in auditory cortex. Nature *426*, 442–446.

White, J.A., Klink, R., Alonso, A., and Kay, A.R. (1998). Noise from voltage-gated ion channels may influence neuronal dynamics in the entorhinal cortex. J. Neurophysiol. *80*, 262–269.

White, J.A., Banks, M.I., Pearce, R.A., and Kopell, N.J. (2000). Networks of interneurons with fast and slow γ-aminobutyric acid type A (GABAA) kinetics provide substrate for mixed gamma-theta rhythm. Proc. Natl. Acad. Sci. *97*, 8128–8133.

Whittington, M.A., and Traub, R.D. (2003). Interneuron Diversity series: Inhibitory interneurons and network oscillations in vitro. Trends Neurosci. *26*, 676–682.

Whittington, M.A., Traub, R.D., and Jefferys, J.G.R. (1995). Synchronized oscillations in interneuron networks driven by metabotropic glutamate receptor activation. Nature *373*, 612–615.

Witter, M.P., and Moser, E.I. (2006). Spatial representation and the architecture of the entorhinal cortex. Trends Neurosci. *29*, 671–678.

Wolansky, T., Pagliardini, S., Greer, J.J., and Dickson, C.T. (2007). Immunohistochemical characterization of substance P receptor (NK(1)R)-expressing interneurons in the entorhinal cortex. J. Comp. Neurol. *502*, 427–441.

Woodhall, G.L., Bailey, S.J., Thompson, S.E., Evans, D.I.P., and Jones, R.S.G. (2005). Fundamental differences in spontaneous synaptic inhibition between deep and superficial layers of the rat entorhinal cortex. Hippocampus *15*, 232–245.

Woodruff, A.R., Anderson, S.A., and Yuste, R. (2010). The enigmatic function of chandelier cells. Front. Neurosci. *4*, 201.

Wouterlood, F.G., and Pothuizen, H. (2000). Sparse colocalization of somatostatin- and GABA-immunoreactivity in the entorhinal cortex of the rat. Hippocampus *10*, 77–86.

Wouterlood, F.G., Härtig, W., Brückner, G., and Witter, M.P. (1995). Parvalbumin-immunoreactive neurons in the entorhinal cortex of the rat: localization, morphology, connectivity and ultrastructure. J. Neurocytol. *24*, 135–153.

Wouterlood, F.G., van Denderen, J.C., van Haeften, T., and Witter, M.P. (2000). Calretinin in the entorhinal cortex of the rat: distribution, morphology, ultrastructure of neurons, and co-localization with gamma-aminobutyric acid and parvalbumin. J. Comp. Neurol. *425*, 177–192.

Wu, X., Liao, L., Liu, X., Luo, F., Yang, T., and Li, C. (2012). Is ZD7288 a selective blocker of hyperpolarization-activated cyclic nucleotide-gated channel currents? Channels *6*, 438–442.

Yartsev, M.M., and Ulanovsky, N. (2013). Representation of three-dimensional space in the hippocampus of flying bats. Science *340*, 367–372.

Yartsev, M.M., Witter, M.P., and Ulanovsky, N. (2011). Grid cells without theta oscillations in the entorhinal cortex of bats. Nature *479*, 103–107.

Yekhlef, L., Breschi, G.L., Lagostena, L., Russo, G., and Taverna, S.

(2015). Selective activation of parvalbumin- or somatostatin-expressing interneurons triggers epileptic seizurelike activity in mouse medial entorhinal cortex. J. Neurophysiol. *113*, 1616–1630.

Zhou, F.-M., and Hablitz, J.J. (1996). Morphological properties of intracellularly labeled layer I neurons in rat neocortex. J. Comp. Neurol. *376*, 198–213.